In-situ Small-Angle X-Ray Scattering Investigation of Transient Nanostructure of Multi-Phase Polymer Materials Under Mechanical Deformation

---

A thesis
submitted to the Department of Chemistry
in partial fulfilment of the requirements for
German academic degree Dr. rer. nat.
by

Ahmad Zeinolebadi

University of Hamburg
2012

to my beloved family

Reviewers/Gutachter

1. Prof. Dr. Norbert Stribeck

2. Prof. Dr. Patrick Theato

Disputation: 20/07/2012

Nomenclature

$\mathbf{r} = (r_1, r_2, r_3)$ real space vector and its components

$\mathbf{s} = (s_1, s_2, s_3)$ reciprocal space vector and its components

$\rho(\mathbf{r})$ electron density

σ_y yield stress

$I(\mathbf{s})$ scattering intensity

2θ scattering angle

ΔH_m melting enthalpy

ΔL long period distribution in meridional direction

ΔL_b breadth of a h_{ba} peak

Δ Laplacian operator

$\gamma(\mathbf{r})$ autocorrelation function

λ radiation wavelength

$\lceil \rceil$ slice mapping

$\{\}$ projection mapping

$\mathscr{F}_3$ 3D Fourier transform

$\mathscr{F}_3^{-1}$ inverse Fourier transform

μ linear absorption coefficient

ρ_i electron density of phase i (i=c crystalline phase, i=a amorphous phase)

σ stress

σ_r residual stress

τ lifetime

ε strain

$\varepsilon_{n,l}$ lateral nanoscopic strain

ε_n nanoscopic strain

ε_y break strain

ε_y yield strain

φ azimuthal angle

$A(t)$ actual sample cross-section at time t during tensile test

$A(\mathbf{s})$ scattering amplitude

d length-sacle of order in Bragg's law

E elastic modulus

e_{12} lateral extension of crystalline lamellae

$F(t)$ actaul force at time t during tensile test

$g(r)$ Chord Length Distribution (CLD)

$g_1(r)$ Interface Distribution Function (IDF)

H_b height of a h_{ba} peak

$h_i(r_{12}, r_3)$ distance distribution (peaks of CDF)

I_{Fl} fluctuation background

k total scattered intensity

L	long period
l	distance between fiducial marks
l_0	initial distance between fiducial marks
L_b	long period of a transverse lamellae-stack
M_n	number-average molecular weight
M_w	weight-average molecular weight
$P(\mathbf{r})$	Patterson function
R	sample-detector distance
R_g	radius of gyration
s	modulus of **s**-vector
T_c	crystallization temperature
T_m	melting temperature
V	iradiated volume
v	volume fraction
$z(\mathbf{r})$	Chord Distribution Function (CDF)
1D	one-dimensional
2D	two-dimensional
3D	three dimensional

Table of Contents

Abstract

There is an increasing demand for low-weight materials with tailored physical and mechanical properties. Polymeric multi-phase materials (such as copolymers, composites and blends) promise an excellent potential for hosting several functions. Designing new materials with desired properties requires deep knowledge of structure-property-relationship of polymers. In order to build up structure-property-relations one has to combine structure-characterization methods with mechanical tests. In-situ X-ray scattering measurement during deformation is one of the most versatile techniques for this kind of investigations. In this work small-angle X-ray scattering (SAXS) is applied during uniaxial stretching of oriented polymer materials. Direct analysis of the recorded SAXS patterns enables only a rough estimation of the structural transitions. More information is obtained by computing the chord distribution function (CDF). The only required assumption is a multi-phase structure. The CDF reveals the structural information in real space. From the peak-analysis of CDFs information about long period, long period distribution, domains shape and arrangement, and lateral extension of the domains are obtained. Furthermore, local nanoscopic strain and nanoscopic strain-heterogeneity can be estimated. The nanostructural parameters are correlated with the mechanical behavior of the investigated materials. In order to demonstrate the power of the method three classes of polymers are studied; namely i. a thermoplastic polyurethane elastomer (TPU), ii. polypropylene (PP) and its nanocomposites containing montmorillonite (MMT), and iii. microfibrillar reinforced composites (MFCs) based on high-density polyethylene (HDPE) and polyamides (PA6 and PA12). The results suggest that low-ordered materials such as TPUs exhibit non-affine deformation at the nanoscopic scale. In other words, the nanoscopic strain of a domain depends on its thickness. High-ordered materials such as HDPE and PP exhibit affine deformation at nanoscopic scale. This means that all lamellae stacks experience almost the same deformation. However, the nanoscopic strain – computed from the maximum of long period peak – is smaller than the macroscopic strain in all studied materials. This indicates that the well-correlated stacks (domains) deform less than the rest of the material. Other results concern void formation, strain-induced crystallization and evolution of nanoscopic parameters during continuous stretching and load-cycling tests.

Acknowledgments

I would like to express my greatest thanks to Prof. Dr. Norbert Stribeck. Without his unceasing support this thesis would not be a reality. Beside the fundamentals of X-ray scattering he taught me scientific reasoning and organizing a research work from the basic experimental works to interpretation of data and writing a manuscript. I would also like to thank my colleagues at Hamburg University and HASYLAB, DESY. Most of the studied materials in this work have been provided by colleagues from other universities and institutes. Accordingly I would like to thank Prof. Achim Frick from Aalen University, Prof. Zlatan Denchev from University of Minho, Dr. Katja Jankova from Danish Polymer Center and Prof. Jesper deClaville Christiansen from Aalborg University and their coworkers. This work was partially supported by the European FP7 project "Nanotough".

Chapter I

Introduction

"*Only those objects should engage our attention, to the sure and indubitable knowledge of which our mental powers seem to be adequate.*"
... René Descartes

New technologies request for new materials. Many new applications desire to combine various functions (e.g. biocompatibility, strength, stiffness, low-weight, etc.) in the same substance. Therefore, during the last decades there has been an increasing demand for new materials with hybrid properties [1,2]. For instance, automotive [3] and aviation industries strongly request for low-weight tough materials[1] in order to replace metal parts. The aim is to decrease fuel consumption. The driving forces are increasing oil prices and environmental issues.

Most of the conventional materials such as ceramics, metals and polymers cannot fulfill the requirements of the new technologies. Hence, designing novel materials is highly desired. Two main routes can be taken to make such materials: i. synthesis of materials with the desired chemical architectures and ii. combining various functions via compounding several constituents with distinct properties. A well-known example of the latter are polymer-based composites and blends. By mixing polymers with other organic or inorganic compounds – such as (nano)fillers, additives, etc. – materials with hybrid properties can be obtained. Thus polymers have received a huge attention due to their potential of hosting multiple functions.

Designing such advanced materials with tailored properties requires deep understanding of structure-property relationship of polymers. Polymers often form complex microstructures. For instance, copolymers form different morphologies according to their processing conditions. Each morphology in turn gives rise to es-

[1] see for example http://www.nanotough.aau.dk/ or http://hivocomp.eu/

pecial mechanical/physical properties. Moreover, the launch of hybrid materials[2] has enhanced the need for exact understanding of materials microstructures. In order to construct structure-property-relationships, one needs to combine stimulus-response[3] tests with structure-characterization techniques. In other words, one has to monitor the transitions of the structure during loading the material. When the structure-property-relations are known, the design of new materials can be based on a knowledge-driven route instead of try-and-error experiments.

This chapter briefly reviews the microstructure of polymers and methods of microstructure-characterization with an emphasis on X-ray techniques. The importance and objectives of the present work are declared in the last section.

1.1 Microstructure of Polymers

Chemically polymers are long-chain molecules of very high molecular weight, often measured in the tens-hundreds of thousands. For this reason, polymers are frequently referred to as "macromolecules" [4]. Polymers are characterized by polydispersity due to distribution of their chain lengths. In the melt state polymer chains form *random coils* with a statistical radius of gyration, R_g, estimated by [4,5]:

$$R_g^2 = \frac{na^2}{6}. \tag{1.1}$$

a and n are statistical segment length and number of segments per chain respectively. Chains inter-penetrate and form[4] entanglements. The entanglements act as temporary cross-links which give polymers their unique viscoelastic properties. Figure 1.1 summarizes schematically three important characteristics of almost all synthetic polymers.

When cooled from the melt state, polymers usually show a second-order transition known as *glass transition*. Thus they form an *amorphous* solid (*glass*) [6]. However, polymer chains with high stereo-regularity may crystallize [5,7]. The

[2] Hybrid materials are composites consisting of two constituents at the nanometer or molecular level. Usually one components is inorganic and the other one organic [2].

[3] The stimuli can be for example a mechanical load or heat.

[4] provided they are longer than a threshold length

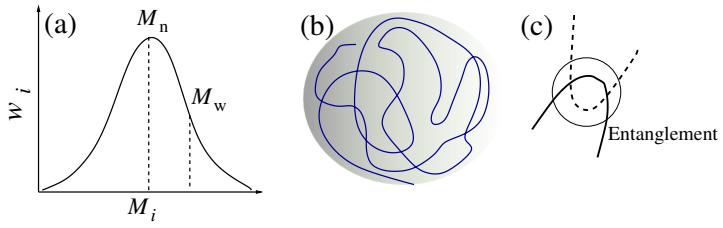

Figure 1.1: Polymers are characterized by high molecular weight, molecular weight distribution (polydispersity), random-coil conformations in the melt state and chain entanglements: (a) a schematic curve showing weight fraction of species i versus its molecular weight, M_i. Polymers are usually characterized by their number-average molecular weight, M_n, and weight-average molecular weight, M_w.(b) Polymer chains form random coils in the melt state. (c) Entanglements are formed due to inter-penetration of chains

crystallization occurs at temperatures between the melting temperature and the glass transition point. Due to the structural irregularities such as entanglements, chain-ends, side-chains, etc. polymers can form only *semi-crystalline* solids.

The semi-crystalline structure of polymers is characterized by special features. Firstly, the crystallites are embedded in an amorphous matrix, resulting in a two-phase morphology. Secondly, most polymers form *folded-chain* crystals in which the chains fold back into the same crystallite[5]. Thirdly, several crystallites stack up and form superstructures known as *spherulites* [8], Figure 1.2. Finally, chains wander from one crystallite to the next one, thereby connecting them to each other. The chain segment between two adjacent crystals is known as *tie-molecule* [9]. Tie-molecules act as stress-transmitters [10–12]. Thus they play an important role in mechanical properties of semi-crystalline polymers.

Several parameters such as chemical structure, processing conditions, impurities (nucleating agents) and thermal history determine the crystallinity and the microstructure of the semi-crystalline polymers. Microstructure, in turn, determines the physical/mechanical properties of the material.

Another phenomenon which affects microstructure of polymers is phase separation. Phase separation is commonly observed in polymer blends and in copolymers. The driving force of phase separation is the immiscibility of the components. Thus the thermodynamic interaction of the components determines the

[5] Under especial conditions (e.g. high pressure) *extended-chain* crystals are also observed [4]. Some polymers may also crystallize under mechanical deformation (strain or shear) [7].

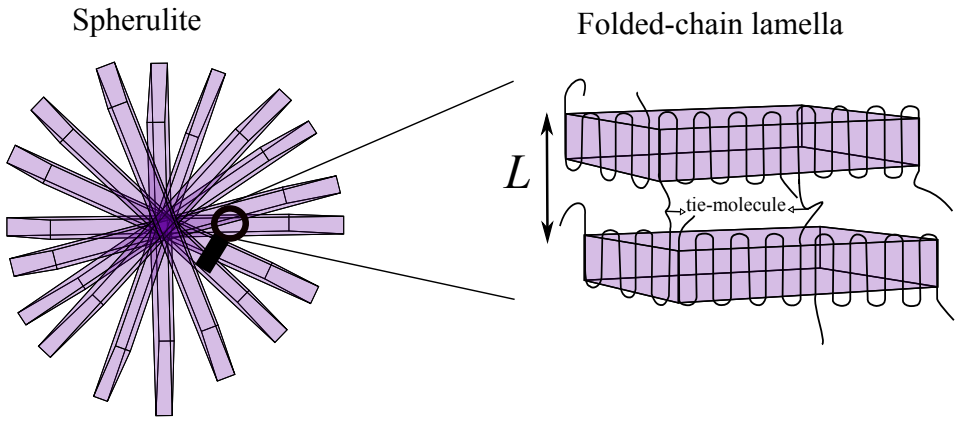

Figure 1.2: Upon cooling from the melt some polymers crystallize and form folded-chain lamellae. Several lemellae stack up and form superstructures known as spherulites. Chains wander from one lamellae to the next one. Parts of the chains shared by two neighboring lamellae are called tie-molecules. Tie-molecules play an important role in the mechanical behavior of semi-crystalline polymers

phase separation process and the resulting microstructures.

The microstructure of polymers can also be altered by the presence of solid particles such as (inorganic) fillers [13]. For example, nano-particles affect the dynamics of their adjacent chains [14]. Moreover, fillers can nucleate crystallization of polymers, thereby changing their semi-crystalline morphology [13]. Nano-particles can also form several (nano)structures according to their interaction with the matrix [15].

In summary, multi-phase microstructures are very common in polymers. The microstructure determines the properties of the material. Thus material design requires deep knowledge of the mechanisms which govern structure formation and behavior of polymers.

1.2 Mechanical Behavior

In this work we focus mainly on the structure and properties of semi-crystalline thermoplastic[6] polymers. Therefore, we confine our discussion only to this class of polymers.

[6] A material that can be melted several times

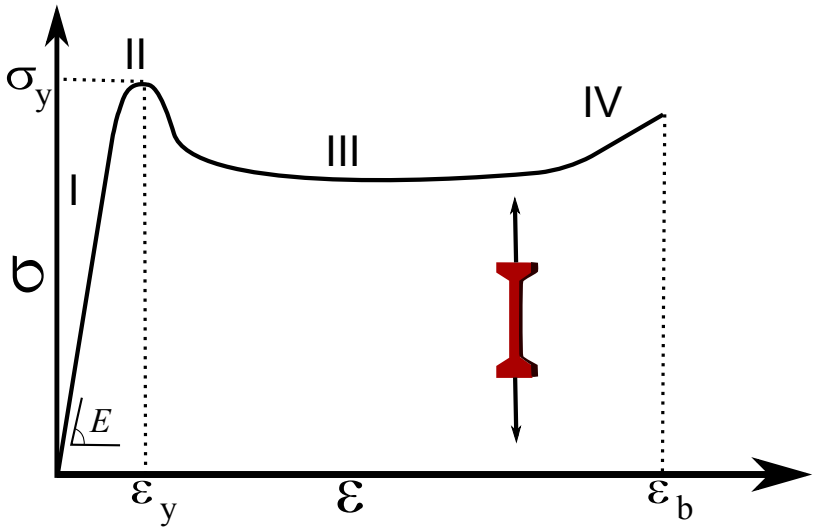

Figure 1.3: Typical stress-strain curve of thermoplastic polymers (e.g. polyethylene). Four regions can be observed on the curve: I. elastic region, the slope of the curve at low strains gives the Young's modulus of elasticity E; II. yield point defined by yield stress σ_y and yield strain ε_y; III. strain softening; IV. stress hardening is observed in some polymers. Finally the sample breaks at its break-strain ε_b

In practice polymeric materials are often subjected to mechanical loads. Therefore, it is essential to know how polymers respond to the mechanical load. Figure 1.3 presents the common behavior of thermoplastic polymers under uniaxial deformation. On the stress(σ)-strain(ε) curve four regions [7] can be distinguished: in region I the material shows an elastic[7] behavior. In this region the material is characterized by its Young's modulus of elasticity. In region II the material yields. The slope of the curve decreases in this region. The yield point is defined by yield stress σ_y and yield strain ε_y. Above ε_y, the material shows strain softening (region III) followed by strain hardening (region IV) [7]. The sample breaks finally at the break-strain ε_b. The area under the curve has units of energy, thus it is a measure of the strength (impact resistance) of the material. In practice materials are usually designed to be used in region I. However, the other three regions have important roles because they determine the failure behavior of the material.

In many applications polymers are designed to be used under (dynamic)cyclic

[7] In the elastic region the deformation is completely reversible; i.e. Hookean behavior

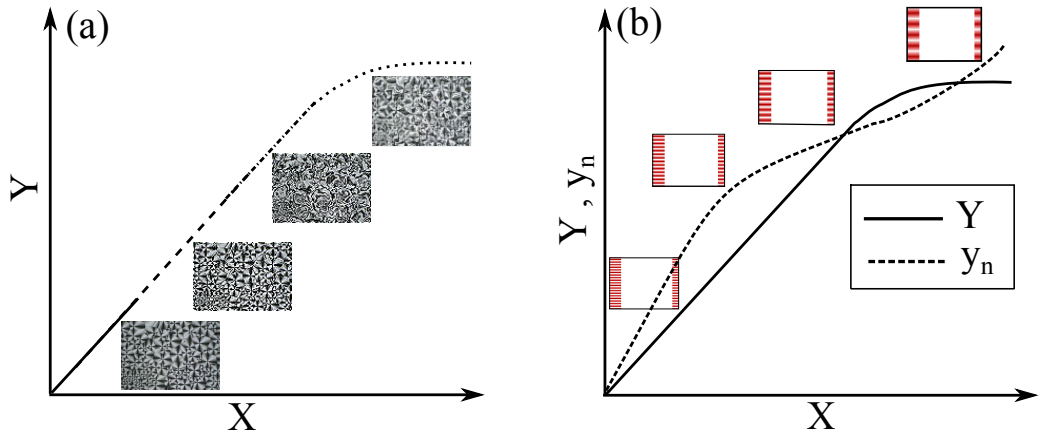

Figure 1.4: Two main concepts of monitoring microstructural evolution. X is the stimulus (e.g. strain) and Y is the macroscopic response (e.g. stress) while y_n is a microstructural parameter (e.g. long period of semi-crystalline lamellae-stack) (a) direct observation in physical space. In this method samples should be prepared at different steps of the test (b) indirect observation by techniques such as X-ray scattering. In this method it is possible to run in-situ measurements. Usually a simple structural model is assumed in order to extract structural parameters that describe the dominant structure

loads [16] (e.g. mechanical vibration). Long-term exposure to dynamic loads causes a gradual and localized structural damage. Accordingly, under dynamic loads polymers will fail at stress levels much lower than they can withstand under static loading conditions [17]. This effect is known as fatigue. Fatigue behavior of polymers has great industrial relevance because it determines the service-life of a polymer part. Despite its importance, the fatigue mechanisms of polymers are still not fully understood [18].

1.3 Constructing Structure-Property-Relationship

In the literature there are abundant papers studying the structure-property-relationships of polymers under mechanical load. One can divide the methods into two groups according to the applied structure-analysis techniques: i. direct observation of the structure in physical space, and ii. indirect observation by monitoring a parameter (e.g. scattering intensity) that can be related to the structure. Figure 1.4 schematically summarizes these two concepts. In the first method information about the morphology is directly obtained from the recorded data. The advantage

of this method is its simplicity. However, in most cases it is not possible to record images simultaneously during a mechanical test. In the second method one has the possibility to perform in-situ measurements. The challenge of the indirect observation is the more complicated data-analysis compared to the direct methods. Therefore, one has to reduce the complexity of the morphology, in order to obtain simple models that describe the dominant structure. For instance, it is usually assumed that polymers form domains with disc-like, rod-like or plate-like shapes. This makes it possible to extract simple parameters that quantitatively describe the morphology. In the following paragraphs examples of both methods are briefly[8] discussed.

Probably the most common direct observation method is the microscopy technique [19–24]. Microscopes usually scan the surface [20] of the sample. Therefore, the image may not be representative of the whole sample. The other drawback of microscopy methods is that most techniques such as SEM[9], TEM[10] and AFM[11] require special sample preparation [20]. This causes problems when the surface of the sample is scanned during deformation. For instance, opening up of fresh, uncoated surfaces leads to charging problems during in-situ SEM-deformation studies [25]. Generally, one has to prepare a series of samples deformed to different strains.

However, application of environmental scanning electron microscope (ESEM) [26] has made real-time measurements possible. With this technique the structural transitions at the crack tip can be directly monitored during deformation [27–29]. ESEM is especially useful for investigation of fracture mechanisms [29] such as crazing and cavitation. However, there is still no work reporting the transitions of the semi-crystalline structure during deformation studied by ESEM. The reason can be the fact that the amorphous phase is eroded from the surface of the uncoated polymer sample by the scanning electron beam [30].

Polarized optical microscope, POM, has been used for on-line monitoring of

[8] Due to the the large number of papers, here we cite only the most important review papers or those papers which deal with the same materials that are used in this study; namely polypropylene, polyethylene and thermoplastic polyurethane elastomers

[9] Scanning Electron Microscopy

[10] Transmission Electron Microscopy

[11] Atomic Force Microscopy

transient structures [31] in polypropylene. This technique does not need complicated sample preparation. However, the length-scale of the observed structure is limited to some microns. Scanning near-field optical microscopy has also been applied to monitor single-chain deformation [32]. In summary, simultaneous microscopy-deformation measurements are still very limited due to the problems concerning sample preparation.

The indirect observation methods are abundant. Here we mention some the most relevant ones:

Solid-state NMR[12] reveals information about molecular mobility in different physical phases and the size of chain-extended crystals [33].

FT-IR[13] enables quantification of the degree of orientation as a feature of structural transition upon deformation in both crystalline and amorphous phases [34, 35].

Rheo-optics can be used to study molecular orientation (birefringence) during deformation [36].

PA-IR[14] provides information about molecular orientation during and after fast irreversible deformations with a time resolution in the order of microseconds and a low data scatter [37].

Raman spectroscopy can be used to study the structure and the deformation behavior at the molecular level [38].

Positron annihilation monitors primarily variations of free-volume during deformation. For instance, chain-scission increases the free-volume [39].

SANS[15] has been applied to monitor conformational changes of polystyrene chains under uniaxial extension [40].

X-ray microtomography with sub-micrometer resolution has been used to investigate the evolution of the microstructure of semi-crystalline polymers during tensile deformation [41].

X-ray scattering methods: probably X-ray scattering is the most versatile method for in-situ structure-characterization during deformation. This technique provides abundant information [42, 43] about structural variations from a molecular

[12] Nuclear Magnetic Resonance Spectroscopy

[13] Fourier Transform Infrared Spectroscopy

[14] Polarized Planar Array Infrared Spectroscopy

[15] Small-Angle Neutron Scattering

level up to several micrometers. Most of the above mentioned techniques provide complementary information to X-ray scattering data and are often applied in parallel with X-ray techniques. Next section briefly reviews application of X-rays for structure analysis of polymers.

1.4 Structure Analysis by X-Ray Scattering

X-rays are electromagnetic radiation classically generated by bombarding a metal with high-energy electrons. X-rays have a wavelength of the order of 10^{-12} to 10^{-8} m [44,45]. In material science a narrow range of wavelength 0.5-2.5$\times 10^{-10}$ m is used. This range of wavelength is of the same order of magnitude as the most inter-atomic distances in condensed matter [44]. Studies on polymers are usually done with radiation having a wavelength of ca. 0.15 nm [44]. In-situ measurements[16] require low exposure time and fast data acquisition. Therefore, in-situ X-ray measurements are usually done at synchrotron radiation facilities.

Synchrotron radiation (Figure 1.5) is produced when electrons orbit in a magnetic field and lose energy continually in the form of electromagnetic radiation (photons) emitted tangentially from the orbit [46]. The special feature that makes synchrotron radiation suitable for in-situ measurements is its high brilliance [45]. Brilliance is defined by:

$$\text{brilliance}=\frac{\text{Photons/second}}{\text{collimation(mrad)}^2\text{source-area(mm)}^2(0.1\%\text{ band-width})}. \qquad (1.2)$$

High brilliance means that the beam has a high intensity, low divergence over propagation, small area and low band-width. High brilliance ensures that low-noise data can be recorded in a short time. Thus fast structural transitions can be monitored without the need to stop the ongoing test.

In addition to the time-scale, one should consider the length-scale of the structures desired to be studied. Polymers often show hierarchical structures, Figure 1.6. This means that order is observed in a wide range starting from molecular level (unit cell of the crystals) up to several micrometers (spherulites). X-rays can easily be adopted to investigate (ordered)structures with the desired length-

[16] performing an X-ray scattering measurement during deformation

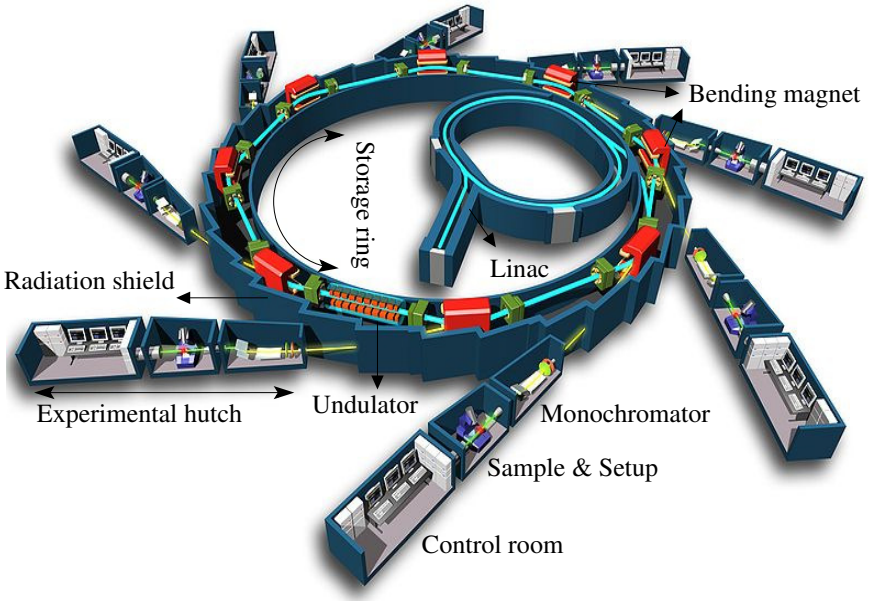

Figure 1.5: Synchrotron radiation ring. Source of the original image: http://en.wikipedia.org/wiki/File:Sch%C3%A9ma_de_principe_du_synchrotron.jpg

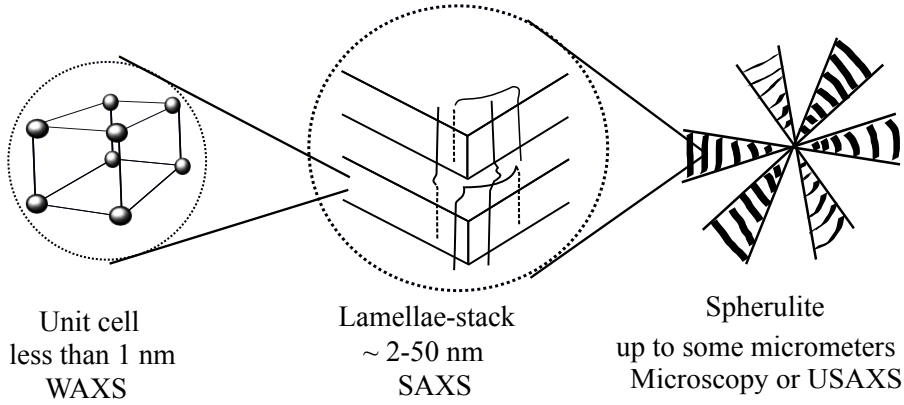

Figure 1.6: Hierarchical structures are common in semi-crystalline polymers. By varying the sample-detector distance one can observe different structural entities

Table 1.1: Subareas of scattering as a function of the sample–detector distance R. X-ray wavelength is assumed to be 0.15 nm [46]

Sub-area	R [m]	Focus	Application
WAXS	0.05-0.2	Arrangement of atoms (chain segments)	Crystallography
MAXS	0.2-1	Liquid-crystalline structure	Clay intercalation
SAXS	1-3	Nanostructure 2-50 nm	Semi-crystalline structure of polymers, Porous materials
USAXS	6-15	Nanostructure 15 nm - 2 µm	Multi-layer polymer films

scale [43]. Already the Bragg's law [47] shows the relation between the length-scale of order d, radiation wavelength λ and scattering angle 2θ:

$$d = \frac{\lambda}{2\sin\theta} \tag{1.3}$$

In practice one has to vary the sample-detector distance in order to obtain good resolution in the desired angular region. In material science X-ray scattering measurements are usually done in four angular regions, Table 1.1.

The classical X-ray diffraction and scattering are carried out in the sub-area of wide-angle X-ray scattering (**WAXS**) [46]. The scattering patterns in the wide-angle region yield information on the arrangement of polymer-chain segments. Variations of orientation of the chains within the amorphous phase, structure of the unit-cell, size of crystals, crystal distortions and crystallinity can be studied [31, 48–50].

The subareas of middle-angle X-ray scattering (**MAXS**) covers the characteristic scattering of liquid-crystalline structure and rigid-rod polymers. For example, intercalation of layered-silicates (clay) is studied in this region [51]. In literature this angular region is often referred to as small-angle due to the similarities in data-analysis in both regions.

The small-angle X-ray scattering (**SAXS**) regime reveals the typical nanostructures observed in semi-crystalline materials, thermoplastic elastomers, copolymers and multi-phase blends. The structure of lamellae-stacks [49, 50, 52, 53], orien-

tation of lamellae[31,50,54] , lamellae-distortion [55], crazing and yielding [55,56] can be studied in this region. **SAXS tomography** [57,58] is used to study structure gradients of polymer samples with fiber symmetry. But there is still no report of simultaneous SAXS-tomography during deformation.

The ultra small-angle X-ray scattering (**USAXS**) extends the accessible structure towards the micrometer range [59].

In summary one can monitor the desired length-scale easily by adjusting the sample-detector distance. In-situ measurements can be performed by using a high intensity source such as synchrotron radiation. Thus structure-property-relations can be best investigated by application of X-ray scattering techniques.

1.5 Objectives and Aims

X-ray scattering measurements have been long used to study structure evolution of polymers during deformation. Most of the works investigate isotropic materials. However, many industrial processing methods (e.g. injection molding, extrusion, etc.) produce oriented (anisotropic) materials. Therefore, it has industrial relevance to investigate structure evolution of oriented polymers. Also from the academic point of view, oriented polymers are interesting because their scattering patterns gives more structural information compared to isotropic materials. From the 2-dimensional scattering pattern of an uniaxially oriented sample (anisotropic pattern) two dimensions of crystallites (thickness and breadth) can be obtained, whereas from an isotropic pattern only one dimension – namely the long period averaged over all directions – can be obtained.

In this work different types of oriented polymer and composite materials are studied. The first studied material is an injection-molded thermoplastic polyurethane elastomer (TPU). TPU materials are broadly used[17] in construction, automotive, sports, and many other industries. TPUs usually form a (multi)two-phase morphology which is similar to a semi-crystalline structure. The second studied system is polypropylene (PP) and its nanocomposites reinforced by montmorillonite (MMT). PP/MMT nanocomposites are designed with the aim of obtaining strong low-weight materials that can replace metals in automobiles and aircrafts. The last studied materials are microfibrillar reinforced composites (MFC). MFCs are

[17] see for example http://www2.basf.us/urethanechemicals/tpu/index.htm

polymer-polymer composites[18] which are highly requested by automobile industry. Thus by choosing these three systems a fairly wide range of materials with various structures and properties are covered.

Macroscopic behavior of the studied materials is characterized by stress-strain curves. Accordingly, two types of mechanical tests are designed. The first one is a continuous stretching test which characterizes the mechanical properties of the studied materials. The second one is a slow load-cycling[19] test that tries to shed some light on the less investigated fatigue mechanisms.

The nanostructural transitions are monitored by small-angle X-ray scattering of the oriented polymers. In the SAXS region information about the semi-crystalline morphology is obtained. Scattering data is transformed into the real space by performing Fourier-transform. The resulting chord-distribution function (CDF) reveals the structure in real space. Nanostructural parameters are extracted from the CDFs. Deformation and distortion of crystalline lamellae, strain-induced crystallization/melting and strain-heterogeneity are monitored at the nano-scale.

The aim of the study is to improve the understanding of structure-property-relationships of multi-phase polymer materials. In doing so the nanostructural parameters are correlated with the mechanical behavior of the materials.

Chapter 2 briefly reviews the SAXS theories. The experimental works are explained in Chapter 3. Chapter 4 is dedicated to the description of data evaluation methods. The results and discussions are covered in three separate chapters (5-7) according to the studied materials. Finally, Chapter 8 summarizes the results and gives suggestions for future works.

---

[18] The fabrication process of MFCs begins with melt-blending followed by cold drawing of the resulting polymer blends. In so doing, the domains of the semi-crystalline blend components are transformed into microfibrils, thus forming the so-called oriented precursor blends. Finally, these precursors are molded at temperatures below the melting of the fibril-forming component and above that of the matrix-forming component. Hence, only the matrix polymer is isotropized, whereas the microfibrils of the reinforcements maintain their orientation and increase their crystallinity.

[19] slow load-cycling experiments are performed because at the moment (CCD detector at A2, HASYLAB) the lowest required exposure time for obtaining low-noise SAXS data is ca. 20 s. In a real fatigue test the exposure time would be below 100 ms.

Chapter II

SAXS Theories

"There is need of a method for finding out the truth."
... René Descartes

This chapter briefly reviews the main concepts and formulations for the analysis of SAXS patterns of semi-crystalline polymers with fiber symmetry.

2.1 Geometry of Scattering

Figure 2.1 presents schematically the normal transmission setup which is frequently used for in-situ X-ray scattering experiments [60]. Sample and detector are oriented at right angles (normal) with respect to the X-ray primary beam. The primary beam penetrates a relatively thin sample (ca. 1-10 mm). The scattering intensity $I(x,y)$ is recorded by means of a planar detector in transmission mode.

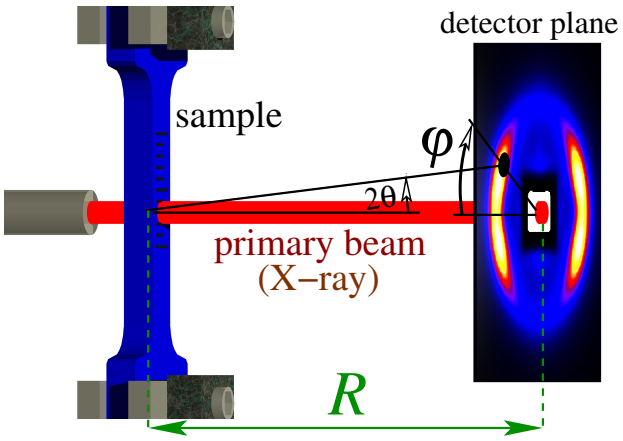

Figure 2.1: *Normal transmission setup* of an X-ray scattering experiment. The intensity at a chosen point (circular mark) on the planar detector, $I(2\theta,\varphi)$ is a function of the scattering angle 2θ and the azimuthal angle φ. R is the sample-detector distance [60]

The angular range of the recorded pattern is controlled by the sample-detector distance R. Equation 2.1 shows the relation between the scattering-related coordinates, $(2\theta, \varphi)$, and the pixel coordinates[1] (x, y) on the detector

$$\begin{aligned} \tan 2\theta &= \sqrt{x^2+y^2}/R \\ \tan \varphi &= y/x, \end{aligned} \tag{2.1}$$

with the scattering angle 2θ, and the azimuthal angle φ [60].

In an X-ray scattering experiment, we are interested in the relation of the measured scattering intensity to the structure inside the volume V that is irradiated by the X-ray beam. X-rays interact with the electrons of the materials, hence the structure is defined by the electron density $\rho(\mathbf{r})$ [60]. Here $\mathbf{r} = (r_1, r_2, r_3)$ is the vector in real space. X-rays are scattered when $\rho(\mathbf{r})$ varies inside the irradiated volume. Thus phases without electron-density-contrast cannot be distinguished by means of X-ray scattering.

As stated by the kinematic scattering theory the relation between the structure of matter and the scattered intensity can be best understood [60], if the latter is treated in the so-called reciprocal space $\mathbf{s} = (s_1, s_2, s_3)$, i.e.

$$I(2\theta, \varphi) \rightarrow I(\mathbf{s}) \tag{2.2}$$

Figure 2.2 shows the geometric relation between the sample coordinate system in real space, the reciprocal space and finally with the scattering intensity measured on the detector's plane. Analysis of Eq. 2.2 shows that it maps a plane into reciprocal space. The mapping is non-linear. The image of the infinite detector plane in reciprocal space is the surface (the vecror $\mathbf{s}$ moves on the surface) of the sphere indicated in Figure 2.2. The sphere is known as the *Ewald sphere*. The sample in its real space coordinate system $\mathbf{r} = (r_1, r_2, r_3)$ is placed in the center of the Ewald sphere. The primary beam propagates from left to right. Assuming an infinitesimal irradiated volume V the scattering intensity $I(2\theta, \varphi)$ is observed. The origin of reciprocal space, $\mathbf{s} = (s_1, s_2, s_3)$, is attached to the point where the primary beam (after penetrating the sample) breaks through the Ewald sphere. The Cartesian axes of reciprocal space (s_1, s_2, s_3) are parallel to the axes (r_1, r_2, r_3) of the coordinate system of the real space. Thus by rotating the sample in the beam

[1] It is assumed that the center of the primary beam on the detector-plane is at $x = y = 0$.

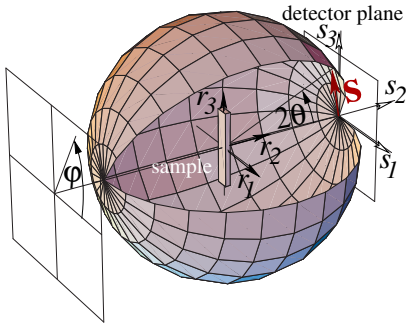

Figure 2.2: Experiment geometry, Ewald sphere, and reciprocal space. The sample is placed in the center of the sphere. Its structure is defined in the real-space coordinates, $\mathbf{r} = (r_1, r_2, r_3)$. The origin of reciprocal space, $\mathbf{s} = (s_1, s_2, s_3)$, is attached to the surface of the Ewald sphere. The orientation of its axes is strictly fixed to the orientation of the sample space $\mathbf{r}$. Each point on a plane detector (for clarity shifted to a position in front of the sphere) can be addressed by the two coordinates scattering angle, 2θ, and azimuthal angle, φ. The mapping of these two coordinates into reciprocal space is mediated by means of the surface of the Ewald sphere [60]

one can record the scattering intensity over a considerable fraction of reciprocal space, in which Ewald's sphere is the representation of the detector plane [60].

Generally one has to rotate the sample in order to collect the information that is required for a structure analysis. Fortunately, soft materials often exhibit some types of symmetry of the scattering intensity $I(\mathbf{s})$. Every kind of symmetry reduces the necessary effort [60].

Isotropy. In the case of *isotropic scattering* [46] the scattering intensity $I(\mathbf{s})$ is only a function of the modulus of the $\mathbf{s}$-vector, $s = \sqrt{s_1^2 + s_2^2 + s_3^2}$, i.e.

$$I(\mathbf{s}) = I(s) \tag{2.3}$$

On the plane detector the intensity is no longer a function of the azimuthal angle φ. In the most simple definition of reciprocal space, s is related to the scattering angle by

$$s = \frac{2}{\lambda} \sin\theta, \tag{2.4}$$

with λ the wavelength of the X-ray. In the case of an isotropic pattern all the intensity maxima appear on the plane detector as rings known as "Debye-Scherrer

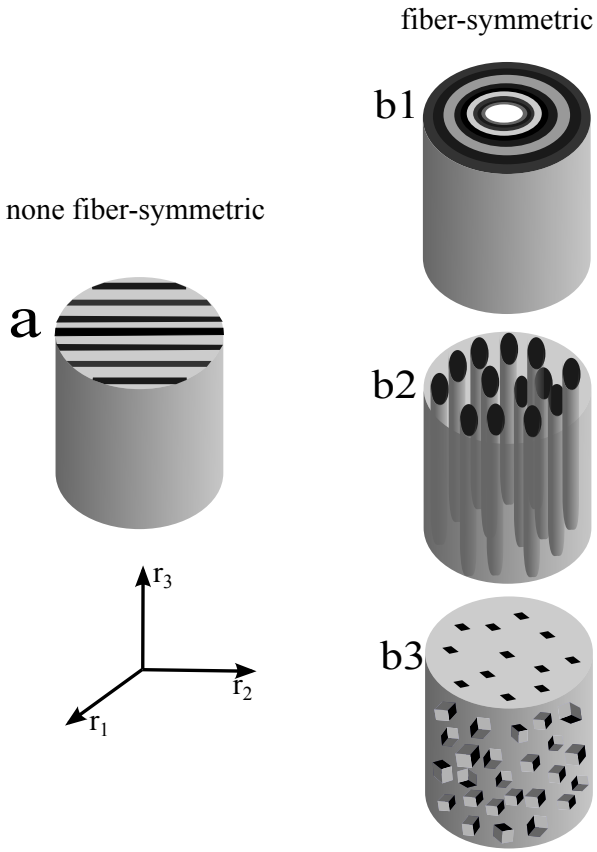

Figure 2.3: Some examples of none-fiber-symmetric (a) and fiber-symmetric samples (b1,b2,b3). Material (a) shows SAXS peaks only when the X-ray beam is not parallel to r_1. The scattering pattern of fiber-symmetric materials does not change by rotating the sample around r_3-axis

rings". Thus a radial cut (slice) extending outward from the center of the pattern gives simply the complete information on the scattering.

Fiber symmetry Fiber symmetry is uniaxial or cylindrical symmetry, Figure 2.3. Rotating the sample about the fiber axis does not change the scattering pattern, but tilting the sample with respect to the fiber axis does [46]. With s_3 in fiber direction the pattern shows rotational symmetry in the (s_1, s_2)-plane.

$$I(\mathbf{s}) = I(s_{12}, s_3), \tag{2.5}$$

where $s_{12} = \sqrt{s_1^2 + s_2^2}$ is the transverse coordinate in cylindrical coordinates, and s_3 is the longitudinal coordinate of reciprocal space in fiber direction. Thus $I(\mathbf{s})$ is a function of s_3 and the distance from this axis only. A fiber symmetric material combined with a 2D detector provide a brilliant chance for an in-situ monitoring of structure evolution. The reason is readily clear from Eq. 2.5; namely the complete scattering information from reciprocal space can be recorded by a 2D detector in a single exposure. However, in order to exploit fiber symmetry to its maximum content, the detector should record a representative plane of reciprocal space, e.g. (s_1, s_3), by means of a rectangular frame [46,60]. As mentioned before the detector is the surface of the Ewald sphere, and this sphere is bending off the (s_1, s_3)-plane. Nevertheless, in the small angle region (SAXS) the curvature of the detection surface causes no serious problem because the so called *tangent-plane approximation* holds in this region (close to the origin $\sin\theta \approx \tan\theta \approx \theta$) [46,60]. Hence, in the SAXS region the Ewald sphere can be well approximated by its tangential (s_1, s_3)-plane. Thus in the favorable case of fiber-symmetric samples the *complete*[2] information is recorded in one 2D image [46]. From a mathematical point of view the recorded pattern is a slice:

$$\lceil I(\mathbf{s}) \rceil_2 (s_1, s_3) \equiv I(s_{12}, s_3) \tag{2.6}$$

2.2 From the Scattering Pattern to the Materials Structure

The purpose of an in-situ X-ray measurement is to monitor the evolution of the materials structure during the mechanical test. The main challenge of such experiments is the huge number of recorded patterns. Moreover, the scattering data is recorded in the reciprocal space. Thus direct analysis of the as-recorded patterns can be confusing or misleading. Therefore, a combination of theoretical tools – that transform the scattering data from the reciprocal space into the real space – and fast automated computer programs is required to obtain a thorough understanding of the structure evolution. The latter is needed to shrink the analysis

[2] Completeness means that from the recorded data one can reconstruct the scattering intensity for every point inside a sufficiently big volume of reciprocal space [46]. In the SAXS region a 1D curve is complete if the material is isotropic. A 2D pattern is complete if the material has fiber symmetry and the principal axis of the sample is set normal to the direction of X-ray beam.

time. In this section the theories will be discussed. The data evaluation routes will be discussed separately in Chapter 4.

2.2.1 The Magic Square

The fundamental relations between the electron density distribution inside the sample, $\rho(\mathbf{r})$, and the observed scattering intensity, $I(\mathbf{s})$ can be sketched [46] in a so called "magic square".

$$\begin{array}{ccccc} & & \rho(\mathbf{r}) & \overset{\mathscr{F}_3}{\Leftrightarrow} & A(\mathbf{s}) \\ & & \star 2 \Downarrow & & \Downarrow |\,|^2 \\ z(\mathbf{r}) & \underset{\Delta}{\Leftrightarrow} & P(\mathbf{r}) & \underset{\mathscr{F}_3}{\Leftrightarrow} & I(\mathbf{s}) \end{array} \tag{2.7}$$

According to the magic square, the real space electron density, $\rho(\mathbf{r})$, is converted into the scattering amplitude, $A(\mathbf{s})$, in reciprocal space by a 3D complex Fourier transform. The square of the absolute value of $A(\mathbf{s})$ gives the scattering intensity [46]:

$$I(\mathbf{s}) = |A(\mathbf{s})|^2 \tag{2.8}$$

The path from the scattering amplitude to the scattering intensity is a one-way path (depicted by a unidirectional downward arrow in Eq. 2.7). Thus the phase information of the structure is lost. This inhibits reconstruction of the absolute positions of individual domains (i.e. crystallites) in the material. Only relative distances among domains, i.e. their correlations can be determined [46,60].

Going back to the real space is possible by performing an inverse Fourier transform on the $I(\mathbf{s})$ [46,60]. The result of this operation is the so called *Patterson function*,

$$P(\mathbf{r}) = \mathscr{F}_3^{-1}(I(\mathbf{s})). \tag{2.9}$$

The physical meaning of the Patterson function can be understood by introduction and interpretation of the autocorrelation operation $\star 2$

$$P(\mathbf{r}) = \rho^{\star 2}(\mathbf{r}), \tag{2.10}$$

which turns the structure $\rho(\mathbf{r})$ directly into $P(\mathbf{r})$. The autocorrelation integral is defined in Eq. 2.11.

$$\rho^{\star 2}(\mathbf{r}) = \int \rho(\mathbf{y})\, \rho(\mathbf{r}+\mathbf{y})\, d^3y, \tag{2.11}$$

It is identified by the overlap integral between the structure, $\rho(\mathbf{y})$, and its displaced ghost. In Eq. 2.11 the vector $\mathbf{r}$ describes the amount and the direction of the displacement. In the field of SAXS it is common to normalize the Patterson function resulting in the so called *correlation function* (Debye (1949)[61], Porod (1951)[62]),

$$\gamma(\mathbf{r}) \quad = \rho^{\star 2}(\mathbf{r}) / \rho^{\star 2}(0) \quad = P(\mathbf{r}) / \rho^{\star 2}(0). \tag{2.12}$$

Thus $\gamma(0) = 1$ which means that the correlation between a domain and its ghost is perfect, if the displacement is zero [60].

Generally, the structure of polymers can be considered to be made from domains which can be discriminated easily from each other by a sufficient difference of their electron densities (contrast). Examples are copolymers consisting of soft and hard domains, semi-crystalline polymers (crystalline phase is denser than the amorphous regions) and porosity(voids) within a material. In this case it is advantageous [46,60] to perform an edge enhancement by applying the Laplacian operator

$$z(\mathbf{r}) = \Delta P(\mathbf{r}) \tag{2.13}$$

instead of directly studying the correlation function. This results in a 3D chord distribution function (CDF), $z(\mathbf{r})$, introduced by N. Stribeck in 2001[63,64]. The CDF is an extension of the one-dimensional chord distribution called interface distribution function (IDF), $g_1(r)$ originally proposed by Ruland[65–67] for the study of lamellar systems. The basic idea of this technique goes back to 1965, when Méring and Tchoubar [68–71] introduced the (radial) chord length distribution (CLD), $g(r)$.

The CDF will be further explored in the next section.

2.2.2 Chord Distribution Function

The multidimensional chord distribution function (CDF) is an advancement of the interface distribution function. CDF is adopted to the study of highly anisotropic

materials. The advantage of the CDF is that the only required assumption is a multi-phase structure [46,60]. This assumption is correct for most of polymeric materials. Thus the structure of the material is revealed in real space without any adjusting parameters. The main prerequisites for computing the CDF are "fiber-symmetry" and completeness of the data.

2.2.2.1 Step 1: Projection on the Representative Plane

For the analysis of the structure we are interested in a multidimensional image in real space but not in a projection of the structural image [46,60]. In reciprocal space, however, we have to perform a projection on the representative plane (s_1, s_3) of the fiber pattern (cf. Figure 2.2), and compute

$$\{I\}_2(s_1, s_3) = \int I(s_{12}, s_3)\, ds_2. \tag{2.14}$$

This step has two main advantages [46,60]. First, it converts the related visualization of structure from a smeared (projected) to a clear one. Second, it reduces noise in the pattern. The latter is due to the averaging nature of the integral. Thus it makes it possible to decrease the exposure-time during experiment and increase the time resolution of an in-situ structure study.

2.2.2.2 Step 2: Laplacian and Background Correction

The next step of a proposed solution[63] extracts the discrete scattering from the pattern which has already been subjected to the Laplacian in real space (cf. Eq. 2.7). For this purpose, first, an estimated density fluctuation background is subtracted. It is computed from the data points outside the inscribed circle of the image by the definition

$$I_{Fl}(s_{12}, s_3) = c_0 + c_{12}\, s_{12}^2 + c_3\, s_3^2. \tag{2.15}$$

This definition conforms to the rule that the density fluctuation background is expanded in even powers of the scattering vector [46,60]. After the subtraction, the discrete intensity is multiplied by $4\pi^2 s^2$. This multiplication is equivalent to the Laplacian[3] edge-enhancement operator, as is evidenced by double application of

[3] Here the negative sign is missing – but we are not interested to work with negative intensities and will take care for the sign later.

the derivative theorem.

Now a correction for the non-ideal character of the multiphase topology must be performed. In the classical analysis this is a manual evaluation step which results in the subtraction of a slowly varying background [46,72,73]. Here the background determination is replaced by the result of a low-pass filter, applied to the scattering image at the present state of evaluation [74].

2.2.2.3 Step3: Fourier Transform

After background subtraction, an interference function $G_2(s_1, s_3)$ is obtained. Its 2D Fourier transform,

$$z(r_1, r_3) = -\mathscr{F}_2(G_2(s_1, s_3)), \tag{2.16}$$

is the sought after multidimensional chord distribution function. Because of fiber symmetry, the plane (r_1, r_3) is representative for the 3D structure [46,60], hence it is permitted to identify $r_1 \to r_{12}$. Thus $z(r_{12}, r_3)$ has been computed.

2.2.2.4 Relation Between a CDF and IDFs

Every radial, 1D slice through the center of a CDF

$$\lceil z \rceil_1 (r_{\psi,\varphi}) \quad = \quad g_1 (r_{\psi,\varphi}) \tag{2.17}$$

is an IDF [46]. In the above equation, the slicing direction is indicated by a polar and an azimuthal angle, ψ and φ, respectively. Of especial practical interest for the study of materials with fiber symmetry is the cut of the CDF along the meridian (fiber axis),

$$\lceil z \rceil_1 (r_3) = z(0, r_3) = g_1 (r_3). \tag{2.18}$$

$z(0, r_3)$ describes the longitudinal structure of the material. In analogy the transverse structure is described by the slice

$$\lceil z \rceil_2 (r_{12}) = z(0, r_{12}) = g_2 (r_{12}) \tag{2.19}$$

of the CDF.

2.2.3 Scattering Power

Another useful parameter for structure analysis is the well-known *scattering power*. It is the zero-dimensional projection of the scattered intensity [46] defined by

$$k = \{I\}_0 = \int I(\mathbf{s})\, d^3 s. \tag{2.20}$$

k is the total scattered intensity. After calibration to absolute units $I(\mathbf{s})$ turns into $I(\mathbf{s})/V$. Its scattering power is known as POROD's invariant:

$$Q = k/V \tag{2.21}$$

Q contains the non-topological structure parameters of the material's nanostructure. This means that Q depends only on the composition and contrast of the phases and not on their arrangement and shape. For multiphase systems this fact can be deduced by application of the Fourier-slice theorem and the considerations which lead to POROD's law [46]. In particular, by applying Fourier-slice theorem one obtains

$$Q = v(1-v)\,(\rho_1 - \rho_2)^2 + X \tag{2.22}$$

for a two-phase system. v is volume fraction of one of the phases, and $\rho_1 - \rho_2$ is the electron density contrast between the two phases. X is an unknown parameter arising from the scattering of voids, crazes, fillers or impurities within the material.

Chapter III

Experimental part

3.1 SAXS Setup

Three types of materials are studied in order to cover a relatively wide range of materials with different structures and properties. Samples are subjected to uniaxial deformation and the nanostructure evolution is monitored by SAXS. Figure 3.1 presents schematically the experimental setup. Small-angle X-ray scattering (SAXS) is carried out at the synchrotron beamline A2 at HASYLAB, Hamburg, Germany. The X-ray path is perpendicular to the sample. The sample-detector distance for a SAXS study is generally about 2000-3100 mm. The wavelength of radiation is 0.15 nm. Scattering intensity is collected by a 2D marccd 165 detector (mar research, Norderstedt, Germany) in binned 1024 $\times$ 1024 pixel mode (pixel size: 158.2 µm $\times$ 158.2 µm). Thus for the typical long period of 20 nm a variation of the peak position by one pixel causes a long period variation of below 1 %. The intensities of the primary beam before the sample and of the transmitted beam after the sample are recorded in order to calculate the absorption factor of the material.

Tensile testing is done in a home-made [75] stretching-machine. The machine performs symmetric drawing in order to maintain the position of the beam on the sample. Signals from load cell and transducer are recorded during the experiment. The macroscopic deformation is determined close to the beam position to ensure accurate comparison of the mechanical data with the nanostructure evolution. For this reason a precise method has been developed [76]. In this method a pattern of fiducial marks is stamped on the sample. The sample is monitored by a TV-camera. Using the fiducial marks the local strain $\varepsilon = (\ell - \ell_0)/\ell_0$ is computed automatically from the average initial distance, ℓ_0, of the fiducial marks and the respective actual distance, ℓ. More details will be presented in Chapter 4.

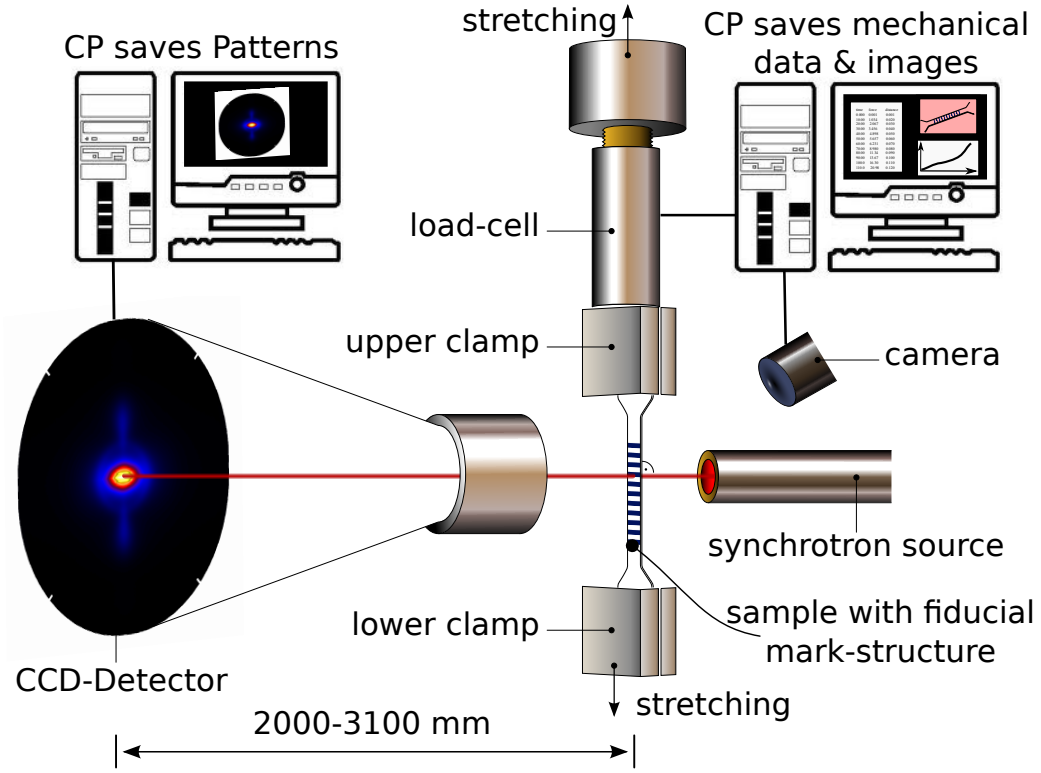

Figure 3.1: Schematic presentation of the experimental setup used for in-situ SAXS measurements during mechanical deformation. The original drawing has been provided by Courtesy of C. Schloen

Details about the sample preparation and experimental conditions of each group of the studied materials are presented in the following three sections.

3.2 Thermoplastic Polyurethane Elastomers

Material. A thermoplastic polyurethane (TPU) is injection molded from melts of different temperature. The material is a commercial grade polyester based thermoplastic polyurethane (TPU) with 94 Shore A durometer hardness from Huntsman Inc., e.g. for sealing applications. The TPU has been polymerized in a one-step process and is provided in granular form ground from cast film.

Injection molding.[1] Samples for the SAXS measurements have been processed directly from the received material. Dumbbell shaped specimens type 5 A according to DIN ISO 527 are injection molded. The nominal dimensions in the central zone of the specimens are 4 mm $\times$ 1 mm. Injection molding is carried out in an Arburg 220 S Allrounder 150-30 from pellets dried at 90 °C for 4 h. The screw diameter is 15 mm. Specimens have been molded in a 2-cavity mold and gated with film gate (0.8 mm thick). The mold is kept at a temperature of 60 °C The injection speed has been set to 25 cm/s where the maximum injection pressure has been 1600 bar. Different kind of samples are produced, the temperature at the nozzle of the injection unit is set to 205 °C, 215 °C and 235 °C, respectively.

Test bar characterization.[2] The injection-molded test bars are characterized by optical microscopy and by differential scanning calorimetry (DSC). Light microscopy is carried out in a Zeiss Axioplan 2 equipped with an AxioCam camera. The specimens are cross-sections cut from the centers of the test bars. They are 10 µm thick. Slicing is carried out at -70°C using a rotary cryo-microtome Leica RM 2165. A Mettler–Toledo DSC 821^e is employed. Sample mass is 5.0 ± 0.1 mg. The samples are studied under nitrogen flux, cooled to -100 °C and heated to 280 °C at a rate of 20 K/min.

[1] This part has been done by A. Frick et al. at IPSP, Aalen University.

[2] This part has been done by A. Frick et al. at IPSP, Aalen University.

Table 3.1: PP/MMT Nanocomposites based on metallocene polypropylene (PP) – HM562S (LyondellBasell) and montmorillonite (MMT) (Laviosa). The compatibilizer is an amphiphilic block copolymer (ABC)

sample	composition
PP	pure polypropylene
PP+MMT	PP + 3 wt.-% freeze-dried MMT
PP+lcMMT	PP + (3 wt.-% MMT + 4.65% ABC)
PP+hcMMT	PP + (3 wt.-% MMT + 8.0% ABC)

In-situ SAXS-stretch measurements. The clamping distance is 45 mm. A 500 N load cell is used. Continuous stretching is performed at cross-head velocity of 1 mm/min for the monitoring of SAXS. Video frames are grabbed every 10 s. The sample-detector distance is 2488 mm. The cycle-time is 60 s (50 s exposure).

3.3 Polypropylene/Montmorillonite Nanocomposites

Materials. Nanocomposites from metallocene polypropylene (HM562S, LyondellBasell) and nanoclay (hydrophilic montmorillonite, MMT) are studied. The MMT is obtained from Laviosa Chimica Mineraria, Italy (3.8 wt.-% aq. dispersion of montmorillonite). A compatibilizer is added to two of the materials in order to intercalate the MMT. The compatibilizer is an amphiphilic block copolymer (ABC) made[3] by atom-transfer radical polymerization (ATRP) [77, 78]. It consists of a hydrophobic block of hydrogenated polybutadiene, i.e. poly(ethylene-co-1,2-butylene) monoalcohol (trade name: Kraton L-1203 from Kuraray Co., Japan) with molecular weight 7000 and PDI=1.05, and a hydrophilic block of quaternized dimethylaminoethyl methacrylate. Modified nanoclays with 4.7 and 8.0 wt.-% of the ABC have been prepared. Table 3.1 describes the composition of the studied materials. Sample PP is the pure polypropylene. Sample PP+MMT is a blend of polypropylene and the freeze-dried hydrophilic MMT. The samples PP+lcMMT and PP+hcMMT are composites that contain MMT with low compatibilizer amounts and high compatibilizer amounts, respectively. In order to prepare the nanocomposites, modified lcMMT and hcMMT have first been freeze-

[3] The compatibilizer has been prepared by K. Jankova et al. at Danish Polymer Center, Technical University of Denmark

dried and, second, blended[4] with the PP.

Test bars S2 according to DIN 53504 are injection molded in a MiniJet II (Thermo Scientific) from a melt of 200 °C. Mold temperature: 30 °C, molding pressure: 650 bar, molding time: 45 s. holding pressure: 100 bar. Holding time: 20 s. The cross-section of the parallel central part is ca. 4 mm × 2 mm.

In-situ SAXS-stretch measurements. The clamping distance is 45 mm. A 500 N load cell is used. The machine is operated at a cross-head speed of 0.5 mm/min. Video frames are grabbed every 10 s. In the continuous stretching experiments necking starts after a draw path of ca. 3.5 mm. The experiment is stopped after the neck is fully developed. In the load-cycling experiments the samples are pre-strained by 2 mm. After that the cycling starts. In each cycle the samples are strained by 1mm and retracted by the same draw-path thereafter. Thus strain-controlled load-cycling instead of stress-controlled cycling is performed. The sample-detector distance is 3031 mm. Scattering patterns are recorded every 30 s with an exposure of 20 s.

3.4 Microfibrillar Composites

Materials. Microfibrillar composite (MFC) precursors are made[5] from high density polyethylene (HDPE) as the matrix and polyamide 6 (PA6) or polyamide 12 (PA12) as the reinforcing phase. Two samples contain the commercial compatibilizer Yparex®8102. The HDPE is produced by Borealis [PE VS4531®; density 0.94 g/cm^3; melt flow index: 0.6 g/10 min (2.16 kg, 190 °C); melting point by DSC: 133 °C]. The PA6 is made by Lanxess [Durethan® B30S; density: 1.14 g/cm^3; melt volume flow rate: 110 cm^3/10 min (5 kg, 260 °C, ISO 1133); melting point by DSC: 220 °C]. The PA12 is produced by EMS-GRIVORY [Grilamid® L25; density: 1.01 g/cm^3; melting point by DSC: 178 °C; M_w= 60 kg/mol; M_n= 31 kg/mol]. Yparex®8102 is made by DSM. It is a copolymer of HDPE and maleic anhydride. Its melt flow index is 2.3 g/10min (2.16 kg, 190 °C); melting point by DSC: 125 °C; M_w= 120 kg/mol; M_n= 15 kg/mol. Quantities of granulate have been premixed in the proportions as indicated in Table 3.2.

[4] Blending has been performed by J. de Claville Christiansen et al. at Aalborg University.

[5] Samples have been prepared by Z. Denchev et al. at University of Minho

Table 3.2: Composition (in wt. %) of oriented blends. In the coding P6, P12, H and Y stand for polyamide 6, polyamide 12, HDPE, and the compatibilizer Yparex, respectively

sample code	PA6	PA12	HDPE	Yparex
P6HY(20/80/0)	20	—	80	0
P6HY(20/70/10)	20	—	70	10
P12HY(20/80/0)	—	20	80	0
P12HY(20/70/10)	—	20	70	10

Each mixture has been melt-blended in a laboratory twin-screw extruder. The extrudate has been cooled to 12 °C and a slight drawing has been applied in the first haul-off unit of the extruder line to stabilize the strand cross-section. Further drawing has been performed in the second haul-off unit after heating the strand in a water bath of 97-98 °C. A third haul-off unit has applied the last drawing causing the diameter of the strand to decrease from 2 mm (at the die out-let) to about 0.6-0.9 mm. Details concerning the principle of the preparation [79] and the design of the extruder line [80] have been published elsewhere.

In-situ SAXS-stretch measurements. Load-cycling tests are performed. After approaching different pre-strains (ca. 5.5% and ca. 8-10% engineering strain for low-cycling and high-cycling, respectively) the sample is cycled between two fixed distances of the cross-heads. In the experiments the strain rate, $\dot{\varepsilon}$, is close to $\pm 1.5 \times 10^{-4} s^{-1}$. Video frames are grabbed every 10 s. Sample-detector distance is 2542 mm. Scattering patterns are recorded every 30 s with an exposure time of 23 s.

Chapter IV

Data Evaluation

"*Method consists entirely in the order and disposition of the objects towards which our mental vision must be directed if we would find out any truth. We shall comply with it exactly if we reduce involved and obscure propositions step by step to those that are simpler, and then starting with the intuitive apprehension of all those that are absolutely simple, attempt to ascend to the knowledge of all others by precisely similar steps.*"

... René Descartes

In this chapter the data-evaluation procedures are discussed. Most of the data-evaluation steps are performed by programs[1] written in an image processing software, PV-WAVE®[81]. Computer programing is highly required due to the large number of recorded patterns. Most computer programs run automatically after adjustment to the actual experimental conditions. In some programs the user have to define a Region Of Interest (ROI) on the first image and afterwards the program runs automatically.

4.1 Evaluation of Mechanical Parameters

In order to correlate the macroscopic response of the material to its structure it is necessary to assess the deformation of the sample close to the beam position. For this purpose a method has been devised by Stribeck et al. [76]. A pattern of parallel fiducial marks is stamped on the sample. A video camera monitors the sample during deformation (Figure 4.1). This method gives precise values of the macroscopic elongation provided the sample is kept straight and the contrast among the

[1] All programs are freely available: http://www.chemie.uni-hamburg.de/tmc/stribeck/pv-wave/index_e.html

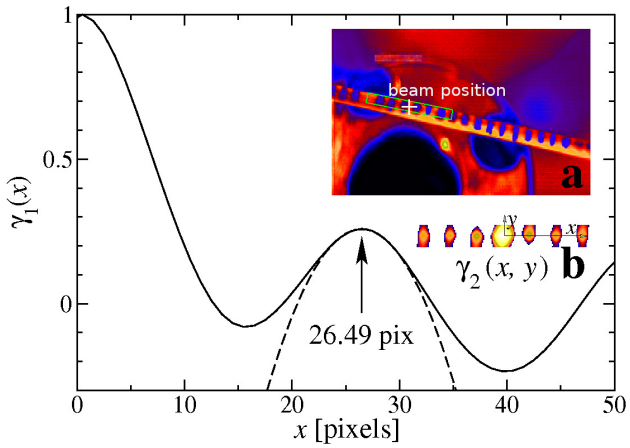

Figure 4.1: Elongation from recorded video frames. Inset **a**: In the first video frame a region of interest (ROI) with fiducial marks is defined. Inset **b**: From the ROI the 2D correlation function $\gamma_2(x,y)$ is computed. Main drawing: The center of the long period peak in $\gamma_1(x) = \gamma_2(x,0)$ is fitted by a parabola (dashed line) to compute the distance between the fiducial marks [76]

fiducial marks is sufficient. The pseudo-color representation provides good visual contrast. The center of the X-ray beam on the sample is marked by a cross in the image. Close to this center the user defines a rectangular region of interest (ROI), $\rho'_m(x,y)$. In Figure 4.1a this region is bordered by a dashed green line. x and y are pixel coordinates in the direction of strain and perpendicular to it, respectively. The same ROI is applied to all video frames of an experiment. The ROI is structured by the fiducial marks running perpendicular to the straining direction. As is known from scattering theory [46], the 2D correlation function

$$\gamma_2(x,y) = \frac{\rho_m^{\star 2}(x,y)}{\rho_m^{\star 2}(0,0)} \tag{4.1}$$

of a function $\rho_m(x,y)$ can be computed, with

$$\rho_m(x,y) = \rho'_m(x,y) - \bar{\rho}_m \tag{4.2}$$

representing the fluctuation of $\rho'_m(x,y)$ about its average $\bar{\rho}_m$. The autocorrelation is defined by the integral

$$f^{\star 2}(x,y) = \int\int_{-\infty}^{\infty} f(u,v)\, f(u+x, v+y)\, du dv. \tag{4.3}$$

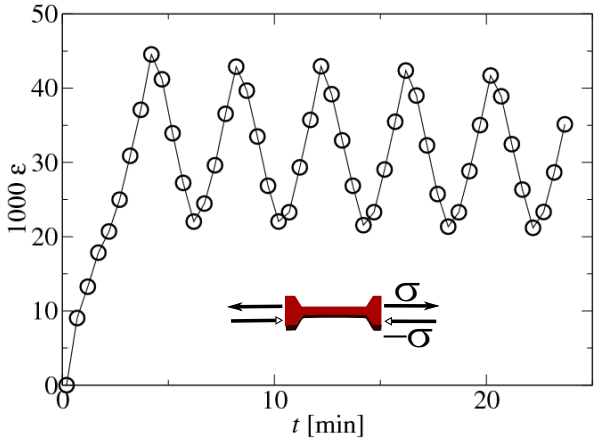

Figure 4.2: Accuracy of the correlation method is demonstrated by the macroscopic elongation $\varepsilon(t)$ determined in a load-cycling experiment

In Figure 4.1b the colored caps demonstrate, where $\gamma_2(x,y)$ is positive. Because bar-shaped marks have been affixed to the sample, only the macroscopic elongation ε in straining direction can be extracted from the section $\gamma_1(x) = \lceil \gamma_2(x,y) \rceil_1(x)$ of γ_2 in straining direction. Figure 4.1 presents this curve and its analysis. In analogy to the nomenclature of the scattering theory, the first positive peak is the long period peak which measures the actual average distance of the fiducial marks, ℓ. Using the 7 data points around the peak maximum, a parabola (dashed line) is fitted, and the position of its vertex is determined (arrow). Thus in our experiments ℓ is determined with an accuracy of 0.01 pixels. Let ℓ_0 be the initial distance between the marks, then the macroscopic strain is $\varepsilon = \ell/\ell_0 - 1$. The high accuracy reached is shown in Figure 4.2 by an $\varepsilon(t)$-curve recorded in a load-cycling experiment of one of the MFC samples. The estimated error is below 0.001. Nevertheless, it increases considerably if the contrast of the bar sequence is low (insufficient illumination) or if the sample is not straight in the beginning. The determination error may also increase after necking has occurred and the sample has begun to slide through the ROI.

Assuming constant volume during mechanical loading, the actual cross-section, $A(t)$, is calculated from

$$A(t) = \frac{A(0)}{\varepsilon(t) + 1}. \tag{4.4}$$

Here $A(0)$ is the initial cross section of the sample. Let $F(t)$ the actual force recorded by the tensile machine. Then the true stress, σ, is

$$\sigma(t) = \frac{F(t)}{A(t)}. \tag{4.5}$$

The true stress averaged over one cycle, $\bar{\sigma}$, is also calculated in order to assess fatigue in the load-cycling tests. The averaging is done by *running-average* command of Xmgrace[2].

4.2 Evaluation of Scattering Data

Evaluation of the SAXS patterns consists of three main stages. Stage I includes pre-evaluation of raw data. In stage II the fiber diagrams, CDFs and scattering power are computed. Stage III includes peak-analysis of the CDFs (or SAXS patterns) and extracting the desired nanostructural parameters.

4.2.1 Pre-evaluation of SAXS Data

All steps of data-evaluation are discussed in a text book [46]. Here the main concepts are briefly reviewed.

Normalization Scattering patterns and the background are divided by the actual incident flux measured by the first ionization chamber, and also by the actual exposure time. The former is necessary due to the decay of the incident beam flux after each injection at a synchrotron source, Figure 4.3.

Valid area masking. A mask is a matrix of ones and zeros. Every scattering pattern is multiplied by the mask. The results are images in which all invalid pixels are set to zero intensity. A mask is usually a combination of several masks each removing some of the invalid points. For instance, for SAXS patterns recorded at the beam-line A2 (HASYLAB) one needs to encircle the area of valid points (mask1), take out the beam stop (mask2) and the holder of the beam stop (mask3). The final mask is the multiplication of these three masks. For making mask1 an arbitrary image (usually the empty scattering or the first pattern of a series) is read

[2] see: http://plasma-gate.weizmann.ac.il/Grace/

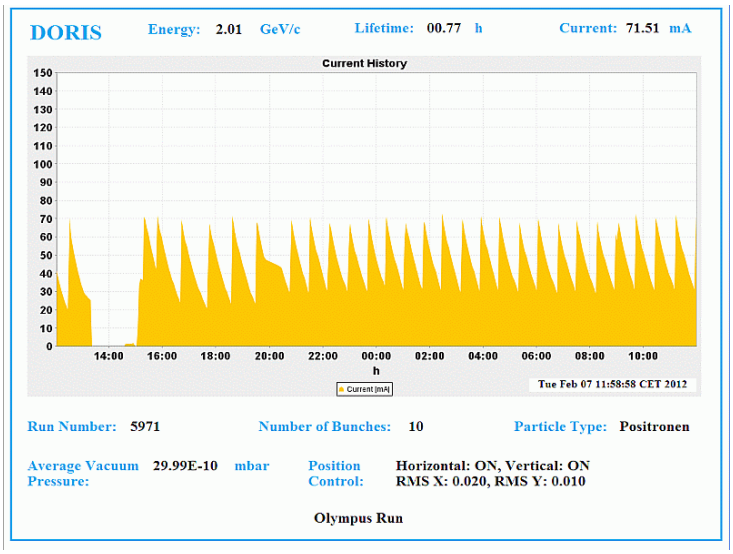

Figure 4.3: Decay of beam intensity at DORIS, HASYLAB, DESY

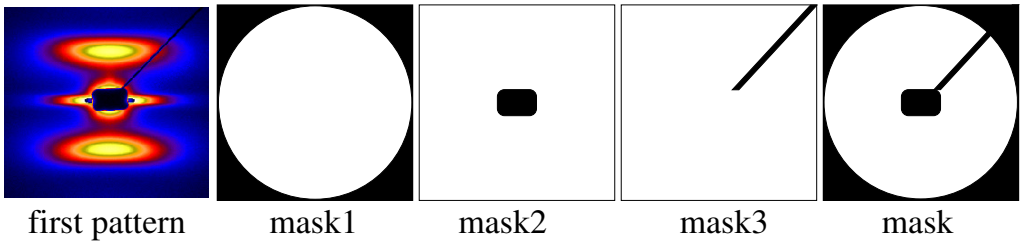

Figure 4.4: steps of making the mask. The final mask is a pattern of 0 and 1 values. Zeros and ones define the invalid and valid points, respectively

into a variable by calling the procedure *marget.pro*. mask1 is set equal to the pattern. Finally all points with an intensity lower than a threshold (0.1-0.5) are set to zero and the rest is set to one. mask2 and mask3 are obtained by calling *sf_filloutcircle.pro* and *sf_killbar.pro,* respectively. The edges of the final mask can be enhanced by calling *sf_erode.pro*. The steps are depicted in Figure 4.4.

wave> img=marget('leer01_000') ; *reading a pattern into the variable img*

wave> mask1=img

wave> mask1.map = img.map GT 0.1

wave> mask2=img

wave> mask2.map = img.map GT 20 ; *the position of the beam stop (center of the pattern) is roughly determined*

wave> sf_filloutcircle, mask2

wave> mask3=img

wave> sf_killbar,mask3,/logscale

wave> mask3.map = mask3.map GT 0 ; *all points out of the beam-stop holder are set to 1*

wave> mask=mask1

wave> mask.map=mask1.map*mask2.map*mask3.map

wave> sf_erode, mask, 7 ; *Here 7 determines the degree of eroding*

Absorption and background correction. The amount of matter irradiated by the X-ray varies during an in-situ SAXS measurement. Moreover, the matter causes both scattering and absorption of the X-ray. Therefore, it is necessary to correct the absorption effects. In practice absorption correction is done based on two flux measurements by means of ionization chambers, one placed before (I_1), and the other behind (I_2) the sample [46]. If $I_{1,0}$ is the reading of the first ionization chamber during a measurement of parasitic background and $I_{1,s}$ is the reading during sample measurement with the analogous nomenclature for the reading of the second ionization chamber then

$$\exp(-\mu t) \approx \frac{I_{2,s} I_{1,0}}{I_{2,0} I_{1,s}} \tag{4.6}$$

is approximately valid. μ is the linear absorption coefficient and t is the sample thickness. The measurement of the incident flux I_1 is only necessary due to the variation of the flux of the synchrotron radiation sources. After absorption correction the machine background (empty scattering) is subtracted.

Alignment. The center of gravity of the primary beam is moved into the center of the image matrix [46]. In addition, in the case of anisotropic scattering patterns, the meridian is aligned in vertical direction. Thus the parameter set of the operation is made from the position of the true center, (x_c, y_c), on the raw image measured in raw pixel coordinates and from an angle of image rotation, φ . If these parameters are known and the sample does not rotate during the experiment, all frames of the experiment can be centered and aligned using the same set. This is usually true during a tensile test.

Harmony. If there is uniaxial symmetry and the fiber axis is in the detector plane, the scattering pattern can be divided into four quadrants [46]. Each quadrant carries identical information. This means that there is some harmony in the scattering pattern. Thus the missing data of one quadrant (e.g. the shadow of the beam-stop holder) can be reconstructed using the data of other quadrants. The remaining central blind hole is filled applying a stiff parabolic extrapolation[82].

A series of patterns are aligned, harmonized and background corrected by:

```
wave> alltifftoima, 'series_name'
```

The result is a series of harmonized fiber-diagrams.

4.2.2 Computing CDFs

CDFs are computed from harmonized patterns by calling *allalign2cdf.pro*. The harmonized fiber-diagram pattern is projected on the representative fiber-plane (s_1, s_3). In PV-WAVE® it is done by calling *sf_fibproj.pro*. Multiplication by s^2 applies the real-space Laplacian. The density fluctuation background determined by low-pass filtering is eliminated by subtraction. The resulting interference function, $G(s_{12}, s_3)$, describes the ideal multiphase system. Its 2D Fourier transform is the chord distribution function (CDF) [63], $z(r_{12}, r_3)$.

The main steps from the recorded pattern toward the CDFs are schematically depicted in Figure 4.5. It shows a representative recorded SAXS pattern, the corrected fiber diagram $I(s_{12}, s_3)$, absolute values of the CDF $|z(r_{12}, r_3)|$ and a slice of the CDF along the meridian, $z(0, r_3)$. Plotting the $z(0, r_3)$ curve is the easiest way of analyzing the structure along the principal axis of the material (injection-molding direction).

4.2.2.1 Automated 2D Peak Analysis of CDFs

The multidimensional CDF $z(\mathbf{r})$ shows peaks wherever there are *domain surface contacts* between domains in $\rho(\mathbf{r})$ and in its displaced ghost. Such peaks $h_i(r_{12}, r_3)$ are called[65] distance distributions. Distance is the ghost displacement. It is sometimes useful to replace the index i by a sequence of indexes that indicate the sequence of domains that have been passed along the displacement path until the considered domain surface contact occurs. For instance $h_{ca}(r_{12}, r_3)$ indicates

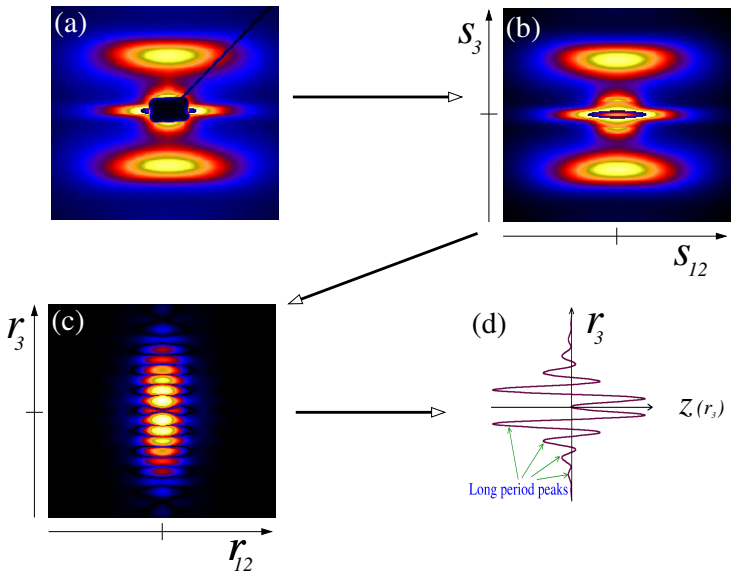

Figure 4.5: Representative X-ray scattering data of oriented polymers (e.g. MFC precursors): (**a**) the recorded SAXS pattern. The blind area arises from the shadow of the primary beam-stop (**b**) the corrected fiber diagram $I(s_{12}, s_3)$, (**c**) absolute value of the CDF $|z(r_{12}, r_3)|$, and (d) a one-dimensional slice of the CDF along the meridian $z(0, r_3)$ showing the negative long period peaks and the positive peaks (above the r_3-axis). Image intensities on logarithmic scale. Displayed regions: $-0.1\,\mathrm{nm}^{-1} < s_{12}, s_3 < 0.1\,\mathrm{nm}^{-1}$, $-100\,\mathrm{nm} < r_{12}, r_3 < 100\,\mathrm{nm}$. The s_3- and r_3-axes match the stretching direction of the sample

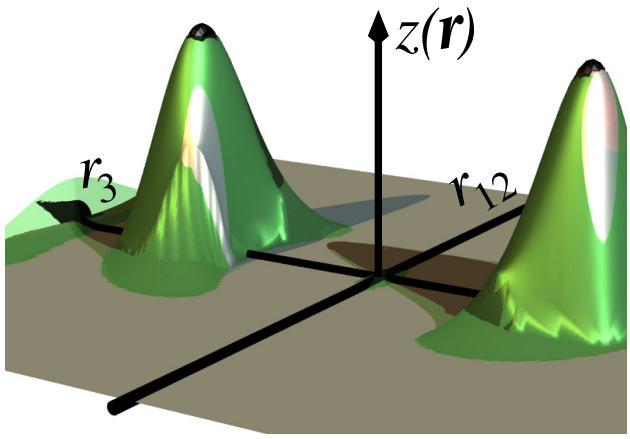

Figure 4.6: Demonstration of bivariate polynomial fitting (linear intensity scale). The measured surface is visualized as glass material. The metal-material surface is the fitted polynomial. Its computation considers all points in a cap (in black) that are above 95% of the peak maximum [76]

the passing of an amorphous and a crystalline domain. Thus this peak is a long period peak. h_{ca} will be used, if the displacement is in the direction of strain. h_{ba}[3] will be used, if the displacement is in the lateral direction (i.e. transverse to strain).

The peak-analysis is done by fitting a bivariate polynomial to the cap of the peak in order to determine its position and the standard deviations that describe the peak widths in equatorial and meridional directions [42, 76]. Let the y-direction be the meridian, in analogy to the correlation method, a ROI is defined by the user. Inside this ROI the algorithm searches for the peak. The 2D peak is fitted to a 2D function. Figure 4.6 demonstrates the fit of the long period peak by a bivariate quadratic polynomial. In order to assure numerical stability of the regression module on digital computers, the maximum intensity in the measured peak data is normalized to 1.

Like in the correlation method, a set of measured data points is fed to a regression algorithm [42, 76]. Instead of the 7 highest points of a 1D peak, now all those points in a cap are used, whose intensity is above a user-defined level. The 1D quadratic polynomial from the correlation method is replaced by a 2D (bivariate)

[3] where b indicates the width of a block in analogy with the notion of Strobl's block structure [83, 84] observed during crystallization of polypropylene.

polynomial of 2nd degree. An n-th degree bivariate polynomial

$$f\left(x',y'\right)=\sum_{i,j=0}^{n}\mathbf{C}'_{ij}\left(x'\right)^{i}\left(y'\right)^{j}$$

in the image coordinates x' and y' is defined by its coefficient matrix $\mathbf{C}'$. Let the center of gravity of the fitted polynomial be $\left(x'_g,y'_g\right)$, then central coordinates are defined by $x=x'-x'_g$ and $y=y'-y'_g$. The fitting of 2D data by a bivariate polynomial is a standard method [85]. In the programming environment PV-WAVE® this is done by utilizing the library module `POLYWARP.PRO` and linking it into our routine `sf_peakfit.pro`. `sf_peakfit` returns the peak center and the 3×3 coefficient matrix $\mathbf{C}$ in the central coordinate system. It is assumed that the profile of the peak in the principal directions x (r_{12}) and y (r_3) can be approximated by Gaussians. Peak widths of Gaussians are characterized by their standard deviations σ, which are readily expressed in terms of the coefficients of $\mathbf{C}$

$$\sigma_{12x}=\sigma_x=\sqrt{\frac{\mathbf{C}_{0,0}}{2\,\mathbf{C}_{2,0}}},\quad \sigma_3=\sigma_y=\sqrt{\frac{\mathbf{C}_{0,0}}{2\,\mathbf{C}_{0,2}}} \tag{4.7}$$

from the series expansion of the Gaussians (routines: `sf_anapeaks.pro`, `sf_anapeakso.pro`). Here σ_x and σ_y measure the extension of the peak in x- and y-direction, respectively.

Taken a meridional long period distribution peak $h_{ca}\left(r_{12},r_3\right)$, three parameters are extracted and discussed: L is its maximum and defines the most probable long period, $\sigma_3\left(h_{ca}\right)$ and $\sigma_{12}\left(h_{ca}\right)$ are its standard deviations in the meridional and equatorial directions, respectively. Thus $\Delta L=3\,\sigma_3\left(h_{ca}\right)$ is a measure of the long period distribution or heterogeneity of the stacking of crystalline and amorphous domains. $e_{12}=3\,\sigma_3\left(h_{ca}\right)$ measures the lateral extension of lamellae . Similarly, L_b is the maximum of $h_{ba}\left(r_{12},r_3\right)$ and defines the most probable long period of a transverse structure. Thus $\Delta L_b=3\,\sigma_{12}\left(h_{ba}\right)$ is the breadth of $h_{ba}\left(r_{12},r_3\right)$ in equatorial r_{12}-direction. $H_b=3\,\sigma_3\left(h_{ba}\right)$ is the height of $h_{ba}\left(r_{12},r_3\right)$ in meridional r_3-direction.

The long period L measures the distance in straining direction between neighboring crystallites. Let $L(t)$ the long period at time t, and $L_0=L(0)$ the long

period at the beginning of a deformation experiment, then a nanoscopic strain

$$\varepsilon_n(t) = \frac{L(t)}{L(0)} - 1 \tag{4.8}$$

can be defined [11,76].

Similarly a lateral nanoscopic strain $\varepsilon_{n,l}$ can be estimated based on the variations of e_{12}:

$$\varepsilon_{n,l}(t) = \frac{e_{12}(t)}{e_{12}(0)} - 1$$

4.2.3 Computing the Scattering Power

From the oriented scattering pattern we compute the scattering power Q of the ideal semicrystalline morphology (no density fluctuations within the domains, no density transition zone between the domains) [46]. For this purpose we start from $G(s_{12}, s_3)$ and extract the scattering intensity $I_{id}(\mathbf{s})$ of the ideal semicrystalline morphology. Then $\{I_{id}\}(s_1, s_3) = \int I_{id}(s_1, s_2, s_3)\, ds_3$ is computed. The equation presents the definition of the projection operation. $\{I_{id}\}(s_1, s_3)$ is the scattering intensity of the ideal multiphase system projected on the representative s_{13}-plane of fiber symmetry [46]. From $\{I_{id}\}(s_1, s_3)$ the scattering power

$$Q = \int\int \{I_{id}\}(s_1, s_3)\, ds_1 ds_3 \tag{4.9}$$

is directly computed. Q is normalized with respect to the irradiated volume, because of the respective normalization of $I(\mathbf{s})$. As mentioned before the predominant contribution [46,50,86–88] to the invariant originates from the two-phase nanostructure of the studied semi-crystalline polymers (cf. Eq. 2.22).

4.2.4 Computing Isotropic Scattering

In order to relate changing Q to structure evolution it is helpful to know where the scattering intensity is changing. In general, the presentation of variations in *images* $\{I_{id}\}(s_1, s_3)$ is difficult, but if the intention is a discrimination between, e.g., void formation and change of the semicrystalline structure, an isotropic scattering *curve* $I(s)$ can be utilized. From $\{I_{id}\}(s_1, s_3) = \{I_{id}\}(s, \phi)$ an isotropic scattering

curve

$$4\pi s^2 I(s) = \int_0^{2\pi} \{I_{id}\}(s,\phi)\, d\phi. \tag{4.10}$$

is obtained by circular integration of $\{I_{id}\}(s,\phi)\, d\phi$ with respect to the polar angle ϕ in the s_{13}-plane. Of course, further integration with respect to s yields the scattering power. Thus it appears reasonable to inspect the integrand $s^2 I(s)$ in order to determine which angular regime is responsible for observed changes in Q.

Chapter V

Thermoplastic Polyurethane Elastomers Under Uniaxial Deformation

The special rubber elastic properties of thermoplastic elastomers are the result of their two- or multi-phase nanostructure consisting of hard domains in a soft matrix. The hard domains form physical cross-links and make the material behave rubber elastic. The soft phase between two hard domains is called soft domain (Figure 5.1). The formation of nanostructure during manufacture is initiated by phase separation, while the polymer melt is cooling down. Phase separation occurs, because the polymer chains are composed from at least two blocks of different chemical composition that are immiscible at the service temperature of the material. Block copolymers synthesized by living polymerization are characterized by uniform block lengths. Processing of such compounds may result in lattice-like nanostructures or even in photonic crystals, in which the soft and the hard blocks reside completely in different domains. This is different with thermoplastic polyurethanes (TPU). Along their chains a mixed sequence of soft segments and hard segments is found. Thus, even optimum process control only leads to domains of very diverse shape and size, the arrangement of which can rarely lead to lattice-like correlation. Moreover, soft domains may contain several hard segments. Consequently, the chemistry [89] and the processing conditions [90–93] define the nanostructure that, in turn, determines the material's mechanical properties. In this chapter we study oriented injection-molded TPU materials during tensile test. In doing so, the focus is on the still little investigated [90–93] effect of processing conditions on the structure and the properties of the material.

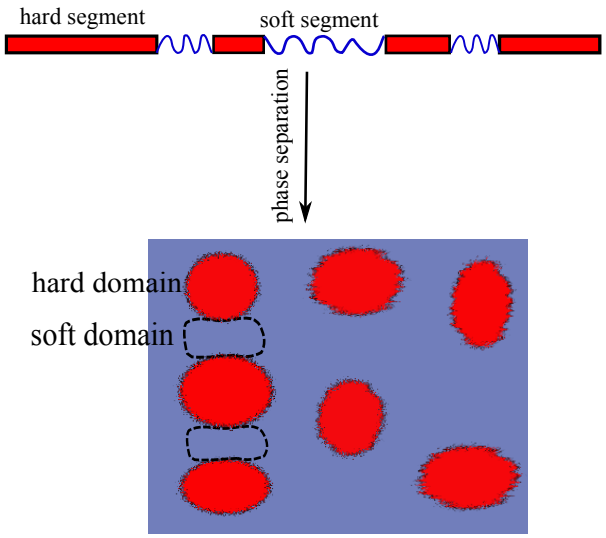

Figure 5.1: Schematic presentation of microstructure of TPU materials. TPU chains are formed by alternating sequences of hard and soft segments. Upon cooling from the melt state, TPU materials undergo phase separation resulting in a (multi)two-phase morphology. The hard domains act as physical cross-links. The soft matrix between two alternating hard domains is called soft domain

5.1 Optical Microscopy

Figure 5.2 presents optical micrographs of the injection-molded materials. The material processed at 205 °C shows a high fraction of spherulitic material. In the material processed at 215 °C the fraction is considerably lower. In the material made from the hottest melt no spherulites are detected. Generally spherulites grow during polymer crystallization. Spherulites consist of alternating crystalline and amorphous layers (cf. Figure 1.2). In TPUs the amorphous layers are formed by soft domains, and the hard domains are not completely crystalline, but only quasi-crystalline [94]. This conclusion is drawn because the melt enthalpies of TPUs are commonly low [94–96].

5.2 DSC Measurements

DSC data of the raw pellets and of the injection molded samples are presented in Figure 5.3. The part between 50 °C and 280 °C is shown. Below 50 °C the curves are featureless. All samples exhibit two endothermic peaks. They are attributed

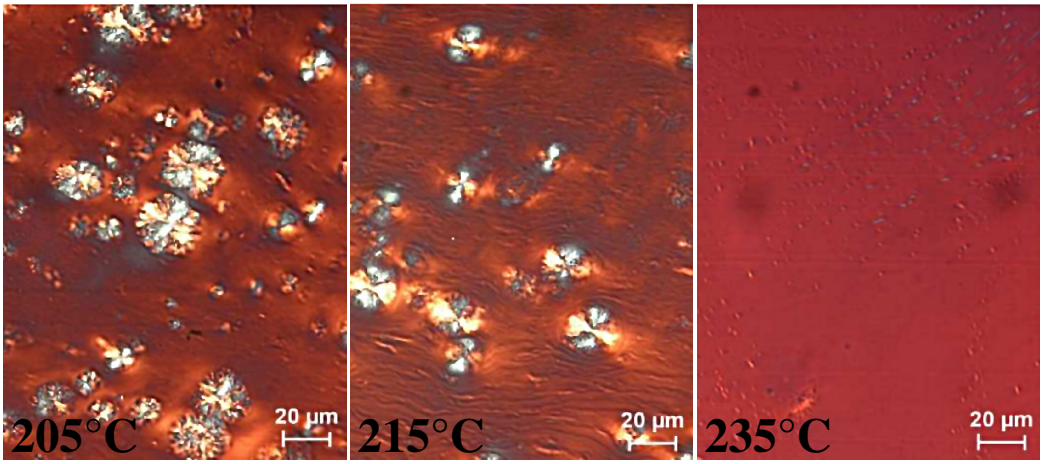

Figure 5.2: Optical micrographs of cross sections (10 µm thickness, cryo-microtome -70 °C) from the central zone of injection molded test bars. Labels indicate the temperature of the injected melt

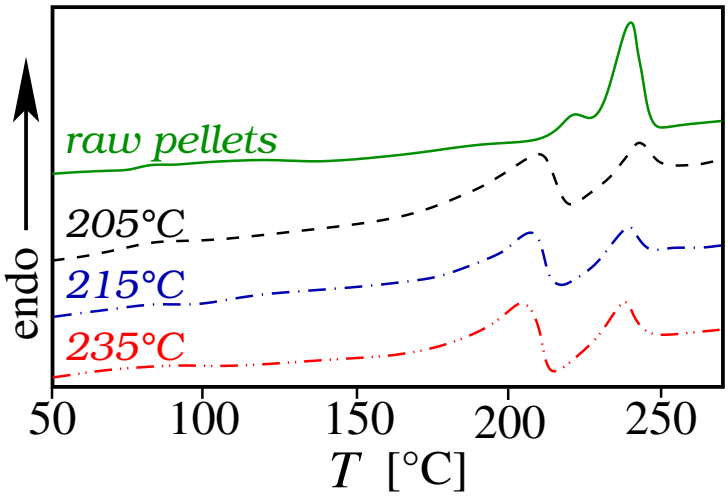

Figure 5.3: DSC traces of TPU material before (raw pellets) and after injection molding. The labels at the dashed curves indicate the temperature of the injected melt

Table 5.1: Melt enthalpies, ΔH_m and melting temperatures, T_m from the DSC scans in Figure 5.3. Peak 1 is the low temperature peak. The processed materials are labeled with the temperature of the injected melt

	Peak 1		Peak 2	
sample	ΔH_m [J/g]	T_m [°C]	ΔH_m [J/g]	T_m [°C]
TPU_raw	3.0	211	15.2	237
TPU_205	10.6	207	3.8	240
TPU_215	6.8	206	3.0	239
TPU_235	10.9	202	4.3	237

to the special morphology of thermoplastic polyurethanes. It consists of hard domains in a soft-domain matrix. The hard domains sometimes form spherulites (cf. Figure 5.2). The hard domains may contain some soft segments. This is due to the multi-block nature of the TPU materials studied here. Inside the hard domains some proximate hard segments are merged into small crystals. Among the hard segments of the crystals hydrogen bonds are formed. The first endothermic peak has been associated [95] with the melting of the small crystals. The second peak has been related [95] to the mixing of hard and soft segments from hard and soft domains to form a single-phase melt. Another explanation for the upper endothermic peak would additionally require the formation of a second crystalline polymorph, as has been reported with non hydrogen-bond forming TPUs [97]. The melt enthalpies and melting points are listed in Table 5.1. Uncertainties of the enthalpy determinations are ± 0.3 J/g. Melting temperatures have been determined with an uncertainty of ± 0.4 K. Considering the processed materials as a function of the injection temperature, ΔH_m does not show a trend. T_m decreases as a function of increasing injection temperature. This implies a decrease of the average crystallite size.

5.3 Mechanical Data

The tensile tests in the synchrotron beam have been carried out at constant crosshead speeds of (1 mm/s). The stress-strain curves recorded during the experiments are shown in Figure 5.4. The SAXS tests have been stopped when the samples slipped from the clamps. Obviously, the stiffness of the material decreases with

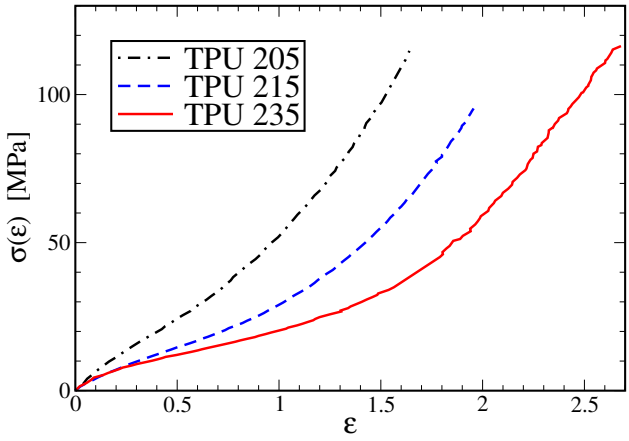

Figure 5.4: TPU samples strained during the scattering experiments. Stress–strain curve, $\sigma(\varepsilon)$

increasing processing temperature. This can be attributed to the higher amount of crystals at lower processing temperatures.

5.4 Measured SAXS

Representative SAXS patterns recorded during stretching experiments of TPU materials are shown in Figure 5.5 – Figure 5.7. Patterns in the figures are scaled logarithmically. They have identical intensity scales. The nanostructure of all the materials shows remarkable orientation already before deformation. The tough, mature test bars used in the SAXS experiments have slipped from the clamps after having been exposed to a stress $\sigma \approx 100$ MPa. Figure 5.5 shows the scattering patterns taken during the straining of sample TPU 205 that had been injection molded from a melt of 205 °C. The lateral extension of the reflections is broad from the beginning, indicating that the arranged hard domains do not exhibit the shape of extended lamellae, but only of moderately anisotropic domains that arrange to form microfibrils [98–100]. With increasing strain an increase of the reflection intensity is observed until $\varepsilon \approx 0.25$. Thereafter the reflection intensity is decreasing. During the test the maximum position of the reflection is moving towards the center of the pattern indicating an increasing distance between the hard domains.

Figure 5.6 shows selected SAXS patterns from the monitoring of the material that has been injection molded from a melt of 215 °C. A microfibrillar nanostructure with increasing distance between the hard domains is observed. The reflec-

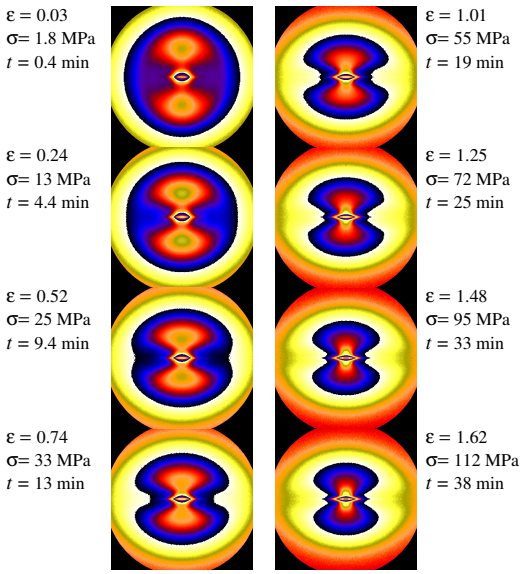

Figure 5.5: TPU 205. Measured SAXS intensity during the tensile test. The pseudo-color fiber patterns $I(s_{12}, s_3)$ show the region $-0.2\,\mathrm{nm}^{-1} \leq s_{12}, s_3 \leq 0.2\,\mathrm{nm}^{-1}$. Pattern intensities on a logarithmic scale. Cross-head speed is 2 mm/s. Straining direction is vertical

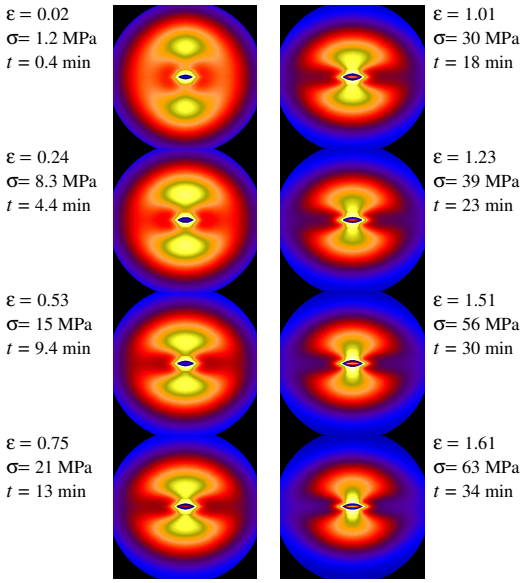

Figure 5.6: TPU 215. Measured SAXS intensity during the tensile test. The pseudo-color fiber patterns $I(s_{12}, s_3)$ show the region $-0.2\,\mathrm{nm}^{-1} \leq s_{12}, s_3 \leq 0.2\,\mathrm{nm}^{-1}$. Pattern intensities on a logarithmic scale. Cross-head speed is 1 mm/s. Straining direction is vertical

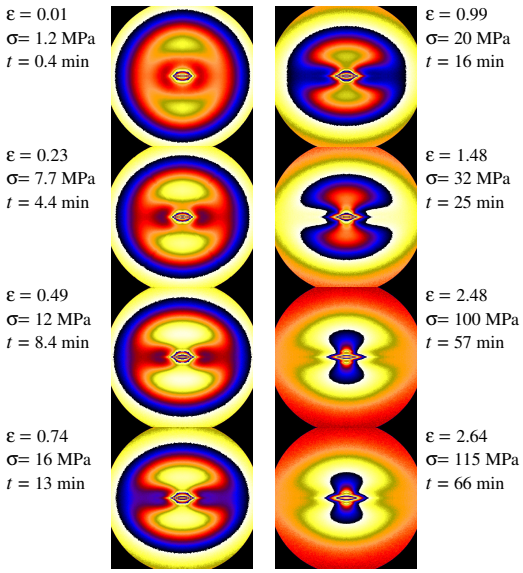

Figure 5.7: TPU 235. Measured SAXS intensity during the tensile test. The pseudo-color fiber patterns $I(s_{12}, s_3)$ show the region $-0.2\,\mathrm{nm}^{-1} \leq s_{12}, s_3 \leq 0.2\,\mathrm{nm}^{-1}$. Pattern intensities on a logarithmic scale. Cross-head speed is 1 mm/s. Straining direction is vertical

tion intensity maximum is first increasing with increasing strain (up to $\varepsilon \approx 0.5$). Thereafter it is decreasing.

Figure 5.7 shows selected SAXS patterns from the monitoring of the material that has been injection molded from a melt of 235 °C. A microfibrillar nanostructure with increasing distance between the hard domains is observed. The reflection intensity maximum is first increasing with increasing strain (up to $\varepsilon \approx 0.7$). Thereafter it is decreasing.

5.5 Nanostructure in Real Space (CDF)

Multidimensional chord distribution functions [46,63] (CDF) visualize the nanostructure of the studied materials and its evolution in real space, Figure 5.8 – Figure 5.10. The general course of the peak intensities in the CDFs is identical to the development observed in the SAXS patterns. The materials exhibit an initial increase of peak intensities that is followed by a decrease for higher strain.

Already in the unstrained materials the CDF peaks are only moderately extended in horizontal direction, which is the direction perpendicular to the strain. This means that the corresponding hard domains show only a moderate lateral

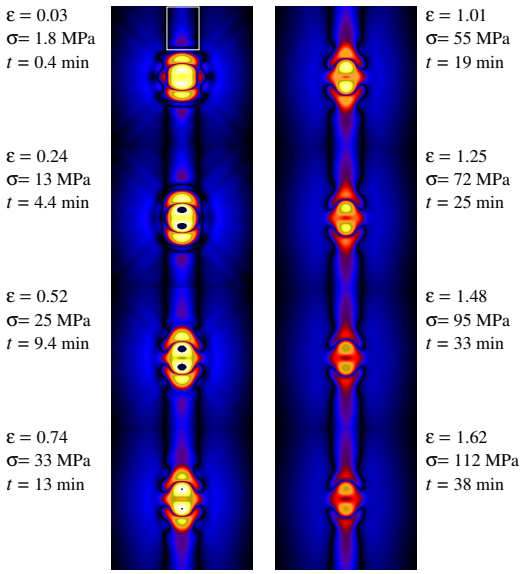

Figure 5.8: Tensile test of TPU 205. Chord distribution functions (CDF) computed from SAXS. The pseudo-color fiber patterns $|z(r_{12}, r_3)|$ show the region $-50\,\text{nm} \leq r_{12}, r_3 \leq 50\,\text{nm}$. Straining direction is vertical. Pattern intensities on a logarithmic scale. Cross-head speed is 2 mm/s. A white border indicates the region used in Figure 5.12–5.14

extension that decreases somewhat with increasing strain. Thus the hard domains cannot be addressed "lamellae" from the beginning, but only "anisotropic granules" that degrade with increasing strain becoming less and less extended. This is the well-known transition process from layer stacks to microfibrillar stacks [99, 100].

Figure 5.8 shows selected CDFs from the monitoring of the material that has been injection molded from a melt of 205 °C. A clean microfibrillar nanostructure with increasing distance between the hard domains is observed. Only few peaks are noticed on the meridian. Because there is no peak outside a distance of 50 nm, the correlation distance among the hard domains is lower than 50 nm. The peaks exhibit a peculiar skewed shape.

Figure 5.9 shows selected CDFs from the monitoring of the mechanical test of sample TPU 215, the material injection molded from a melt of 215 °C. Similar to TPU 205 the domain peak intensity of the material first increases after the start of the straining (developing dark spots in the center of the peaks) and falls below the initial value thereafter. Similar to TPU 205 the tough material slips from the clamps rather early.

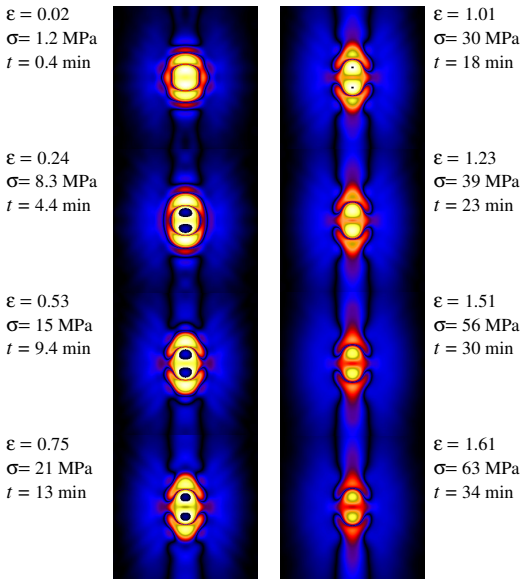

Figure 5.9: Tensile test of TPU 215. Chord distribution functions (CDF) computed from SAXS. The pseudo-color fiber patterns $|z(r_{12}, r_3)|$ show the region $-50\,\text{nm} \leq r_{12}, r_3 \leq 50\,\text{nm}$.. Straining direction is vertical. Pattern intensities on a logarithmic scale. Cross-head speed is 1 mm/s

Figure 5.10 presents the nanostructure evolution during the mechanical test for the material injection molded from the hottest melt (235 °C). A plain microfibrillar pattern is observed from the beginning. During the test the microfibrils narrow (vertical bar-shaped reflections move closer to the meridian), and the intensity in the central meridional streak is changing. An ordinary nanostructure and its response to strain is not observed. An ordinary nanostructure would exhibit distinct peaks along the meridian that clearly move outward with increasing strain instead of a meridional streak. In other materials that are studied in straining tests (cf. Chapters 6 and 7) we have observed such distinct peaks moving. They indicate a well-defined preferential distance between hard domains instead of an extremely broad distribution of distances. Nevertheless, let us relate the position of the peak maximum on the meridian of the CDF to its initial position and discuss it. Is this quantity an adequate measure for a nanoscopic strain with the studied segmented TPU material?

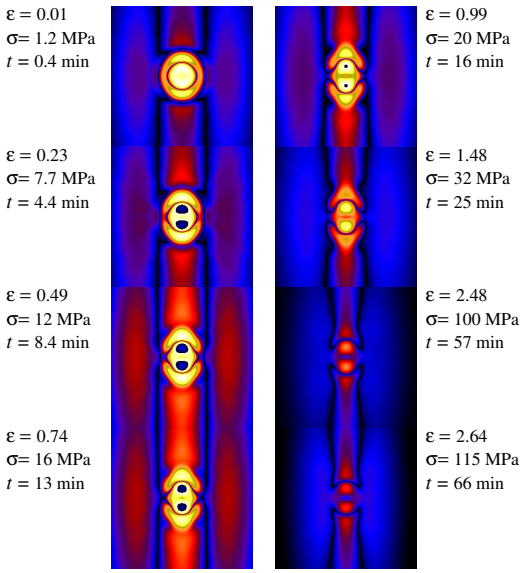

Figure 5.10: Tensile test of TPU 235. Chord distribution functions (CDF) computed from SAXS. The pseudo-color fiber patterns $|z(r_{12}, r_3)|$ show the region $-50\,\text{nm} \leq r_{12}, r_3 \leq 50\,\text{nm}$.. Straining direction is vertical. Pattern intensities on a logarithmic scale. Cross-head speed is 1 mm/s

5.6 Macroscopic and Nanoscopic Strain

Figure 5.11 presents the macroscopic and nanoscopic strains in the irradiated volume of the samples as a function of elapsed time. ε is the macroscopic strain as computed from the strain of the grid of fiducial marks on the samples. $\varepsilon_{n,I(s)}$ is a nanoscopic strain that is computed from the movement of the maximum position of the SAXS peak in the pattern $I(\mathbf{s})$. $\varepsilon_{n,CDF}$ is a nanoscopic strain parameter computed from the movement of the maximum position of the long period peak in the CDF. Choosing this parameter we take the most probable long period for the average long period.

Obviously, ε and $\varepsilon_{n,I(s)}$ exhibit initially the same behavior for the materials TPU 205 and TPU 215. In TPU 235 $\varepsilon_{n,I(s)}$ is always smaller than the macroscopic strain. For high macroscopic strains the nanoscopic strain from the SAXS peak position, $\varepsilon_{n,I(s)}$, remains constant on a plateau. The structural reason for this strange behavior is found in the CDF. As a first test, the nanoscopic strain $\varepsilon_{n,CDF}$ has been computed. The result appears even stranger. $\varepsilon_{n,CDF} \ll \varepsilon_{n,I(s)}$ is valid throughout the whole experiment, but the onset of the plateau is similar. This

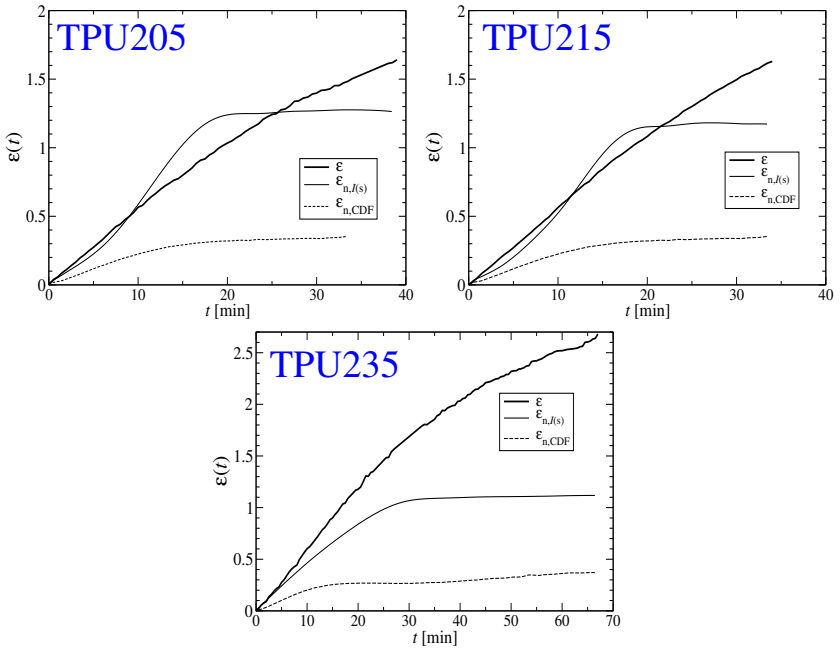

Figure 5.11: Evolution of strains in the tensile test. ε: macroscopic strain, $\varepsilon_{n,I(s))}$: nanoscopic strain from the shift of the SAXS peak maximum, $\varepsilon_{n,CDF}$: nanoscopic strain from the position of the CDF peak maximum

finding appears less surprising, if the peak maximum position is no approximation of the mean (the average long period). This is the case, if the long period distribution is not affinely expanded, but its skewness is growing during the mechanical test.

5.7 Long Period Peaks in the CDF: Analysis of Peak Shape

The simple CDF long period peak (L-peak) analysis presented in the previous section hooks the maximum of the long period distribution (brightest area in Figure 5.12-5.14), tracks its movement and relates it to a nanoscopic strain $\varepsilon_{n,CDF}$. This approach is only reasonable, if the distribution of the long periods is affinely expanded in the straining experiment. Instead, if the skewness of the distribution is increasing, then $\varepsilon_{n,CDF}$ as computed from the L-Peak *maximum* hangs behind the *average* nanoscopic strain.

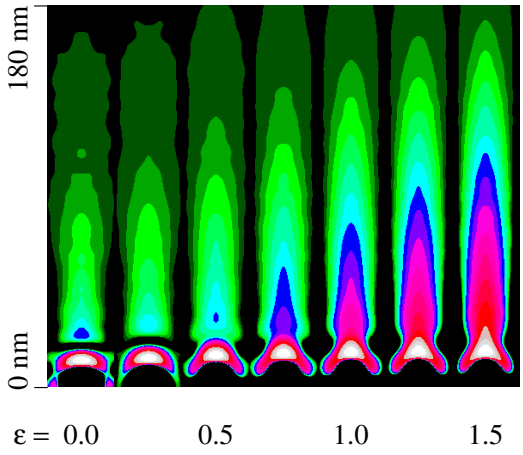

Figure 5.12: TPU 205. Detail of the CDF: Evolution of the long period peak in real space as a function of macroscopic strain ε. Direction of strain (r_3) is vertical. The width of each band in transverse direction (r_{12}) is $\pm$16 nm

5.7.1 Demonstration of L-Peak Shape Variation

In order to discuss the shape evolution of the long period distributions, the regions (example: white border in Figure 5.8) of the corresponding peaks are extracted from the CDFs. These regions are collected as a function of ε and displayed in Figure 5.12 – 5.14 for discussion.

For sample TPU 205 Figure 5.12 presents the regions of the L-peak in the CDFs as a function of strain. Here and with sample TPU 235 (Figure 5.14) the most simple evolution is observed: Upon straining the relative asymmetry of the long period distribution increases considerably: The many thin soft domains are relatively hard, the thick soft domains are considerably softer.

We do not discuss this disproportionating in terms of different Young's moduli, because there might as well be a different reason: an elastic limit due to full extension of taut tie-molecules that is increasing more or less continuously with increasing soft-layer thickness. Taut tie-molecules may simply block further extension of respective sandwiches.

So the thin soft domains undergo a low nanoscopic strain, whereas the thick soft domains are easily elongated during the straining experiment. When the plateau of $\varepsilon_{n,CDF}(t)$ is reached in Figure 5.11, there is no more movement of the maximum position of the L-peak. The many hard soft-domains that contribute to

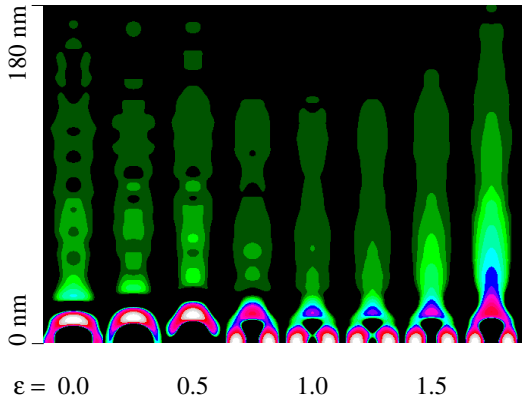

Figure 5.13: TPU 215. Detail of the CDF: Evolution of the long period peak in real space as a function of macroscopic strain ε. Direction of strain (r_3) is vertical. The width of each band in transverse direction (r_{12}) is ± 16 nm

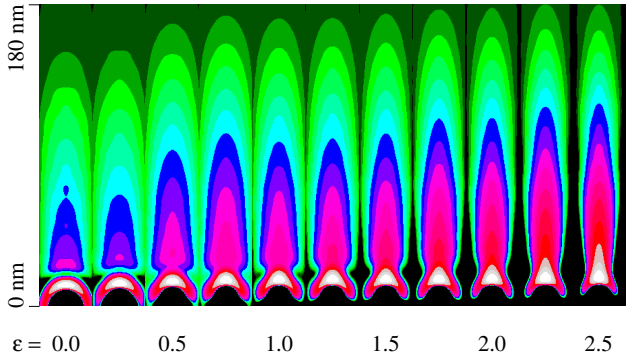

Figure 5.14: TPU 235. Detail of the CDF: Evolution of the long period peak in real space as a function of macroscopic strain ε. Direction of strain (r_3) is vertical. The width of each band in transverse direction (r_{12}) is ± 16 nm

this peak have all reached their elastic limit, whereas the soft domains collected in the tail of the L-peak are still lengthening as a consequence of the continued macroscopic load. Let us consider the widths of the strip-shaped reflections. The widths are a measure of the average hard-domain widths. It is decreasing with increasing macroscopic strain. This indicates disruption of hard domains under stress. This observation supports the chain orientation process by Bonart [101, 102]. With TPU 235 the initial width of the hard-domain distribution is wider than with the materials molded from cooler melts.

Figure 5.13 shows a more complex nanostructure. Here the thickness distri-

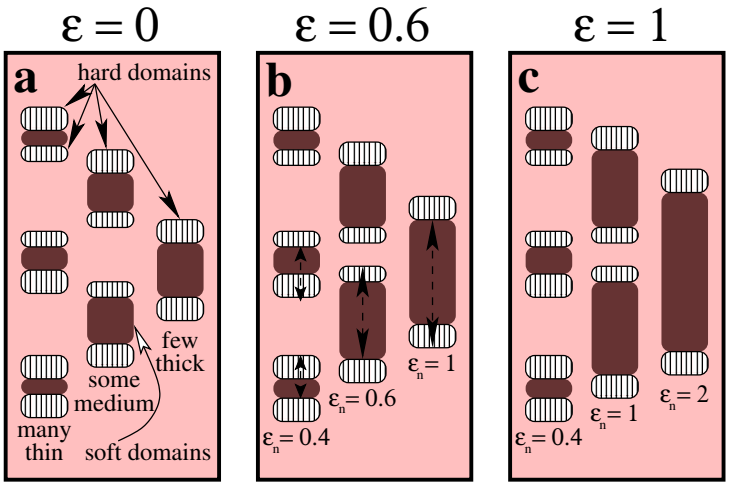

Figure 5.15: Principal straining mechanism of the studied TPU material. **a**: Unstrained state. There are many sandwiches with thin soft layers and few with thick soft domains. The thicker the soft domains are, the lower is their modulus. **b**: Medium strain. For the thin layers there is a stretching limit. Double-head arrows indicate the distances between phase boundaries that are collected in the L-peak of the CDF. **c**: High strain. Only the medium and thick layer sandwiches keep responding

bution of the soft domains is not unimodal, but multimodal with several preferential soft domain thicknesses. Nevertheless, even this sample follows the basic mechanism discussed with the other materials. Thin soft domains are harder than thick ones, and the straining of thick domains is easier than the straining of thin domains.

5.7.2 Principal Deformation Mechanism

These results are summarized in a simple sketch (Figure 5.15) that describes the principal deformation mechanism of the studied TPU materials – still neglecting domain formation, transformation or destruction. The virgin injection-molded material (Figure 5.15a, $\varepsilon = 0$) exhibits a nanostructure of hard and soft domains with poor inter-domain correlation. Thus the SAXS only sees uncorrelated "sandwiches", e.g. two hard domains with a soft domain in between (or two soft domains with a hard domain in between). In the sketch only one type of sandwich is drawn. Thus the main scattering effects in the CDF on the meridian are the domain peak (at very small r_3), and the long period peak (L-peak) that has been discussed

in the previous section. By definition of the CDF, the L-peak collects the number-probabilities of those distances between phase boundaries that are indicated by vertical double-head arrows. Inspection of the L-peaks of the unstrained material has yielded that the long period distributions are highly anisotropic. We see many sandwiches with thin soft domains, but few sandwiches with thick soft domains. Figure 5.15b sketches a situation in the elongated state with changed shape of the sandwiches. We assume that the hard-domain distributions are much more rigid than the soft-domain distributions. Thus from the highly non-affine shape change of the L-peak we infer that change is mainly caused from the straining of soft domains. We observe that the many thin-layer sandwiches are strained ($\varepsilon_{n,CDF}$) much less than the macroscopic strain (ε). On the other hand, the tail of the anisotropic L-peak is extended so far out that the few thick-layer sandwiches have been strained much more than the macroscopic strain. Finally, in Figure 5.15c, all the thin-layer sandwiches have reached their elastic limit and do not extend any more. Further nanoscopic strain is only taking place in medium-layer and thick-layer sandwiches.

5.7.3 Domain Formation, Transformation and Destruction

As the last step in nanostructure evolution analysis we are searching for hints concerning the formation, transformation and destruction of domains. Initial strain may arrange hard segments in such a way that they form new hard domains. Further straining may break intermediate hard domains, resulting either in a transformation of thin-layer sandwiches into thick-layer sandwiches or in a complete loss that decreases the number of sandwiches.

In order to answer this question we study meridional slices $\lceil z(\mathbf{r})\rceil_1(r_3) = z(r_{12}=0,r_3)$ of the CDF. It appears worth to be reminded that such slices in real space, $\mathbf{r}$, describe the correlation among the phase boundaries between hard and soft domains in the direction of strain. Assuming that there is no relevant correlation beyond the intra-sandwich ones, the curve $-z(r_{12}=0,r_3)$ cut from the CDF on its meridian must be positive for $r_3 > r_{mt}$. r_{mt} is the maximum thickness of a single domain. Then – apart from oscillations that demonstrate the limit of the assumption – $-z(0,r_3)$ is the distribution of long periods in the material. The strip-plots (cf. Figure 5.12 – Figure 5.14) appear to suggest that an analysis might

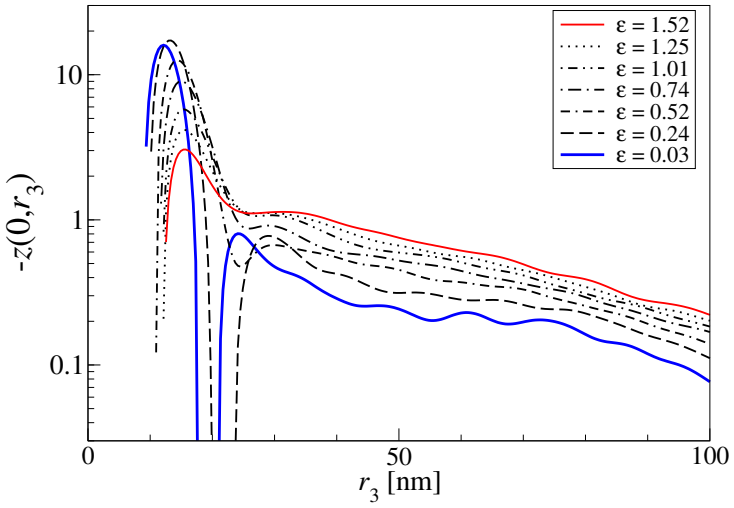

Figure 5.16: TPU 205. Evolution of CDF slices $-z(r_3)$ along the meridian as a function of macroscopic strain ε

be possible at least to a first approximation. Because of the fact that the scattering patterns have been normalized for constant thickness, the curves can be compared relative to each other.

Figure 5.16-5.18 show the CDF slices in semi-logarithmic plots. The curves are selected in steps of $\Delta\varepsilon \approx 0.25$. Intensity collapses indicate correlations among neighbors that are violations of the simplifying assumption. Above a level of strain that depends on the sample preparation these collapses become rather small. The thin-layer sandwiches are indicated by the sharp maximum at the beginning of the L-peak.

For all materials the nanostructure shows a broad variety of scattering entities ranging from thin-layer sandwiches to thick-layer sandwiches. After the start of the experiment the thin-layer-sandwich maximum is increasing. Thus the number of thin-layer sandwiches is increasing for TPU 205 and TPU 215 up to $\varepsilon \approx 0.25$, and for TPU 235 up to $\varepsilon \approx 0.5$. An increase of contrast between the hard phase and the soft phase could cause the same effect, but it appears unlikely to assume that the soft-domain density decreases as a result of applied strain. The more probable formation of thin-layer sandwiches may be the result of disruption of clusters of hard-domains that contain soft segments (cf. Figure 5.19, middle row).

After this initial strain-induced formation of thin-layer sandwiches the number

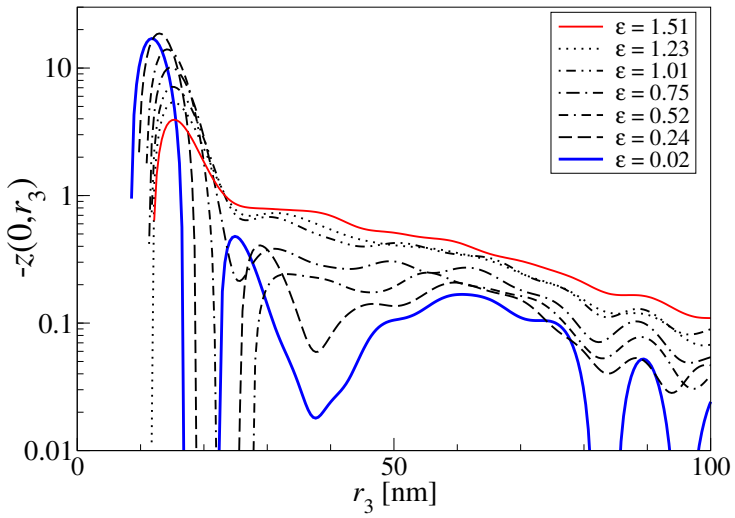

Figure 5.17: TPU 215. Evolution of CDF slices $-z(r_3)$ along the meridian as a function of macroscopic strain ε

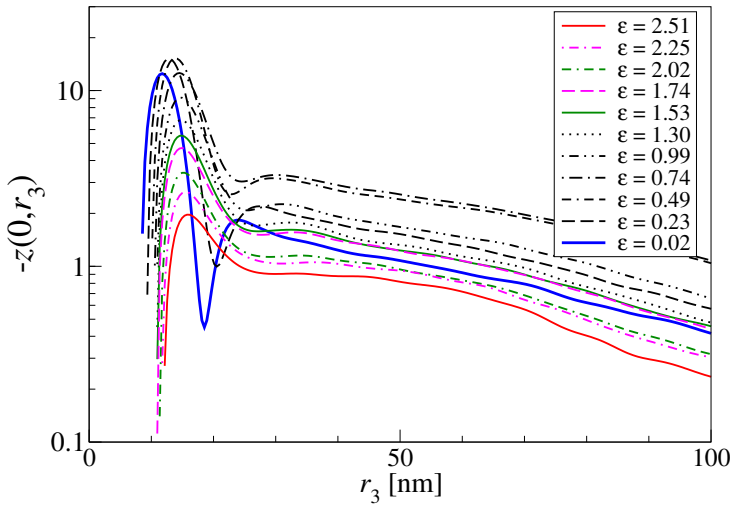

Figure 5.18: TPU 235. Evolution of CDF slices $-z(r_3)$ along the meridian as a function of macroscopic strain ε

of thin-layer sandwiches is decreasing. For the samples TPU 205 and TPU 215 at the same time the number of sandwiches in the tail of the L-distribution is increasing. Because it is unlikely that at the same time one of the soft phases becomes more dense and the other becomes less dense, this observation shows that some of the thin-layer sandwiches are disrupted and, after that, the remnant hard domain may become member of a thick-layer sandwich. This transformation process is active up to a macroscopic strain $\varepsilon \approx 1.6$. Then the two materials have become so hard that they slip from the clamps of the tensile tester.

For sample TPU 235 the transformation process is only dominant until $\varepsilon \approx 0.75$ (highest curve for $r_3 > 30\,\text{nm}$). After that even the number of thick-layer sandwiches starts to decrease, most probably because of destruction of their hard domains. As a result, the material appears more soft than TPU 205 and TPU 215. It can be strained until $\varepsilon = 3.1$ before the stress increases beyond 100 MPa and the sample slips from the clamps, as well. Thus we observe a direct correlation between macroscopic properties and the stability of the hard domains controlled by choice of the processing temperature. The detected nanostructure evolution mechanisms are sketched in Figure 5.19. Samples processed from a lower temperature melt (205 °C, 215 °C) exhibit an evolution with two transformation mechanisms among the scattering entities (in the sketch indicated by arrows): At strains $\varepsilon < 0.3$ clusters are transformed into thin-layer sandwiches. Above $\varepsilon > 0.3$ the dominant transformation process is destruction of hard domains from thin-layer sandwiches that leads to an increase of thick-layer sandwiches. The hard domains are strong. The material slips from the clamps at $\varepsilon \approx 1.6$.

The sample processed at 235 °C exhibits an evolution with 3 transformation mechanisms. Only the third one is new: Many hard domains are weak and are destructed during straining. The destruction becomes dominant at $\varepsilon = 0.75$. An explanation for the different hard-domain strengths becomes obvious, because 235 °C is in the center of the second melting endotherm (cf. Figure 5.3) that has been related to homogeneous mixing [95] of soft and hard segments. The detected strength of hard domains after low-temperature processing may be caused from the fact that phase separation in the mold advances to a higher level when it is applied to a presorted melt. Thus it may be favorable to partially preserve the phase separation between hard and soft segments in the manufacturing process, if the aim is production of TPU materials with strong hard domains.

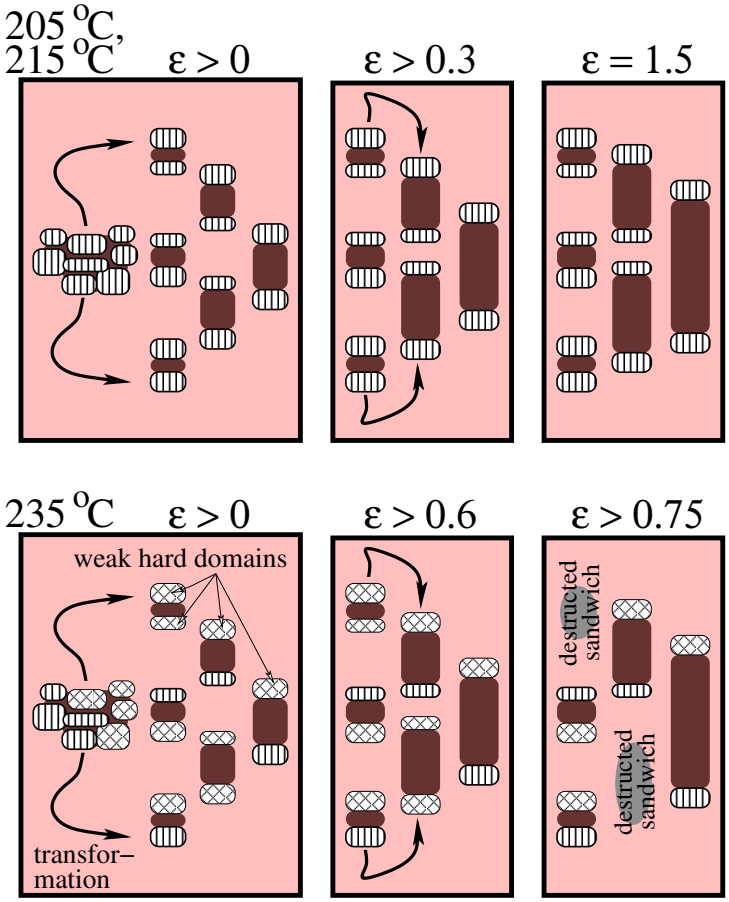

Figure 5.19: Nanostructure evolution mechanisms of the TPU injection-molded samples as a function of processing temperature and strain

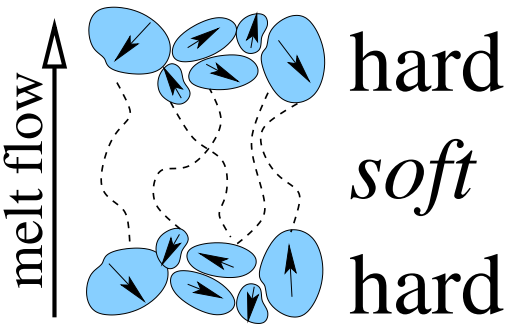

Figure 5.20: Proposed inner sandwich structure: Hard domains from almost randomly oriented very small grains (that may be crystalline) are preferentially oriented perpendicular to the flow direction of the injected melt. Small arrows indicate the chain orientations inside the grains

Figure 5.20 shows a model for the initial inner structure of the hard domains. According to this model the hard domains are clusters of very small grains that may be crystalline. SAXS shows that the hard domains as a whole are oriented more or less perpendicular to the melt-flow direction during injection molding. SAXS shows that during the straining process the hard domains break apart.

In summary, the materials from the lower injection temperatures contain bigger crystallites inside the hard domain lamellae (higher T_m). These lamellae initiate spherulitic growth. The small grains that are formed during injection from the high temperature are neither strong nor able to initiate spherulitic growth. These results suggest that in order to obtain strong TPU materials, the manufacturing process must be done below the phase-mixing temperature.

Chapter VI

Polypropylene/Montmorillonite Nanocomposites: Continuous Stretching and Load-Cycling

In the last two decades there have been a lot of efforts to improve mechanical properties of polypropylene [103] via compounding it with layered silicates (clay) [104–109]. For instance, enhancements of storage modulus [110–112], Young's modulus [113, 114], impact strength [115, 116], and tensile strength [116, 117] have been reported. Layered silicates can be mixed with polypropylene in the melt state using conventional polymer processing machinery [105, 106, 108, 118]. Nevertheless, incompatibility of layered silicates with hydrophobic polypropylene chains provokes problems with dispersing them inside the matrix [119, 120]. The problem of dispersion has partly been solved by chemical treatment [106, 108, 109, 116, 118, 121–123] of clay surfaces, addition and tailoring of compatibilizers [106, 108, 118, 120, 124, 125] and modification of mixing methods [106, 108, 126–128]. In spite of relatively good dispersion (intercalation and exfoliation) [116, 118, 129–131] the obtained improvement in some mechanical properties of PP/clay (e.g. tensile strength) is still modest compared to other thermoplastic nanocomposites such as nylon 6/clay [108]. Hence dispersion of clay particles appears not to be the only determining parameter. Several papers [113, 132–140] report alteration of semi-crystalline structure of polypropylene in the presence of layered silicates. Two important effects have been observed; firstly polypropylene chains crystallize at temperatures higher than the crystallization temperature T_c of the neat polymer [112, 117, 132, 134–136], secondly clay exfoliation enhances the shear-induced nucleation and the overall crystallization rate [137, 140]. Microstructure alteration of the matrix (PP) influences in turn the properties of the nanocomposite [108]. Such effects may be investigated by small-angle X-ray scattering (SAXS). In particular results from SAXS-monitoring of structure evolution under load may advance the understanding of the relation

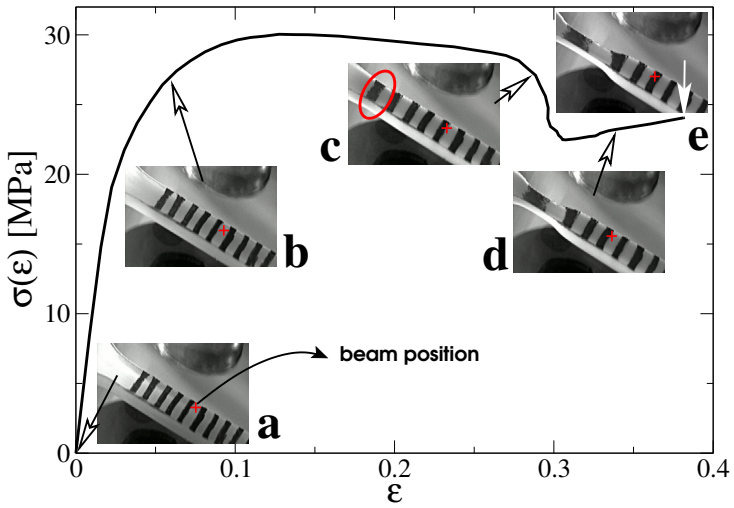

Figure 6.1: Stress relaxation and spot translation caused by necking. True stress $\sigma(\varepsilon)$ as function of local strain ε. **a:** Start of test. The X-ray beam spot is indicated by a cross. **b:** Homogeneous stretching. Spot does not move. **c:** Necking has started (see ellipse). Material shows stress relaxation. **d:** Spot moving towards neck. **e:** End of experiment

between the composite's morphology and its practicality in a load-bearing application.

6.1 Mechanical Data

The self-made[75] tensile tester performs symmetric drawing. Thus the same spot of the sample is monitored by the X-ray, as long as the sample is homogeneously extended. If the tested material starts to neck, a peculiar problem is encountered that limits the interval in which data evaluation appears reasonable. This is demonstrated in Figure 6.1. In the inset images the irradiated spot is indicated by a cross. As the material begins to neck (Figure 6.1, inset **c**), stress relaxation is observed and the irradiated spot starts to move along the sample towards its neck. Because the X-ray is no longer monitoring the same location of the material, the corresponding data are not discussed.

Figure 6.2 shows the mechanical data of the tensile tests in the synchrotron beam. The true stress σ is plotted as a function of the local strain ε measured at the point of irradiation by the synchrotron beam. The spot-translation tail of the curves has been discarded. Obviously, the uncompatibilized materials (pure

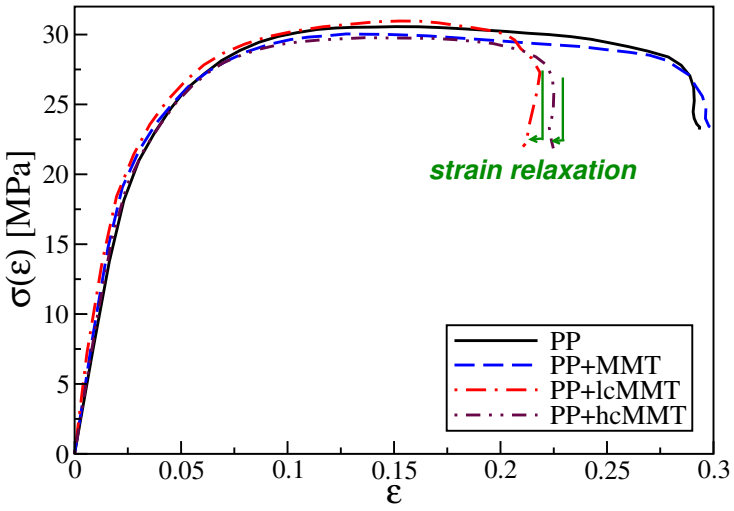

Figure 6.2: Tensile testing of PP/MMT materials in the synchrotron beam. True stress $\sigma(\varepsilon)$ as a function of the local strain ε at the position of irradiation. Compatibilized nanocomposites exhibit even relaxation of local strain ε

PP and PP+MMT) start necking at a higher elongation ($\varepsilon \approx 0.29$) than the composites that contain compatibilized MMT. Moreover, these composites even show relaxation of the local strain while the neck is developing.

6.2 Discussion of Measured SAXS Patterns

Figure 6.3 presents central sections of selected SAXS patterns $I(s_{12}, s_3)$ from the plain straining experiments as a function of the local strain ε. The measured images are larger and range to $s = \pm 0.25\,\mathrm{nm}^{-1}$. The logarithmic intensity scale is identical for all images.

Unstrained materials. Before the start of the tests ($\varepsilon = 0$) all the injection molded materials exhibit discrete SAXS with high uniaxial orientation. Two-point patterns are observed. The peak maxima are on the vertical axis (s_3, meridian, direction of the melt-flow in the bar, straining direction). From top to bottom both the peak intensity and the lateral peak width are strongly increasing. The narrow reflections of the pure PP (top) and of the blend PP+MMT (below) are indicative for layer stacks made from crystalline lamellae in the PP that extend in the direction perpendicular to the direction of melt-flow. Nevertheless, the blend al-

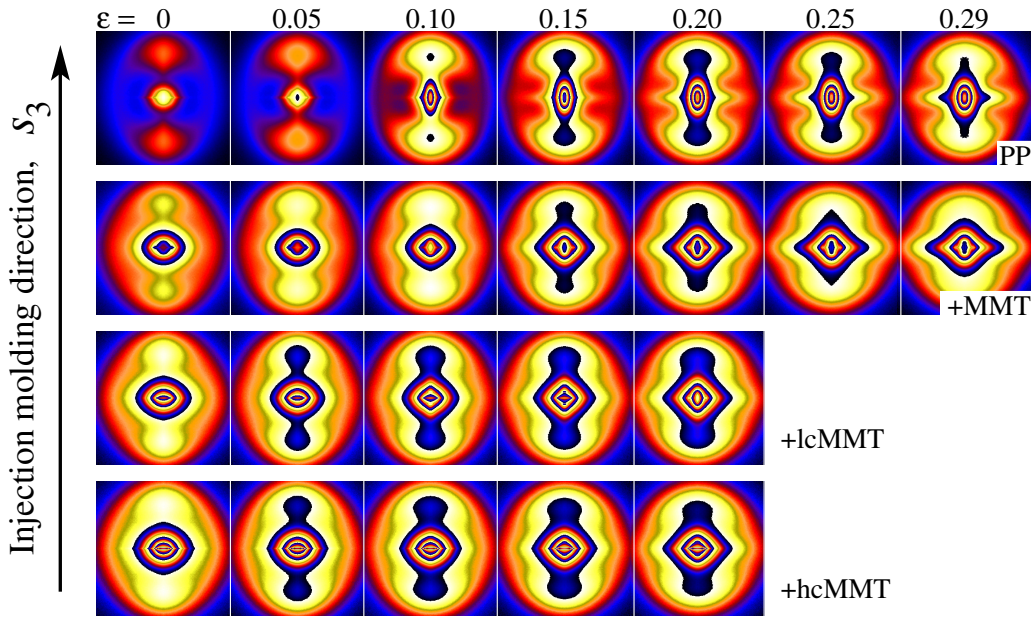

Figure 6.3: SAXS intensities $I(s_{12}, s_3)$ of PP, a blend (+MMT) and two composites (+lcMMT, +hcMMT) as a function of the local strain ε. Straining direction s_3 is vertical. The images are on the same logarithmic scale. They show the central region $-0.15\,\mathrm{nm}^{-1} \leq s_{12}, s_3 \leq 0.15\,\mathrm{nm}^{-1}$ of the measured patterns in a repetitive pseudo-color presentation

ready contains an additional background. It is a broad peak underneath the narrow reflection, which indicates an additional microfibrillar component. In this component the shape of the crystalline domains is no longer an extended lamella, but only a granule of lower lateral extension.

The blend and the composites exhibit strong central scattering of big scattering entities. These entities may either be crazes formed between the nanoparticles and the PP matrix, or bigger particles of MMT that have not been exfoliated. Typical for craze scattering is diffuse central scattering showing an envelope of cross shape or of diamond shape [141–146].

Diffuse central scattering as a function of strain. At $\varepsilon = 0$ none of the samples exhibits diamond-shaped central scattering. From left to right in Figure 6.3 the local strain is increasing in steps of $\Delta\varepsilon = 0.05$. All samples that contain MMT develop diamond-shaped central scattering during the test. This observation can be explained by voids in the MMT materials at least for $\varepsilon > 0.15$. During the test even pure PP develops central scattering that is increasing up to $\varepsilon \approx 0.2$. Its envelope shows a different shape. It is an ellipse with its long axis in the direction of strain. This means that the corresponding scattering entities are oriented perpendicular to the straining direction. They could be explained by amorphous layers that are converted into crazes. In parallel, a rather well-defined equatorial streak is developing. Such streaks are typical for needle-shaped voids extended in the straining direction [147]. In summary, the SAXS of all samples indicates void formation during tensile testing.

Pure polypropylene. The top row of Figure 6.3 displays selected patterns taken during the tensile test of the pure PP material. The scale is identical for all pseudocolor images in the figure. With increasing local strain also the maximum peak intensity is increasing and after the yield stress is reached (cf. Figure 6.2), i.e. $\varepsilon > 0.1$, the peak itself is broadening in lateral direction. The peak broadening after reaching the yield-stress level indicates a decrease of crystallite extension in the direction perpendicular to the "fiber" axis. This decrease can be explained [148] by disruption of crystalline lamellae. Such a morphological transition from a lamellar to a microfibrillar stack is generally observed whenever semi-crystalline polymers are subjected to uniaxial strain [99].

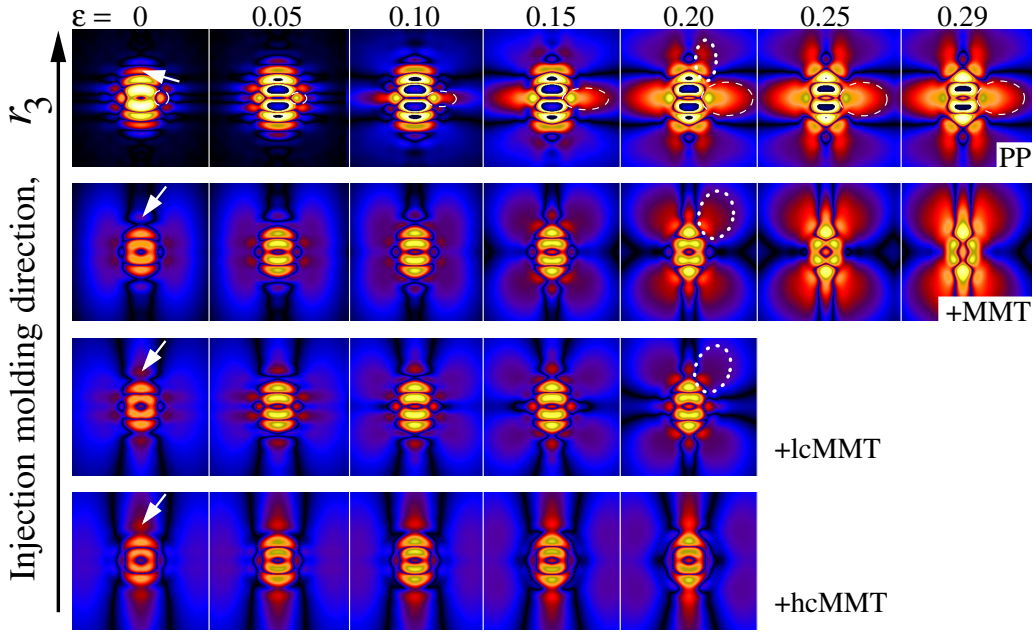

Figure 6.4: Absolute values $|z(r_{12}, r_3)|$ of chord distribution functions (CDF) of PP, a blend (+MMT) and two composites (+lcMMT, +hcMMT) as a function of the local strain ε. Straining direction r_3 is vertical. The images are on the same logarithmic scale. In a repetitive pseudo-color representation the images show the region $-60\,\text{nm} \leq r_{12}, r_3 \leq 60\,\text{nm}$ of the patterns computed from SAXS data by a special Fourier transform

PP/MMT blend and nanocomposites. The scattering patterns of the blend and the two nanocomposites are presented in rows 2–4 of Figure 6.3. All materials show the mentioned transition into a microfibrillar stack morphology, but their initial structure is different from the initial structure of the pure PP. The scattering patterns appear rather blurred and a direct qualitative interpretation can only describe very general features. Thus the scattering entities of the samples that contain MMT must be smaller, less homogeneous, and their arrangement less perfect than with the pure PP. A quantitative analysis will be based on the data after their transformation into the CDF that displays the morphological features more clearly.

6.3 Discussion of the CDF Patterns

Figure 6.4 shows the absolute values $|z(r_{12}, r_3)|$ of the CDFs for the 4 studied

materials. The pseudo-color scale is identical for all images.

Nanostructure of the unstrained samples. The left column displays the CDFs of the samples at $\varepsilon = 0$. Most prominent are the layer-like peaks on the meridian of the CDFs. They describe the stacked crystalline and amorphous layers of the polypropylene matrix and their correlation in straining direction. Their lateral extension is a measure of the average lateral extension of the layers. These reflections are analyzed quantitatively in Section 6.6. It is worth reminding that the meridional SAXS peaks reflected in the CDF only probe the part of the matrix volume that is filled by semi-crystalline stacks with a minimum arrangement among their constituent domains (ordered stacks). Random placement of irregular domains does not generate discrete SAXS peaks.

The CDF in the top left corner shows the pure PP. Compared to the blend and the composites below its peaks are wider in horizontal direction. Thus the lamellae are wider than those of the samples that contain MMT. Moreover, several distinct reflections are piled up. This shows that the thickness variation of the layers is low, and at least 3 crystalline lamellae are correlated in each stack. In the samples containing MMT the correlation along the stack is even lower. There are only 2 crystalline layers in each stack (a "sandwich"). Arrows point at the shape distributions $h_{cac}(r_{12}, r_3)$ of such sandwiches. For the pure PP $h_{cac}(r_{12}, r_3)$ is narrow in r_3-direction. Thus the heights of all sandwiches are almost the same. In the lateral r_{12}-direction the peak is extended. Thus the sandwich is made from two crystalline lamellae that are well-aligned on top of each other.

In the materials that contain MMT the lateral width of $h_{cac}(r_{12}, r_3)$ is narrower than the lateral width of the inner peaks. Thus there is some lateral disorder in the piling. Let us discuss the shape of the sandwich peak in Figure 6.4 from top to bottom. In r_3-direction the height distribution of the sandwiches becomes broader and more and more asymmetric. For the material with the high amount of compatibilizer (PP+hcMMT) the tail of the sandwich distribution even outreaches the limit of the image at $r_3 = 60$ nm. From top to bottom a decrease of domain size, domain uniformity, and domain arrangement is observed. This fact is as well reflected in the decrease of the sharp off-meridional peaks. They characterize correlations among crystallites whose connecting line is not in straining direction.

All the CDFs of the MMT samples show an off-meridional, vertically ex-

tended intensity region. This intensity characterizes the distance distribution between the left and the right edge of microfibrils that house the crystalline domains. For pure PP this peculiar arrangement of crystalline domains is not observed.

6.4 Analysis of the Block-Structure

In Figure 6.4 proceeding from left to right, the evolution of the semi-crystalline polypropylene structure as a function of ε is presented. For the pure PP (top row) the structure evolution is very much different from that of the other materials. Most peculiar is the development of a very strong equatorial long period distribution $h_{ba}(r_{12}, r_3)$. In Figure 6.4 it is marked by a dashed-line ellipse. Already at $\varepsilon = 0$ a pointed precursor peak is found on the equator. As the yield-stress level is reached at $\varepsilon = 0.1$, the peak starts to grow outward on the equator (i.e. in r_{12}-direction) by combining with an outer satellite. At $\varepsilon = 0.2$ the peak widens in r_3-direction, and from $\varepsilon \approx 0.25$ the shape of the peak does not change any more. h_{ba} describes a lateral correlation between adjacent crystallites that are no extended lamellae. Taking into account the satellite peaks that are visible at low strain, ensembles of 3 crystalline grains arranged along the r_{12}-direction are present. The corresponding scattering entity in the equatorial plane is readily identified as Strobl's block structure [83, 84]. In the patterns of samples containing MMT the block structure is much less distinct. Nevertheless, when the yield point is approached at $\varepsilon = 0.1$ all materials exhibit a block structure. At this strain the 3 top patterns even show many sharp block-correlation peaks surrounding the center of the pattern. This observation indicates, that close to the yield point the blocks even arrange[149] in the 3rd dimension. A three-dimensional macrolattice[150] of only short-range correlation has been formed.

Figure 6.5 presents results of a quantitative analysis of Strobl's block structure as a function of the local strain ε. The long period L_b is shown. L_b is the most frequent distance between adjacent blocks in the equatorial r_{12}-plane as determined from the position of the maximum of $h_{ba}(r_{12}, r_3)$ in the CDF. For all samples L_b decreases slightly with increasing ε until yielding sets in. For $\varepsilon > 0.1$ a slight increase is observed. Thus the block structure itself behaves identical in all samples. The only difference is that addition of MMT diminishes its fraction severely.

Only for the pure PP with its strong block structure a more involved peak

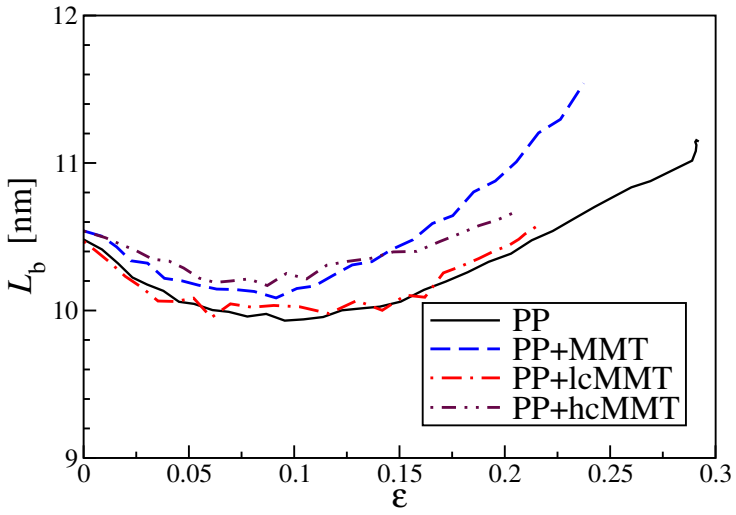

Figure 6.5: The evolution of the most-frequent long period L_b of Strobl's block structure during tensile testing of PP and PP/MMT materials. L_b is determined from the maximum position of the equatorial long period peak in the CDFs (cf. Figure 6.4)

shape analysis is possible. As described previously (cf. Section 4.2.2.1), a bivariate polynomial is fitted to the cap of the peak in order to determine its position and the standard deviations that describe the peak widths in equatorial and meridional direction, respectively. Figure 6.6 presents the result. L_b has already been discussed. ΔL_b is the breadth of $h_{ba}(r_{12}, r_3)$ in equatorial r_{12}-direction. H_b is the height of $h_{ba}(r_{12}, r_3)$ in meridional r_3-direction. These two width parameters have been defined by 3 times the respective standard deviations. As has already been seen by inspection of the patterns, the breadth ΔL_b is increasing during the tensile test. The quantitative analysis shows that this increase is continuously slowed down with increasing ε. H_b reflects the average height of the blocks. For low strain H_b is constant at 5.5 nm. Just before the yield level is reached at $\varepsilon \approx 0.08$, H_b starts to increase linearly. The mechanism behind this growth of block height may be chain extension caused by the increased local stress around the blocks. Such chain extension could make the blocks grow tending towards a formation of extended chain crystals.

Some peaks in Figure 6.4 are difficult to analyze. They are encircled by dotted lines. These peaks result from sandwich domain size distributions $h_{cac}(r_{12}, r_3)$ that overlap severely with the strong and narrow meridional distributions. There-

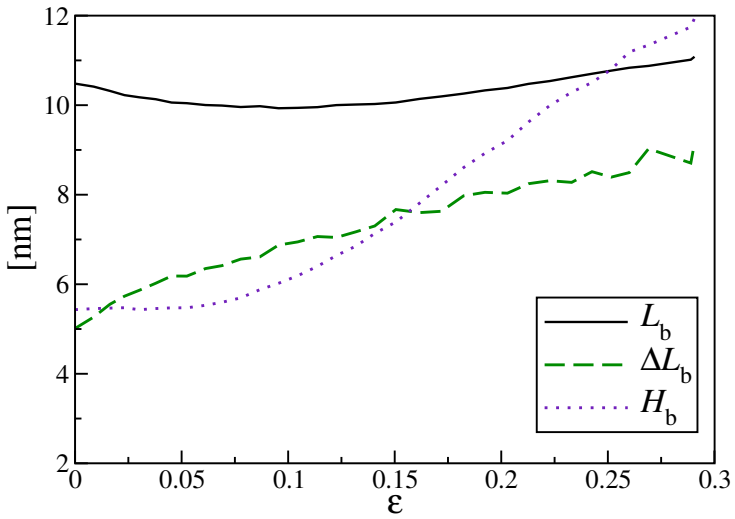

Figure 6.6: Nanostructure evolution of Strobl's block structure during tensile testing of the pure PP material from peak-shape analysis of the equatorial long period peak $h_{ba}(r_{12}, r_3)$ in the CDF (encircled in Figure 6.4). L_b is the most frequent distance between adjacent blocks, ΔL_b is the breadth of $h_{ba}(r_{12}, r_3)$, and H_b is the height of $h_{ba}(r_{12}, r_3)$ in straining direction

fore an analysis would require to separate these peaks from the meridional distributions by fitting the complete CDF patterns with a three-dimensional model of the semicrystalline PP nanostructure. The CDFs exhibit that such a model would have to be rather complex.

6.5 Analysis of the Scattering Power

Figure 6.7 shows the evolution of the scattering power Q of the semicrystalline PP as a function of strain. The curves are normalized to constant irradiated volume and constant flux. Thus

$$Q\,c = (\rho_c - \rho_a)^2\, v\,(1-v) + X \tag{6.1}$$

is valid with c being a calibration constant. The contrast factor is specified by the electron densities ρ_c and ρ_a of the crystalline and the amorphous domains, respectively. v is the volume crystallinity of the PP. Obviously, $v\,(1-v) \approx 0.24$ remains almost constant for $0.3 < v < 0.7$. X is an unknown factor that describes both the scattering effects of MMT particles and of voids or crazes on Q. At $\varepsilon = 0$ the

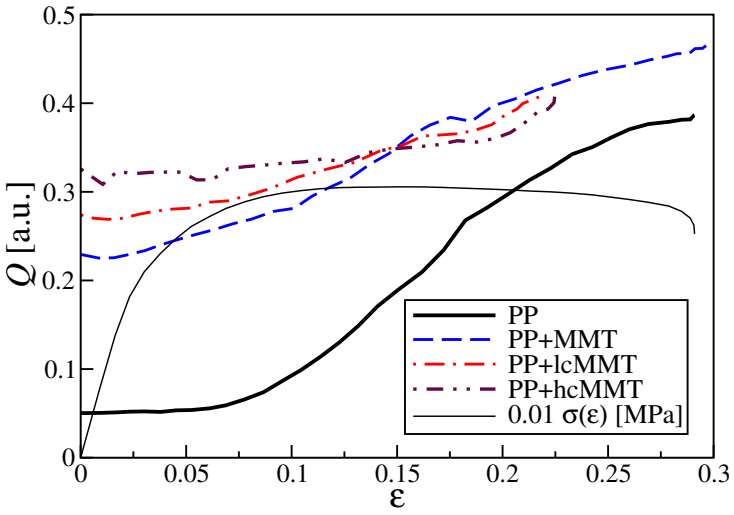

Figure 6.7: Evolution of the scattering power Q during tensile testing of PP nanocomposites as a function of the local macroscopic strain ε in the irradiated volume. Additionally the stress-strain curve $\sigma(\varepsilon)$ of the pure PP material is shown

scattering power of PP is considerably smaller than that of the samples containing MMT. The reason is either the scattering tail of big MMT particles or the scattering of voids. Compatibilization of the MMT increases the scattering power even more. This result may be caused by MMT exfoliation in the nanocomposites.

For pure PP $Q(\varepsilon)$ remains constant until the onset of yielding. The constant value for low strain is readily explained by constant contrast. After yielding sets in, the sample starts to become white. Thus the strong increase of $Q(\varepsilon)$ for $\varepsilon > 0.1$ can be related to void formation. It is well-known that voids mainly affect the scattering at low s. Because Q is only a number, the isotropic scattering $s^2 I(s)$ with $Q = 4\pi \int s^2 I(s)\, ds$ is prepared (cf. Section 4.2.4) for angle-dependent inspection (Figure 6.8). For the sample PP Figure 6.8 shows a steep increase of scattering at very low angles ($s < 0.05$ nm^{-1}). On the other hand, the change of the long period peak ($s \approx 0.09$ nm^{-1}) is only moderate. Thus it can be concluded that the steep increase of Q with sample PP indicates considerable formation of voids as the material is strained beyond the yield.

The blend PP+MMT exhibits high scattering at low s even in the unstrained state. Further increase of low-s-scattering is moderate. This means that, in contrast to pure PP, straining of the blend does not induce an increase of voids that

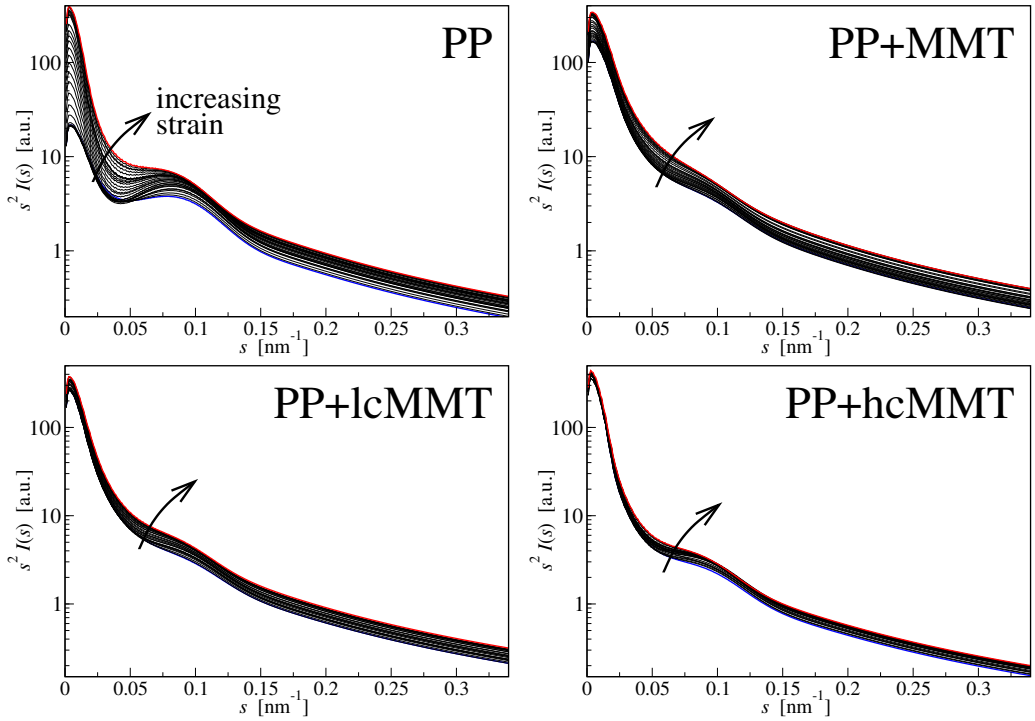

Figure 6.8: Evolution of the isotropic integrands $s^2 I_{id}(s)$ for the computation of Q during tensile testing of PP nanocomposites as a function of the local macroscopic strain ε on a logarithmic intensity scale

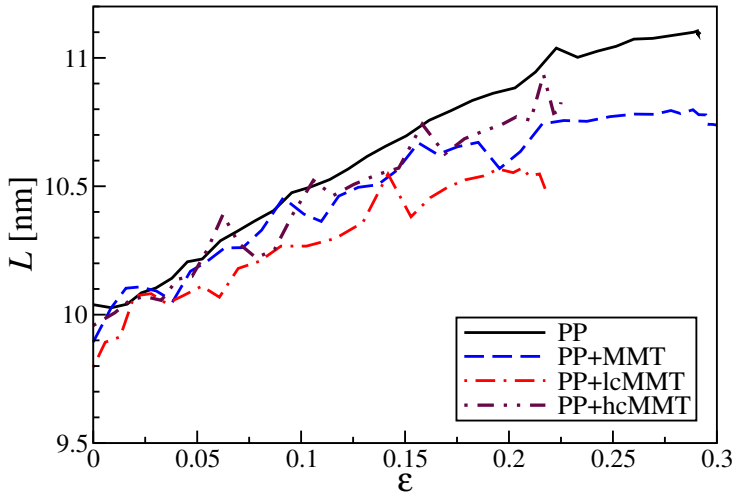

Figure 6.9: Nanostructure evolution during tensile testing of PP nanocomposites determined from the CDF long period peak. Most-frequently long period $L(\varepsilon)$

are small enough to be detected by SAXS.

For the nanocomposites PP+lcMMT and PP+hcMMT Figure 6.8 exhibits a similar response to strain, but the variation of the integrand with strain becomes even smaller. Thus the effect of increasing compatibilization is an increased stability of the nanostructure of the polypropylene that has been formed during injection molding. Admittedly, this finding may simply mean that an already distorted structure cannot be destructed further. Another explanation would be based on a dynamic equilibrium that would not change the SAXS if the voids growing out of the SAXS detection-window would be dynamically replaced by new small voids while all voids are continuously growing. In Figure 6.7 the moderate increase of the total $Q(\varepsilon)$ is depicted. The increase is fastest for the uncompatibilized blend and slowest for the composite that contains the high amount of compatibilizer. Whitening during straining has not been detected with the samples containing MMT, but detection is difficult anyway, because the samples look brownish from the MMT.

6.6 Quantitative Analysis of Meridional Peaks

Figure 6.9 presents the evolution of the long period $L(\varepsilon)$. This is the most frequent distance between two crystalline domains measured in straining direction.

At $\varepsilon = 0$ the long periods of the 4 samples are identical. The increase of $L(\varepsilon)$ is much slower than expected from the macroscopic strain. At 30% strain ($\varepsilon = 0.3$) L has only grown by 10%. The data is more scattered for the samples containing MMT. The shape evolution of the $L-$peak of these samples (Figure 6.4) shows that the asymmetric long period distribution is non-affinely strained. Thus the most probable L is no measure of the *average* nanoscopic strain of the semicrystalline morphology (i.e. of the long period distribution $h_{ca}(r_{12}, r_3)$ that has its maximum at $(r_{12}, r_3) = (0, L)$), but it only reflects the deformation of the well-correlated stacks which are tracked by the maximum of $h_{ca}(r_{12}, r_3)$. This is similar to what was observed during straining TPU materials (cf. Chapter 5). However, the $L-$peak of pure polypropylene moves up without becoming skewed. This indicates that the well-correlated semi-crystalline structure of PP deforms *on average* to a lower extent compared to the macroscopic strain. This phenomena has been observed in other semi-crystalline materials as well (for example see [11, 151–153] or Chapter 7). In summary the strong well-correlated stacks deform less than the macroscopic strain.

The width ΔL of $h_{ca}(r_{12}, r_3)$ in r_3-direction describes the heterogeneity of the stacking of crystalline and amorphous domains. Data are presented in Figure 6.10. Addition of MMT increases the heterogeneity of h_{ca} considerably. Thus the nanodomain stacking of PP is distorted by the MMT. Compatibilization leads to a relative reduction, indicating attenuation of the distorting effect of MMT on the semi-crystalline structure.

With increasing strain the pure PP exhibits a moderate monotonous broadening. The MMT samples start with a slight homogenization of the stacks up to $\varepsilon \approx 0.07$ that is followed by a distinct loss of uniformity when the materials are above the yield. At high strain, compatibilization (PP+lcMMT, PP+hcMMT) even further attenuates the distortion introduced by MMT. The asymmetry of $h_{ca}(r_{12} = 0, r_3)$ is not considered and cannot be quantified from a peak fit that is based on a 2nd-order polynomial only.

The lateral extension $e_{12}(\varepsilon) = 3\,\sigma_{12}(h_{ca})$ (in r_{12}-direction) of $h_{ca}(r_{12}, r_3)$ measures the size of the crystallites in the transverse direction. Figure 6.11 presents the results. $e_{12}(\varepsilon = 0)$ is highest for the pure PP. Addition of MMT leads to a decrease of $e_{12}(0)$ by 2 nm. The compatibilizer has no effect on the initial lateral extension of the crystalline domains, but on its decrease in the addressed conver-

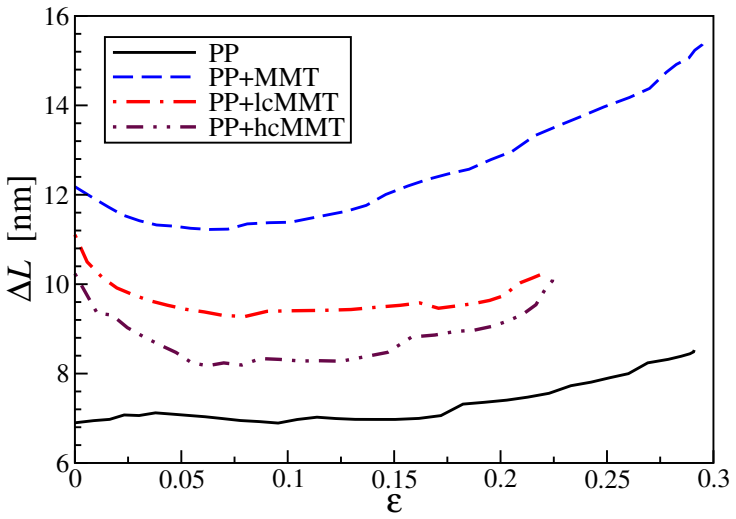

Figure 6.10: Nanostructure evolution during tensile testing of PP nanocomposites determined from the CDF long period peak. Width $\Delta L(\varepsilon)$ in straining direction r_3 of the long period distribution $h_{ca}(r_{12}, r_3)$

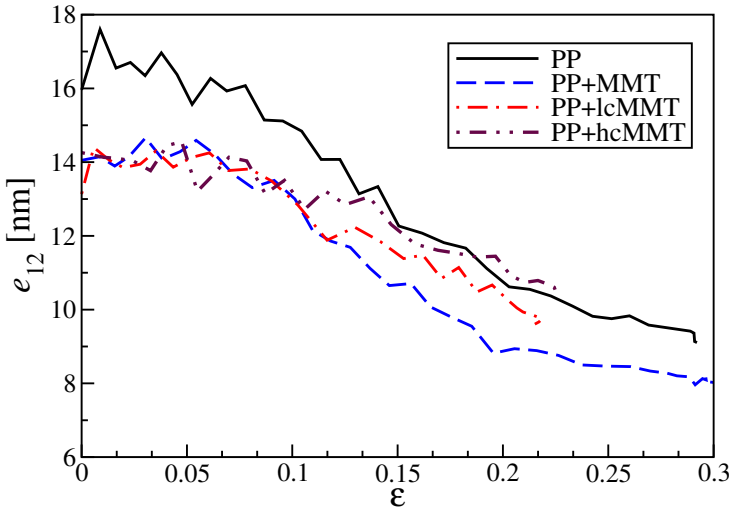

Figure 6.11: Nanostructure evolution during tensile testing of PP nanocomposites determined from the CDF long period peak. Average lateral extension $e_{12}(\varepsilon)$ of the crystalline PP domains

sion from layer stacks to microfibrillar [98–100] stacks. This decrease is generally observed [149, 154–159] during the straining of semi-crystalline polymer materials. Compatibilization diminishes the degradation of the crystallite extension $e_{12}(\varepsilon)$ for $\varepsilon > 0.1$, i.e. above the yield point.

6.7 Nucleation and Compatibilization in the PP/MMT Nanocomposites

Nucleation. The depicted effects of clay on the semi-crystalline morphology (broadening of the crystallite thickness distribution, smaller crystallite extension) may be explained by a strong nucleating effect of the MMT on polypropylene crystallization. Consequently, the nuclei density must have been increased, and during processing many crystallites grow simultaneously, mutually inhibiting their growth. Finally, the altered morphology is described by a less ordered arrangement of undersized, weak crystalline domains. The crystallinity is not increased. This means that addition of MMT to the commercial PP reduces the reinforcing effect of the crystalline polypropylene phase. In summary, part of the intrinsic reinforcement of MMT is not added to the strength of PP. Instead, it only replaces lost self-reinforcement of the polypropylene. As observed with the studied materials, the desired macroscopic reinforcement is not achieved. In Section 6.8 we assess loss of self-reinforcement and gain of foreign reinforcement.

Nevertheless, although the mechanical properties of the 4 materials are very similar, monitoring of the straining experiments by SAXS has shown that the semicrystalline nanostructure and its evolution vary considerably. The relative variations from material to material indicate that the dominant troublesome effect of blending MMT and the studied metallocene polypropylene grade is not the interfacial incompatibility between filler and matrix, but the alteration of the adjusted nanostructure of the matrix grade by the filler.

The addressed strong nucleating effect of MMT has been reported in several papers [113, 132, 134–136, 160–162]. According to Deshmane et al. [163] the nucleating effect of MMT on polypropylene is high, whereas polyethylene remains almost unaffected. The addition of 4% MMT to polypropylene reduces the spherulite diameter from 210 µm to 14 µm, whereas the spherulite size of polyethylene remains unchanged. The different nucleating effect of MMT on polypropylene and polyethylene could explain, why Drozdov et al. [164] have found a strong reinforc-

ing effect of MMT on polyethylene.

On the other hand, Deshmane et al. [163] report an increase of crystallite size with respect to the pure PP, whereas we and others [136] find a decrease. According to the Deshmane paper the addition of MMT is not accompanied by a decrease of mechanical properties. In contrary, the authors report an increase of Young's modulus by 50% and a considerable increase of the impact strength. An indication for the reason of the different results is the different crystallite size. The small and imperfect crystallites in our composites may be weaker than the extended crystallites grown in the composite prepared by Deshmane et al. [163]. A comparative study has reported [134] that the alteration of polypropylene nanostructure by clay is not only a function of the pre-treatment, but also of the geological origin of the clay. Thus the reason for the different findings may probably be the sensitive response of different polypropylene grades on different nucleating agents, MMT, and compatibilization. Consequently, our results indicate that blending a nucleating additive into a polypropylene grade may require re-optimization of its formulation. In a first step, one could try to reduce the supplier-provided nucleators [165–168] of the grade.

A decrease of crystallite size may be considered a decrease of filler particle size in the amorphous matrix. Theories of particulate reinforcement predict no influence of the filler size on the mechanical properties, although frequently an increase is empirically found [169]. On the other hand, Sumita et al. [170] report that for polypropylene also the opposite behavior can be observed. The reason may be that below a certain crystallite size further reduction will probably lead to weakening of the filler particle.

Compatibilization. The pathway to cure the shortcomings of a blend is compatibilization. The result is a nanocomposite. In our experiments the compatibilizer itself appears to inhibit crystal growth additionally (Figure 6.10 at $\varepsilon = 0$). On the other hand, addition of more compatibilizer makes the nanostructure more stable when subjected to mechanical loading (Figure 6.3, Figure 6.4, Figure 6.8). Admittedly, this stability is the stability of an already degraded structure. As shown by the necking-induced local strain-relaxation (Figure 6.2), the compatibilizer increases the elasticity of the material.

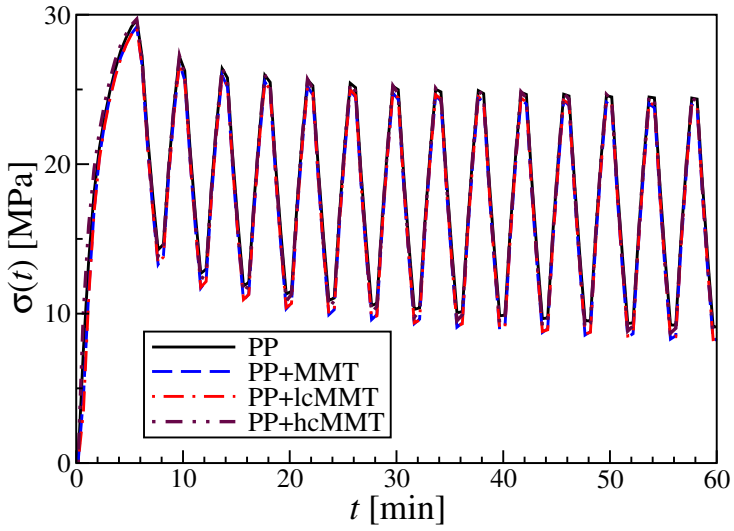

Figure 6.12: Slow load-cycling of PP/MMT materials in the synchrotron beam. True stress $\sigma(t)$ as a function of the time t

6.8 Load-Cycling Experiments

Figure 6.12 shows the evolution of the true stress in the load-cycling experiments. The local strain $\varepsilon(t)$ is the dynamic stimulus. It is identical for all materials and presented in some of the following figures. Macroscopic fatigue of the materials is indicated by the decay of the peak stresses from cycle to cycle. Among the 4 materials the difference appears small. In order to quantify the macroscopic fatigue, the decay of the peak stresses has been evaluated quantitatively. Figure 6.13 shows the data in a semi-logarithmic plot. In order to linearize the data, a residual stress σ_r has been subtracted. From the add-on decay the lifetime of macroscopic stress fatigue, τ_σ has been computed by logarithmic regression using the equation $y = k\exp(-t/\tau)$ (results in Table 6.1). Here k and τ are the regression parameters with τ the lifetime of the decay.

The nanoscale response of the material is evaluated from the long period peak of the CDFs that have been computed from the SAXS patterns. The evolution of the most probable long periods L during load-cycling is presented in Figure 6.14. The measured amplitudes are very low because the elongation of $h_{ca}(r_{12}, r_3)$ in r_3-direction is non-affine (see Section 6.6). For all materials the responses $L(t)$ are in phase with the stimulus $\varepsilon(t)$. This has been expected because of the low load-

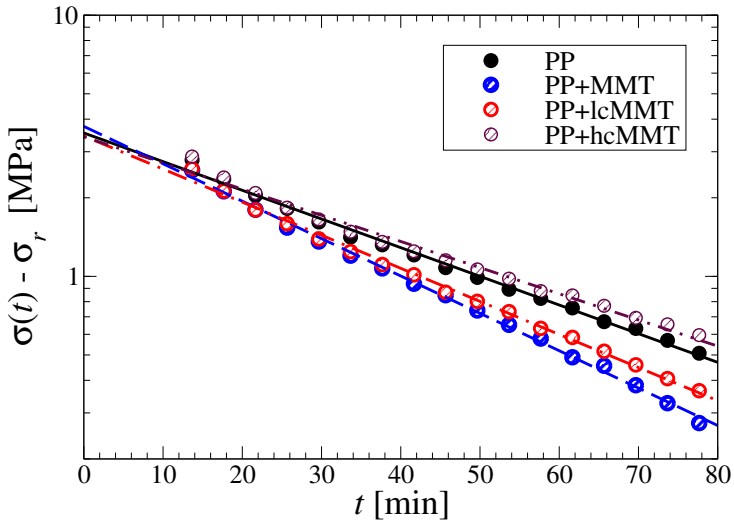

Figure 6.13: Slow load cycling of PP/MMT materials. Assessment of fatigue by exponential regression using the oscillation maxima of Figure 6.12. In order to linearize the plot $\sigma_r = 23.6$ MPa was subtracted for PP and PP+hcMMT. $\sigma_r = 23.4$ MPa linearizes the data of PP+MMT and PP+lcMMT

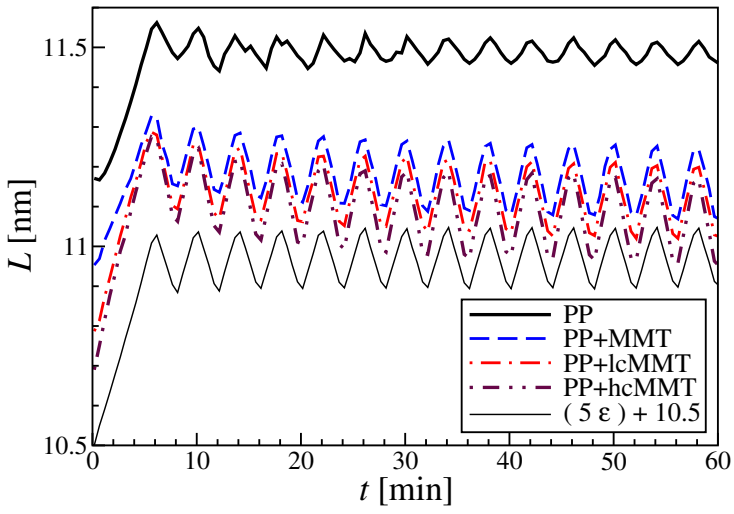

Figure 6.14: Nanostructure evolution during load cycling of PP nanocomposites determined from the CDF long period peak. Most-frequently long period $L(t)$ as a function of the elapsed time t. Additionally the local macroscopic strain $\varepsilon(t)$ is shown

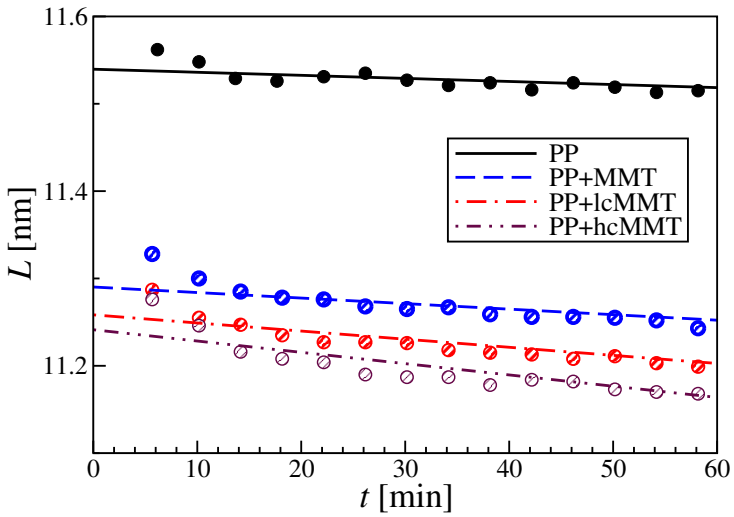

Figure 6.15: Assessment of nanostructure fatigue. Fit of the oscillation maxima from Figure 6.14 by an exponential for determination of the lifetime τ_L of long period decay

Table 6.1: Fatigue in a slow load-cycling experiment (cycle time 4 min) estimated from exponential fits. The lifetimes τ_σ, τ_L, τ_e, and $\tau_{\Delta L}$ characterize the macroscopic stress fatigue, the nanoscopic long period fatigue, the nanoscopic lamella-extension fatigue, and the nanoscopic structure-heterogeneity fatigue, respectively. Data in brackets are only based on a part of the curve (cf. Figure 6.19)

sample	τ_σ [min]	τ_L [d]	τ_e [h]	$\tau_{\Delta L}$ [min]
PP	39	23.1	5.8	110
PP+MMT	30	12.4	0.9	43
PP+lcMMT	34	8.4	1.7	50
PP+hcMMT	43	6.1	[1.0]	[140]

cycling frequency. Nanostructure fatigue is manifested in the underlying decay of $L(t)$. The fit of the peak L-values with an exponential function (Figure 6.15) yields a quantitative assessment of nanostructure fatigue (Table 6.1). Because the data are already linear in a semi-logarithmic plot, a residual does not need to be subtracted here.

Table 6.1 shows that the lifetime τ_L of the long period decay is halved as MMT is blended in. Addition of the full amount of compatibilizer weakens the semicrystalline nanostructure of the polypropylene even more. The decay is accelerated by another factor of 2. Thus the introduction of MMT and compatibilizer reduce the polypropylene self-reinforcement to 25% of its initial performance. The effective

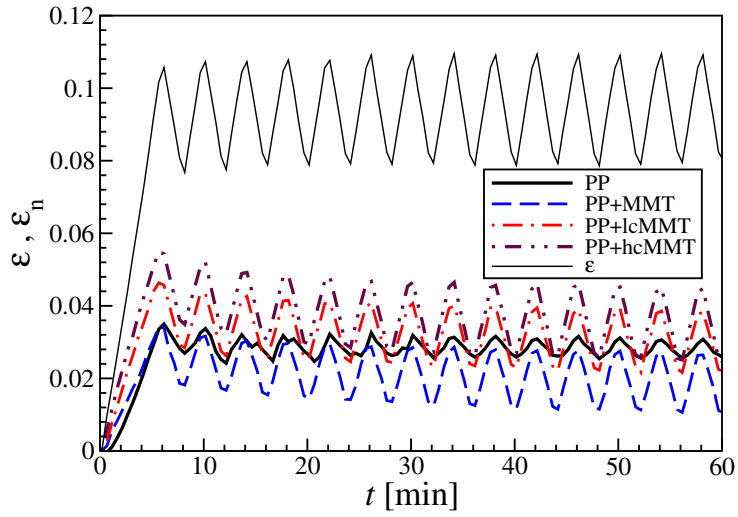

Figure 6.16: Evolution of the nanoscopic strain, ε_n, during load cycling of PP nanocomposites computed from the variations of CDF long period peak.

performance of the materials can be estimated from the lifetime of the macroscopic stress decay, τ_σ. Table 6.1 shows, that the blend has a reduced performance of $100 \times 21/27 \cong 77\%$ with respect to the commercial polypropylene grade. Only the compatibilization of the MMT with 8% amphiphilic block copolymer leads to a slight performance gain to 111%.

Figure 6.16 shows the variation of the nanoscopic strain ε_n during load-cycling. By its definition ε_n measures the deformation of well-correlated lamellae stacks. The difference between ε and ε_n indicates a heterogeneous strain distribution in the sample. Adding MMT to the polypropylene matrix (PP+MMT) enhances strain-heterogeneity (lower values of ε_n). The nanocomposite samples show higher ε_n values compared to PP. This can be attributed to the softening effect[1] of the low-molecular weight compatibilizer [171, 172]. Time evolution of ε_n is already reflected in the variations of the long period (see above).

The dynamic variation of the lateral extension $e_{12}(t)$ of the layers during load-cycling is presented in Figure 6.17. The initial levels are somewhat higher than those reported from the plain tensile experiments, but this is only related to different data pre-evaluation. For this analysis we had to take out a step, namely an

[1] strain-heterogeneity and the effects of compatibilizer are explored further in the discussion of MFC materials in Chapter 7

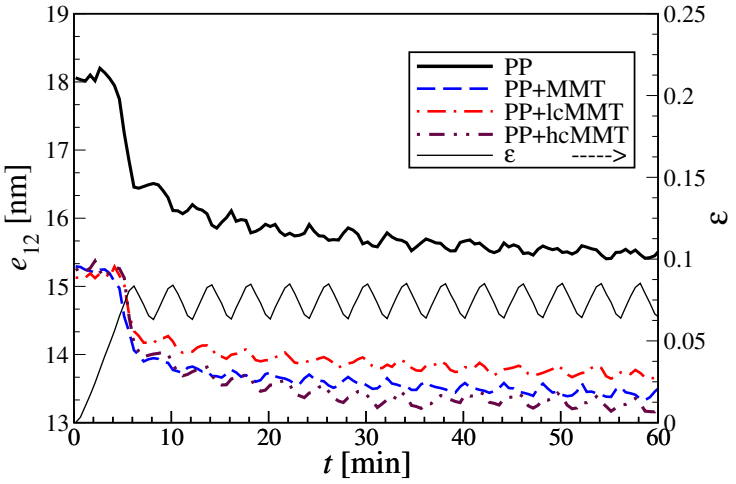

Figure 6.17: Nanostructure evolution during tensile testing of PP nanocomposites determined from the CDF long period peak. Average lateral extension $e_{12}(t)$ of the crystalline PP domains as a function of the elapsed time t. Additionally the macroscopic strain $\varepsilon(t)$ is shown

extrapolation of the scattering intensity to high angles. The extrapolation proved not to be stiff enough, and the noise introduced by extrapolation was higher than the weak variation of $e_{12}(t)$.

Layer-extension reduction starts after 4 min at $\varepsilon \approx 0.06$ and $\sigma \approx 27$ MPa for all studied materials. Thus the lag-time of lamellae disruption is not changed in the MMT-containing materials with respect to pure PP.

When the cycling starts, all materials respond with small oscillations about a monotonous decay. Thus the fatigue of the nanostructure with respect to the breaking of crystalline layers can, again, be analyzed by exponential regression. Because the oscillations are not well-expressed but we know that we have 8 SAXS patterns per cycle, this time the data are prepared for regression by sampling 8 points in a running average. A residual layer extension, $e_r = 13.2$ nm is subtracted in order to linearize the data sets in a semi-logarithmic plot. An exception is the curve of PP+hcMMT. It cannot be linearized over the full length of 85 min and the data look strange for $t < 40$ min. The corresponding lifetimes τ_e of the lamellae extension are reported in Table 6.1. The blending with MMT reduces the lifetime of the lamellae extension to 15%, but in the composite PP+lcMMT the lifetime has recovered to 30% of the initial value. The determined value for PP+hcMMT is based on a short interval ($t > 40$ min). Thus its significance is questionable, and

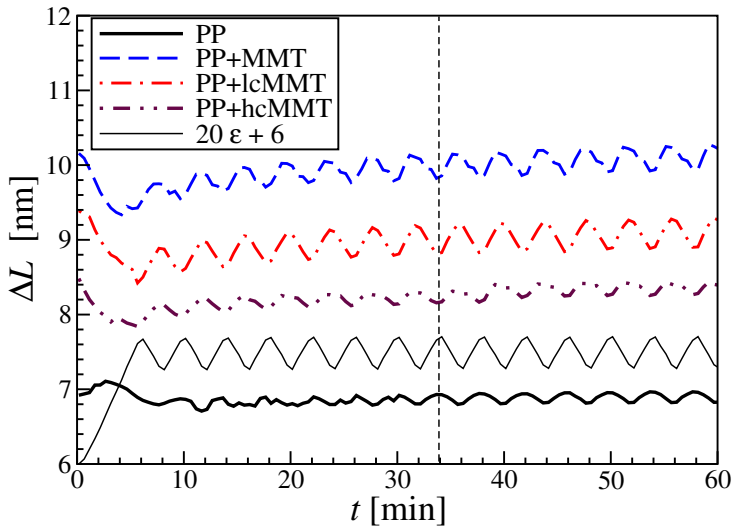

Figure 6.18: Nanostructure evolution during load cycling of PP nanocomposites determined from the CDF long period peak. Breadth $\Delta L(t)$ of the long period distribution. Additionally the local macroscopic strain $\varepsilon(t)$ is shown

in the table the value is enclosed in brackets.

Figure 6.17 exhibits a peculiar variation of the phase of the responses $e_{12}(t)$ on the dynamic strain $\varepsilon(t)$. For samples that are no composites (PP, PP+MMT) the layer extensions are low at the peak strains and vice versa. On the other hand, for the composites (PP+lcMMT, PP+hcMMT) the macroscopic stimulus $\varepsilon(t)$ and the nanoscopic response $e_{12}(t)$ are in phase. An explanation may be given that is based on a result of an earlier load-cycling study of pure PP [148] combined with the notion that in a composite matrix and filler are well bonded. In the earlier study the transition from strain-induced crystallization to crystallite disruption was found at $\sigma \approx 20\,\mathrm{MPa}$. In the present load-cycling study, macroscopically the peak stress is well above the transition threshold. Thus in pure PP and in the blend many crystallites break. During the elongational branch of the cycles pieces of lamellae are moved apart. They recombine in the relaxational branch of the cycle. In the well-bonded composite the MMT bears part of the load, thus saving the polypropylene lamellae from breaking. On the other hand, the fraction of the load that is exerted on the polypropylene is low enough to guarantee a dominance of strain-induced crystallization over lamella disruption.

Figure 6.18 shows the breadth parameter $\Delta L = 3\sigma_3(h_{ca})$ of the long period

distribution h_{ca} as a function of time. It is related to the variability of the distances in straining direction between two crystallites. During the first straining the MMT materials exhibit decreasing heterogeneity of the nanostructure in straining direction, whereas it almost remains constant for sample PP. This has already been found in tensile testing (cf. Figure 6.10).

As a function of time sample PP exhibits during the first 7 cycles small variations about a constant level $\Delta L \approx 6.8\,\mathrm{nm}$. Thereafter the material starts to respond to the macroscopic strain $\varepsilon(t)$ by a clear low-amplitude oscillation of $\Delta L(t)$. It is in phase with $\varepsilon(t)$. Thus the arrangement of crystallites becomes more heterogeneous in each straining branch and returns to a more homogeneous state during relaxation. There is little fatigue related to the arrangement of crystallites. This behavior is readily explained by non-affine straining of layer stacks that contain durable crystallites in which the low long period stacks are less extensible than the high ones.

Compared to sample PP the behavior of the MMT materials is characterized by 4 features. First, they show higher heterogeneity. Second, they respond from the beginning by a high-amplitude oscillation. Third, the phase of the oscillation is inverted with respect to the stimulus $\varepsilon(t)$ (cf. arrows in Figure 6.18). Thus the distances between the crystallites become more uniform in each straining branch and relax into a more inhomogeneous state. A possible explanation is based on the assumption of a considerable fraction of undersized, premature crystallites that are too weak to withstand even moderate strain. Disintegration by chain-unfolding leads to a loss of long periods at small r_3 in $h_{ca}(r_{12}, r_3)$, and a carry over to greater r_3. h_{ca} becomes more uniform. During the relaxation branch the corresponding chains fold again to form an undersized crystal, and the breadth of h_{ca} broadens again.

Fourth, the heterogeneity of the MMT samples is increasing from cycle to cycle exhibiting nanostructure fatigue. The reason for this nanostructure fatigue remains speculative. Let us assume that the premature state of the semi-crystalline morphology itself is the reason. Then, under dynamic load it is easily worn down, leaving behind a broad spectrum of different long periods.

The corresponding lifetime analysis based on running averages $\overline{\Delta L}(t)$ of $\Delta L(t)$ is presented in Figure 6.19. It shows the strange breakdown in the data from sample PP+hcMMT (full data set marked by circles), the running-average curves and

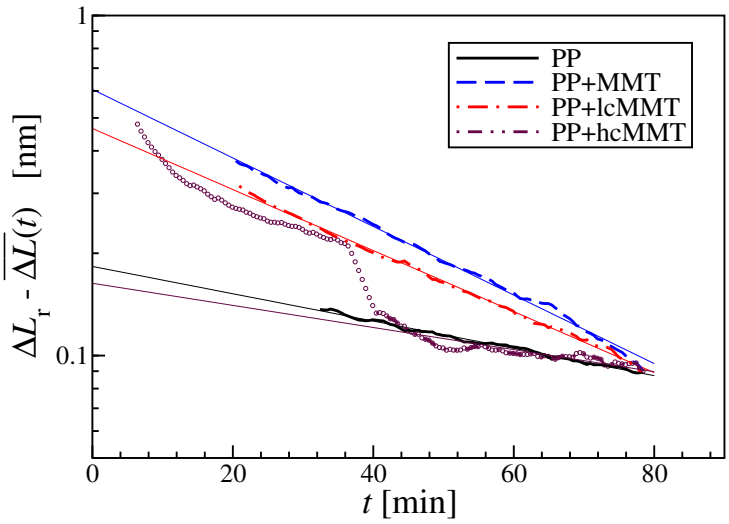

Figure 6.19: Nanostructure heterogeneity fatigue. Determination of lifetimes $\tau_{\Delta L}$. $\overline{\Delta L}(t)$ is the running average of the curves from Figure 6.18. Small circles show the complete set of PP+hcMMT containing the strange breakdown

their fit by an exponential. The corresponding lifetimes $\tau_{\Delta L}$ are documented in Table 6.1. Obviously, the increase of nanostructure heterogeneity under dynamic load is doubled by addition of MMT to PP. The compatibilizer in the composites helps to reduce this fatigue.

The evolution of the scattering power Q under dynamical load is almost trivial. The curves do not change significantly during the cycling. This means at least that there is not much change of contrast or void content during the load cycling.

Finally, an oversimplified cartoon of the nanoscale morphology is presented in Figure 6.20. It shows a rather well-developed lamellar structure in the polypropylene, and in the materials that contain MMT a distorted layer structure that is reinforced by the silicate layers depicted as thin vertical domains.

The findings of this study can be summarized as follows:

1. By comparing the extracted nanostructure evolution information to the mechanical data it has been found that missing improvement of mechanical properties appears to result predominantly from the inhibition of a load-bearing semi-crystalline morphology inside the PP by the MMT.

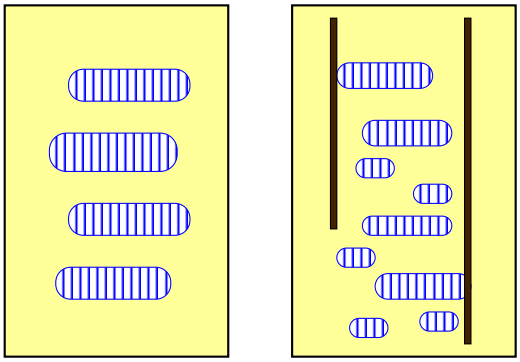

Figure 6.20: Simplified structural model for the semicrystalline structure of the pure polypropylene (left) and of the polypropylene phase in the nanocomposites (right). The thin vertical domains are drawn only to indicate that the composite contains MMT layers

2. Chemical compatibilization [123, 173, 174] appears to be a secondary effect with the studied polypropylene grade. In fact, the predominant deterioration of mechanical properties of PP by nucleating mineral fillers has been reported in the literature [175].

3. Load-cycling the materials below the yield exhibits macroscopic and nanoscopic fatigue detected from a decay of the peak stresses and peak nanostructure parameters, respectively. From the respective lifetimes we have for the first time assessed the reinforcement of the composite and the weakening of the PP by the MMT. It has been found that crystallite growth is obstructed even more when MMT is compatibilized. It remains to be clarified, if this effect is caused by the compatibilizer itself or by improved exfoliation of the MMT.

4. With respect to application the results indicate that the optimization of a commercial PP grade undertaken by the manufacturer may be lost when it is bonded to a filler with nucleating capacity. If the optimization of the formulation has to be redone, one could start from a PP grade without nucleators.

Chapter VII

HDPE/PA Microfibrillar Composites Under Load-Cycling

Microfibrillar reinforced composites (MFC) are polymer-polymer composites in which both the isotropic matrix and the fibrous anisotropic reinforcements are formed *in-situ* during processing [79, 176]. MFC materials promise both improved properties during service and low ash content after incineration [177–179]. The first feature is required to replace metals by light-weight parts in automobiles. The second feature is a European legislative request [180–182] that must be met in the future. In many practical applications that MFCs are designed for, the materials are subjected to cyclic (dynamic) load. Hence, resistance [183] to dynamic loads (i.e. low fatigue[184–186]) is required. In this chapter we examine the evolution of the nanostructure under slow load-cycling in HDPE/PA oriented MFC precursors that have not been subjected to the final compression molding processing step which removes [80, 187] the orientation of the HDPE matrix.

7.1 Micro– vs. Nanostructure

On the micrometer scale the morphology of HDPE/PA oriented precursors has been studied by scanning electron microscope (SEM) in previous works [187, 188]. Based on SEM micrographs the average diameter of polyamide microfibrils is 550 ± 100 nm, strongly depending on the HDPE/PA ratio of the cold drawn blend. The length of polyamide microfibrils has been estimated 30-90 µm. Generally, addition of compatibilizer causes a reduction in both diameter and length of polyamide microfibrils [187, 188].

On the nanometer scale the structure of the samples is studied by SAXS. Figure 7.1 sketches structural features that can be probed by SEM on the micrometer

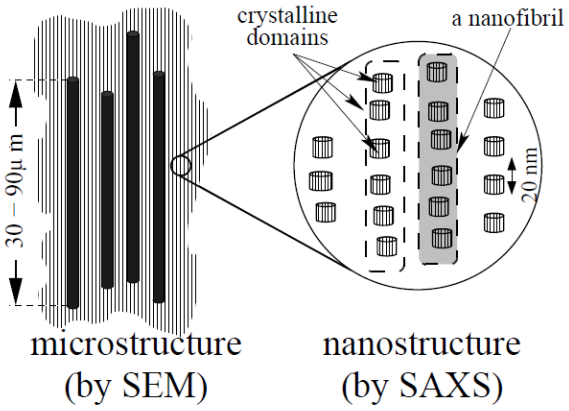

Figure 7.1: Sketch of typical MFC multi-scale structure at micrometer (left) and nanometer scale (right). Processing direction is vertical. SEM can probe polyamide microfibrils (dark rods) embedded in a fibrillated HDPE matrix [187, 188]. SAXS monitors mainly the semi-crystalline nanostructure of the HDPE matrix. Crystalline domains are frequently arranged in processing direction forming nanofibrils (in the conceptual notion of microfibrils[99]). One nanofibril is highlighted in gray

scale and by SAXS on the nanometer scale, respectively. The SAXS of the samples arises mainly from the semi-crystalline structure of the HDPE matrix, as has previously been shown [80]. The reasons are, firstly, that the major component is HDPE. Secondly, polyamide has a low electron density contrast between its crystalline and amorphous regions compared to the corresponding contrast in HDPE.

7.2 Nanostructure of Undeformed Materials

For the undeformed samples Figure 7.2 shows the scattering intensities $I(s_{12}, s_3)$ and the absolute values of the corresponding CDFs $z(r_{12}, r_3)$. All samples exhibit a layer-line scattering pattern. It is characteristic for a highly oriented structure from slender domains arranged in rows along the fiber axis. The layer lines are not indented or even split into separate peaks. Thus there is only one-dimensional arrangement of domains. This fact is obvious from the CDF data in real space (Figure 7.2, bottom row). Its peaks and their arrangement directly demonstrate the domains slenderness and their arrangement in fiber direction. The corresponding semi-crystalline morphology is usually called "*microfibrillar*" [99, 100]. Instead, in

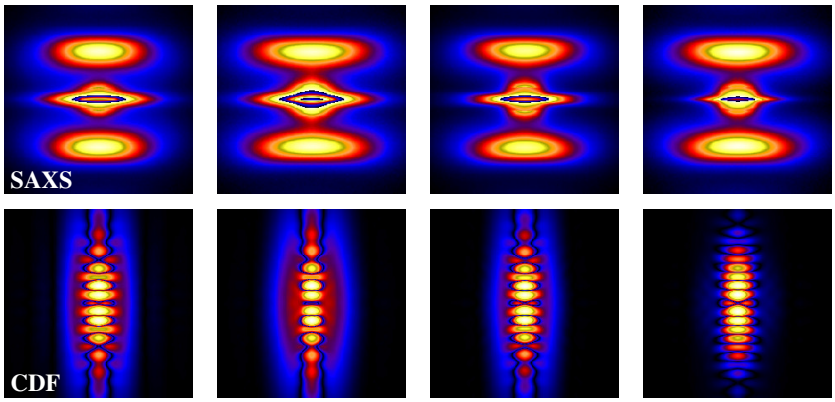

Figure 7.2: Undeformed samples. SAXS fiber diagrams $I(s_{12}, s_3)$ (top row) and the corresponding CDFs $|z(r_{12}, r_3)|$ (bottom row). Displayed regions: $-0.1\,\mathrm{nm}^{-1} < s_{12}, s_3 < 0.1\,\mathrm{nm}^{-1}$, $-100\,\mathrm{nm} < r_{12}, r_3 < 100\,\mathrm{nm}$. Intensities on logarithmic scale. Fiber axis is vertical

Table 7.1: Undeformed samples. Essential nanostructure parameters extracted from the CDFs. long period, L, and an average lateral extension e_l of the crystalline domains

sample	L [nm]	e_l [nm]
P6HY(20/80/0)	18.6	16.2
P6HY(20/70/10)	18.2	15.1
P12HY(20/80/0)	18.3	16.2
P12HY(20/70/10)	18.9	17.3

this chapter we call it *"nanofibrillar"*, in order to discriminate it from a microfibrillar structure on the micrometer scale (cf. Figure 7.1). The central equatorial streak in the SAXS patterns arises from the envelope of the nanofibrils and from other needle-shaped entities like voids [147, 189].

Table 7.1 presents essential nanostructure parameters for the undeformed materials that have been extracted from the strong long period peak in the CDF. The reported values are averages of measurements from 4 different pieces of the strands. They vary by 5 %. This indicates a slight structure heterogeneity. Table 7.1 shows that there is little influence of materials composition on the essential nanostructure of the HDPE nanofibrils.

In the CDFs from Figure 7.2, the PA12-reinforced samples show clearer peaks than the PA6-reinforced materials. Figure 7.3 demonstrates this feature quantitatively by curves cut from the CDFs along its meridional axis. The CDFs of PA12-

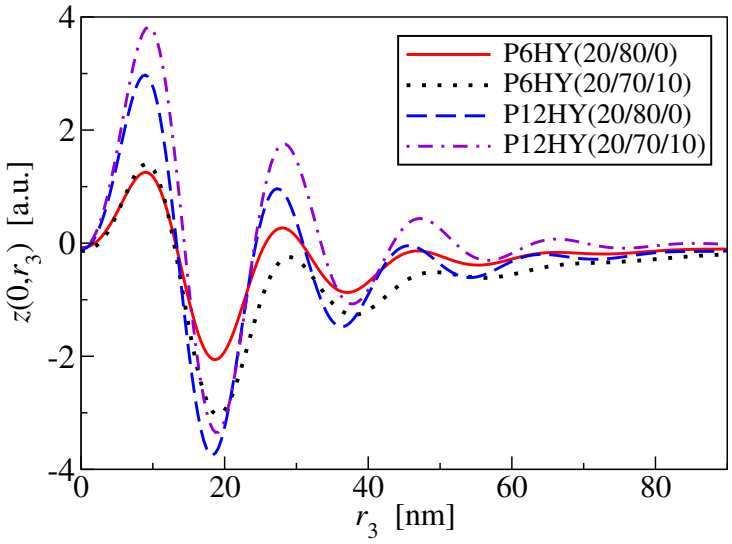

Figure 7.3: Comparison of $z(0,r_3)$ of undeformed samples. Diffuse merging of the 3rd and 4th negative peaks with the PA6-samples indicates poorer stacking of crystalline domains in its HDPE matrix

reinforced materials exhibit four separable long period peaks corresponding to at least five correlated lamellae. However, in the CDFs of the series containing PA6 already the 3rd and 4th long period peak become diffuse and merge. Thus the semi-crystalline HDPE stacks from the blends containing PA6 show more disorder than the respective stacks in blends containing PA12.

7.3 General Nanostructure Evolution in Load-Cycling Tests

During the mechanical tests SAXS patterns have been recorded continuously. Qualitatively these patterns are very similar, as is demonstrated in Figure 7.4. Hence, it is necessary to extract structural parameters from the patterns with high precision and to analyze their variations. Inspection of the shape-evolution of the CDF peaks shows affine deformation, in contrast to TPU materials (cf. Chapter 5). Thus the introduced simple nanoscopic structure parameters discussed here are considered to correctly describe the average response of the nanostructure to the applied macroscopic strain.

The evolution of macroscopic-mechanical and of nanoscopic parameters during load-cycling tests is presented in Figure 7.5 – Figure 7.8.

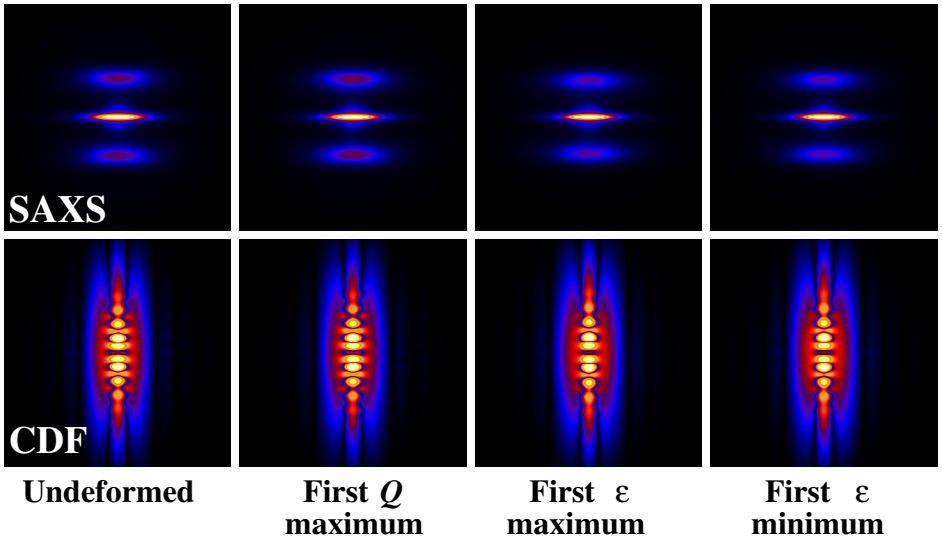

Figure 7.4: Qualitative similarity of scattering data recorded during load-cycling experiments. Shown are patterns from states of extreme difference during the testing of P6HY(20/80/0) cycled about high pre-strain (8-10%). SAXS fiber diagrams $I(s_{12}, s_3)$ (top row) and the corresponding CDFs $|z(r_{12}, r_3)|$ (bottom row). Displayed regions: $-0.15\,\mathrm{nm}^{-1} < s_{12}, s_3 < 0.15\,\mathrm{nm}^{-1}$, $-75\,\mathrm{nm} < r_{12}, r_3 < 75\,\mathrm{nm}$. Intensities on logarithmic scale. Fiber axis is vertical

7.3.1 Response of Stress and Nanoscopic Strain

In all tests the macroscopic response $\sigma(t)$ to the applied signal $\varepsilon(t)$ is rather simple. The monotonous branches of the saw-tooth function $\varepsilon(t)$ are immediately responded by monotonous branches of $\sigma(t)$. Thus little phase-shift is observed in these low-frequency load-cycling experiments.

Compatibilization increases (Figure 7.6) the stress $\sigma(t)$ for the material reinforced by PA6, as compared to the uncompatibilized sample (Figure 7.5). At $\varepsilon = 0.06$ the stress increases from 62 MPa to about 80 MPa. The plus with respect to the PA12-reinforced blend is readily explained by the more effective compatibilization in PA6. Due to its different molecular structure, i.e., the lower amounts of CH_2–groups in the repeat units, the chemical bonds between N-atoms from the PA6 and the anhydride groups from the maleinized HDPE of the compatibilizer are twice as many as in the case when PA12 reacts with the same compatibilizer [187].

The response of the nanoscopic strain ε_n to the macroscopic strain ε during plain straining is reported in Figure 7.9. The nanoscopic strain is smaller than the

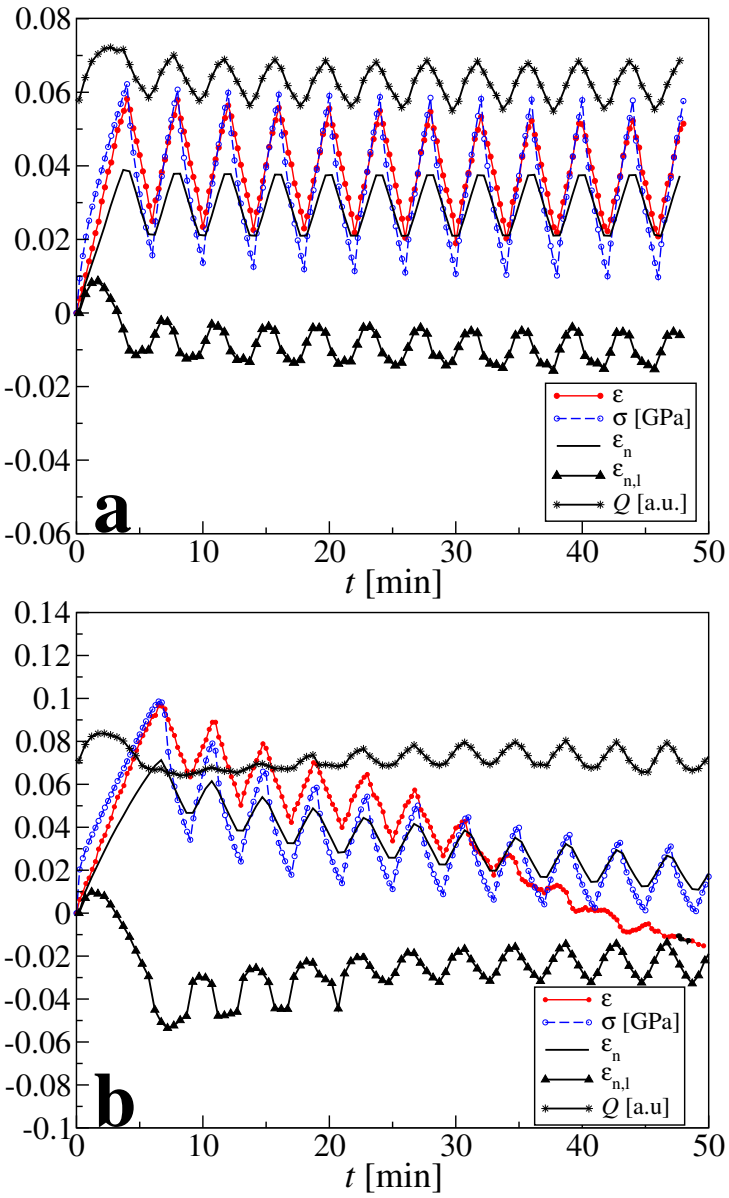

Figure 7.5: P6HY(20/80/0) load cycling. Mechanical and nanostructure parameters. (**a**) material cycled about low pre-strain (ca. 5%). (**b**) material cycled about high pre-strain (ca. 8%). Mechanical parameters: strain ε and stress σ. Nanostructure parameters: nanostrain ε_n, lateral nanostrain, $\varepsilon_{n,l}$, and scattering power Q. In the high-cycling experiment ε becomes negative

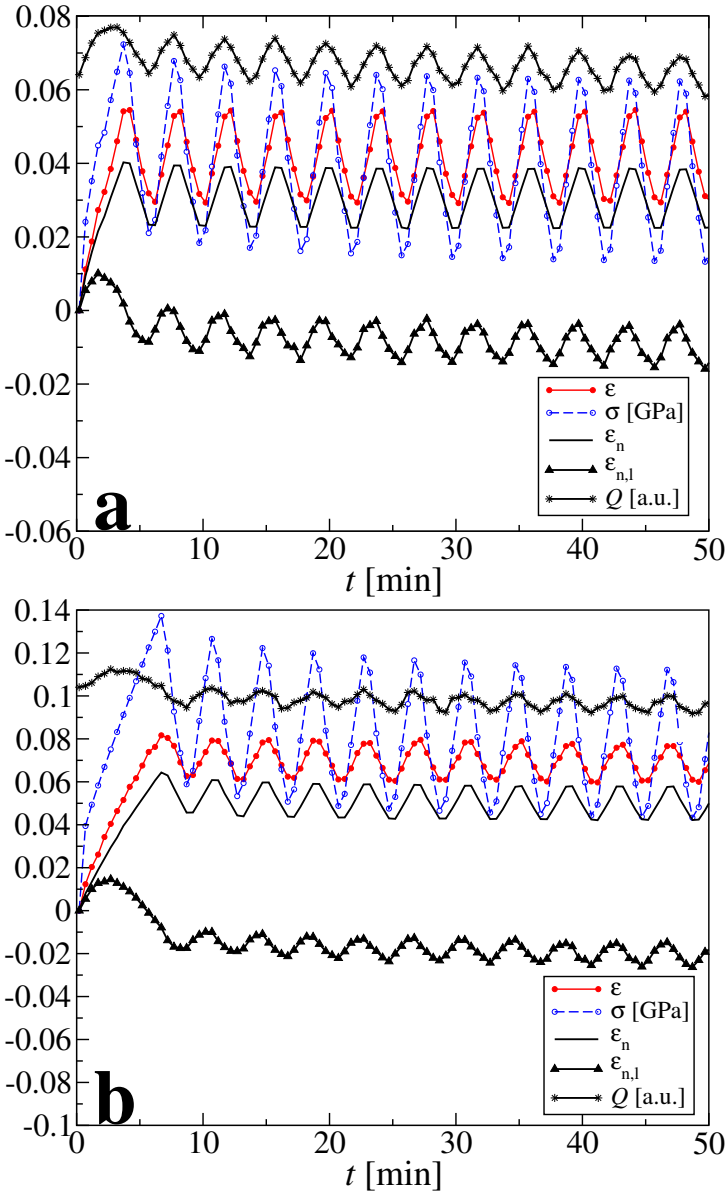

Figure 7.6: P6HY(20/70/10) load cycling. Mechanical and nanostructure parameters. (**a**) material cycled about low pre-strain. (**b**) material cycled about high pre-strain. Mechanical parameters: strain ε and stress σ. Nanostructure parameters: nanostrain ε_n, lateral nanostrain, $\varepsilon_{n,l}$, and scattering power Q

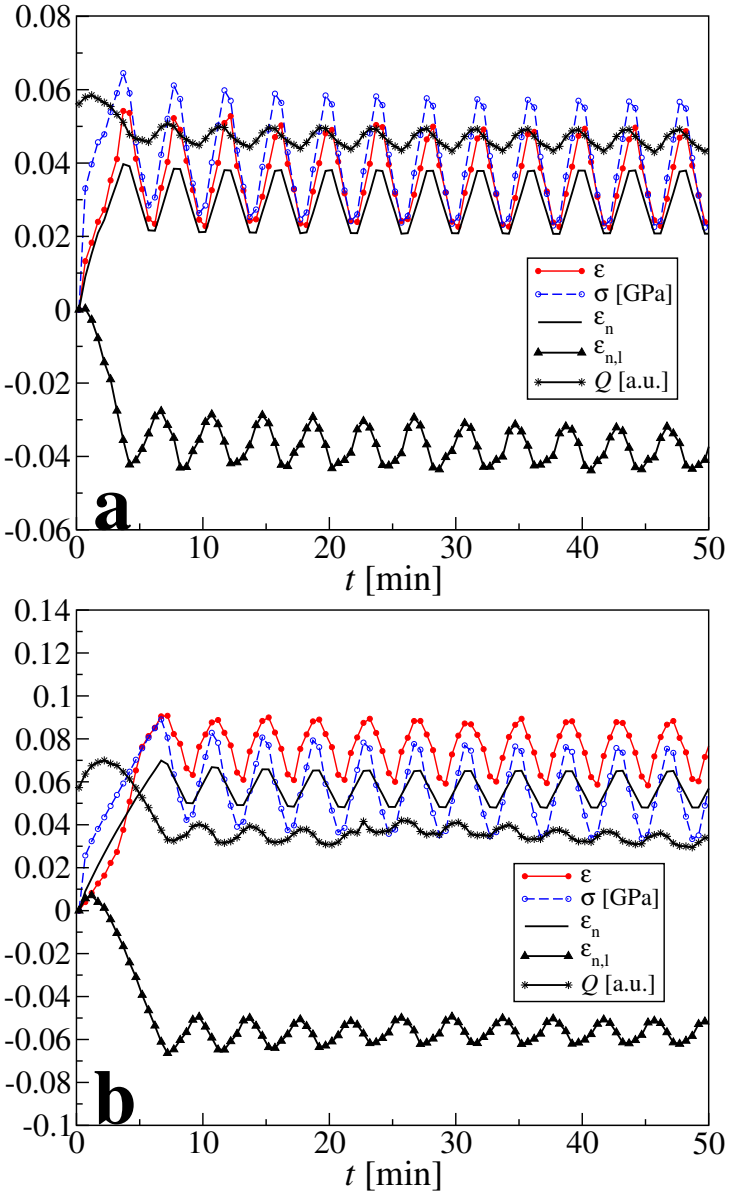

Figure 7.7: P12HY(20/80/0) load cycling. Mechanical and nanostructure parameters. (**a**) material cycled about low pre-strain. (**b**) material cycled about high pre-strain. Mechanical parameters: strain ε and stress σ. Nanostructure parameters: nanostrain ε_n, lateral nanostrain, $\varepsilon_{n,l}$, and scattering power Q

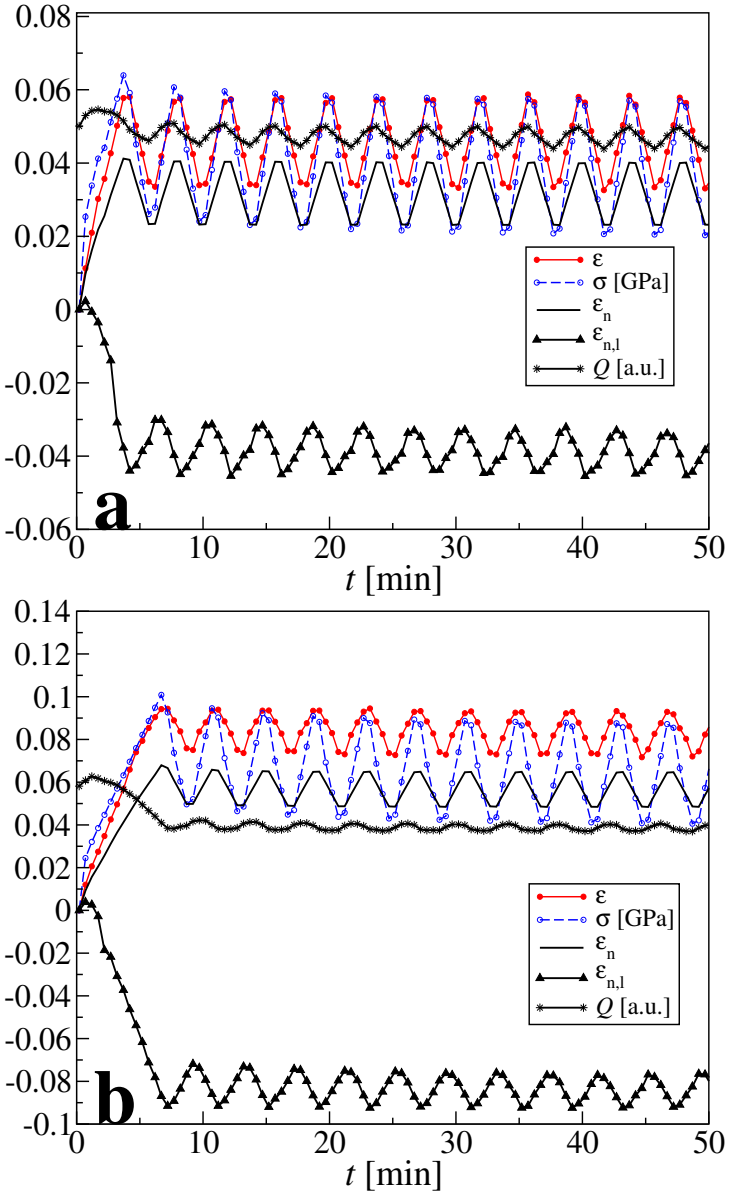

Figure 7.8: P12HY(20/70/10) load cycling. Mechanical and nanostructure parameters. (**a**) material cycled about low pre-strain. (**b**) material cycled about high pre-strain. Mechanical parameters: strain ε and stress σ. Nanostructure parameters: nanostrain ε_n, lateral nanostrain, $\varepsilon_{n,l}$, and scattering power Q

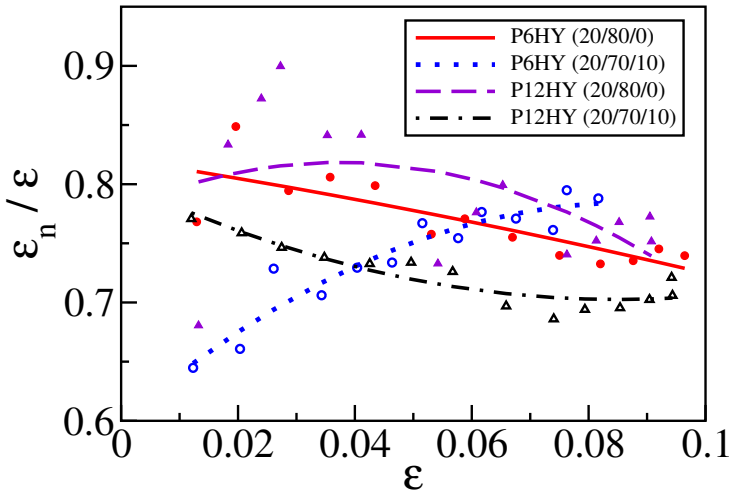

Figure 7.9: Relative nanoscopic strain, $\varepsilon_n/\varepsilon$, as a function of the local macroscopic strain ε. Data from the first straining branch. The curves are quadratic fits to the data

macroscopic strain ($\varepsilon_n < \varepsilon$). ε_n measures only the deformation of the HDPE semi-crystalline stacks. Humbert et al. [11] have monitored tensile tests of isotropic PE by SAXS. They report relative nanoscopic strains $\varepsilon_n/\varepsilon \approx 0.5$ for $0 < \varepsilon < 0.35$. Our measurements on oriented blends (cf. Figure 7.9) return values that are closer to the identity $\varepsilon_n = \varepsilon$. For low ε the compatibilized materials show a higher lag of ε_n than the uncompatibilized ones, and the material reinforced by PA12 performs somewhat closer to homogeneous strain than the material that contains PA6. With increasing strain ε, $\varepsilon_n/\varepsilon$ is, in general, further departing from the value $\varepsilon_n/\varepsilon = 1$. This means that in the plain strain experiments the strain heterogeneity is increasing for 3 of the 4 materials. An exception is P6HY (20/70/10) that shows the highest initial strain heterogeneity. Increasing the strain, the strain distribution in this sample becomes more homogeneous, i.e., the trend is inverted as compared to the other samples.

For load-cycling experiments (low pre-strain) Figure 7.10 presents $\varepsilon_n/\varepsilon$ data. During the test the material P6HY (20/80/0) (Figure 7.10a) is building up a considerable variation in $\varepsilon_n/\varepsilon$ as a function of ε. As ε is already low, ε_n is still high. Thus here ε_n shows a considerable phase-shift, i.e. a retarded relaxation response. In Figure 7.10c a similar inclination of the line segments demonstrates that build-up of a retarded relaxation response is also observed with the other uncompatibilized material, P12HY (20/80/0). Nevertheless, here the effect is much weaker.

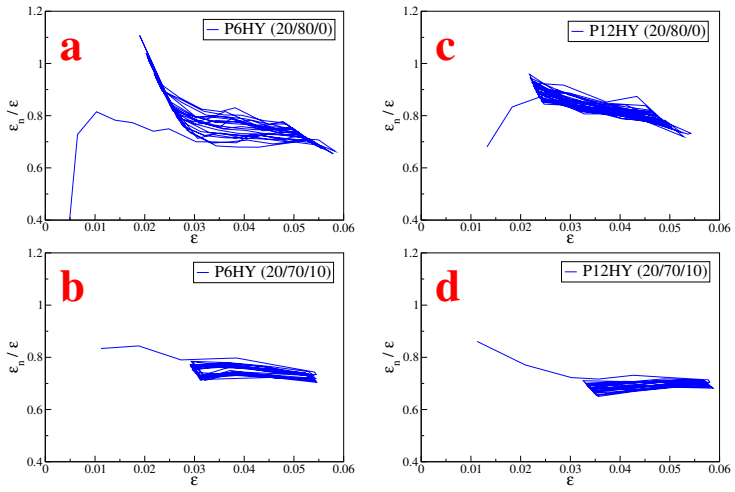

Figure 7.10: Relative nanoscopic strain, $\varepsilon_n/\varepsilon$, as a function of the local macroscopic strain ε. Data from the complete load-cycling experiments (low pre-strain)

Moreover, the lifting of the inclined line from cycle to cycle towards the level of homogeneity ($\varepsilon_n/\varepsilon = 1$) indicates homogenization of the strain distribution inside the material.

Addition of 10 wt.% compatibilizer (Figure 7.10b and Figure 7.10d) leads to continuous movement of $\varepsilon_n/\varepsilon$ away from the level of homogeneity from cycle to cycle. Thus strain heterogeneity in the compatibilized materials is growing under cyclic load. In summary, the compatibilizer induces strain heterogenization during load cycling, but suppresses the tendency of a retarded nanoscopic structure response.

Increasing strain heterogeneity in the HDPE phase during the cyclic loading of only the compatibilized materials may be explained by migration of unbound compatibilizer from the surfaces of the PA microfibrils into a heterogeneous HDPE matrix (cf. Figure 7.11). This matrix is built both from well-developed semicrystalline HDPE stacks that probe ε_n, and from a disordered fraction that has little effect on the long period feature seen by the SAXS. The latter matrix fraction is characterized by almost random placement of diverse crystalline domains. If the migrating compatibilizer is enriched more in the disordered than in the ordered fraction, it can be expected that it plasticizes predominantly the fraction of the HDPE matrix in which it is enriched. Consequently, the nanoscopic strain in the disordered fraction would increase from cycle to cycle, whereas the

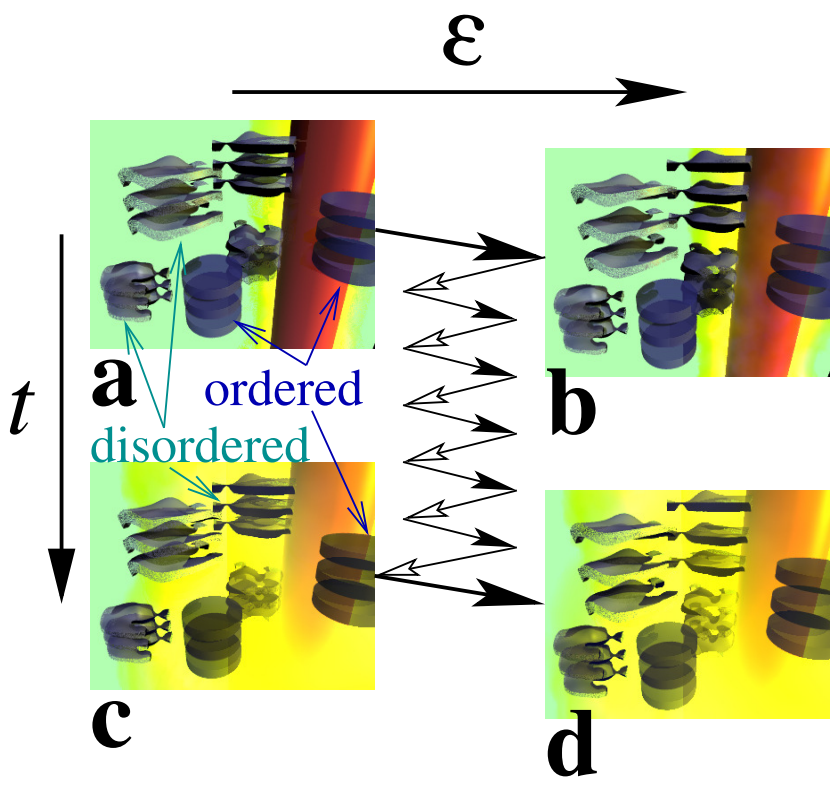

Figure 7.11: Mechanism of strain heterogenization by selective migration of compatibilizer (yellow haze) away from the PA microfibrils (long red rod) into the disordered fraction (distorted crystalline layers) of the HDPE matrix avoiding the ordered stacks (ideal crystalline discs). Reaching the upper dead center after some cycles (d) the distance between the distorted layers is longer than at the first maximum (b) because of a plasticizing effect of the compatibilizer. The course of macroscopic strain ε in time t is indicated by arrows

probed ε_n would decrease slightly, as is observed in the experiments. In the literature similar softening effects of compatibilizers on the matrix of nanocomposites have been reported [171, 172] and side-effects of additive migration in blends and composites have been studied [190–192]. It should be mentioned that the migration of compatibilizer into the polyamide cannot be studied by means of SAXS data from the studied materials.

7.3.2 Response of the Lateral Nanoscopic Strain

A different response scheme is observed with the lateral extensions $\varepsilon_{n,l}(t)$ of the crystallites. Figure 7.5 and Figure 7.6 present the data from the MFC precursors that contain PA6. Here, during the initial straining branch, $\varepsilon_{n,l}(t)$ is first increasing for small t indicating domain-growth at low ε. We propose to explain this growth of the crystalline domains by strain-induced crystallization [148]. From higher ε and σ, the average $\varepsilon_{n,l}(t)$ begins to decrease. This indicates that now the dominant effect is domain destruction under high stress. For the MFC precursors containing PA12 the corresponding data are presented in Figure 7.7 and Figure 7.8. Here no epitaxial strain crystallization is observed.

The cycles of $\varepsilon(t)$ that follow the first straining induce oscillations of $\varepsilon_{n,l}(t)$. For the PA6-materials (Figure 7.5 and Figure 7.6) a phase shift is observed. The maxima of $\varepsilon_{n,l}(t)$ are always found on the increasing branch of $\varepsilon(t)$. Again, this finding is explained by epitaxial strain crystallization in the lower part of the branch followed by domain disruption in the upper part. The decreasing branch of $\varepsilon(t)$ is initially responded by further decrease of $\varepsilon_{n,l}(t)$ that can be explained by relaxation melting. In the lower part of the relaxation branch $\varepsilon_{n,l}(t)$ already starts to increase again. A possible reason is defragmentation of broken HDPE crystalline domains. For the PA12-materials, on the other hand, the phases of $\varepsilon(t)$ and $\varepsilon_{n,l}(t)$ are opposite (Figure 7.7 and Figure 7.8). Again, this finding coincides with the missing of epitaxial strain crystallization in the first straining branch of these materials. It is compatible with the notion of mere crystallite disruption in the straining branches, and in the relaxation branches of re-composition by defragmentation.

Figure 7.12 sketches the proposed nanostructure evolution mechanisms of the PA6-materials (Figure 7.12a) and of the PA12-materials (Figure 7.12b). The

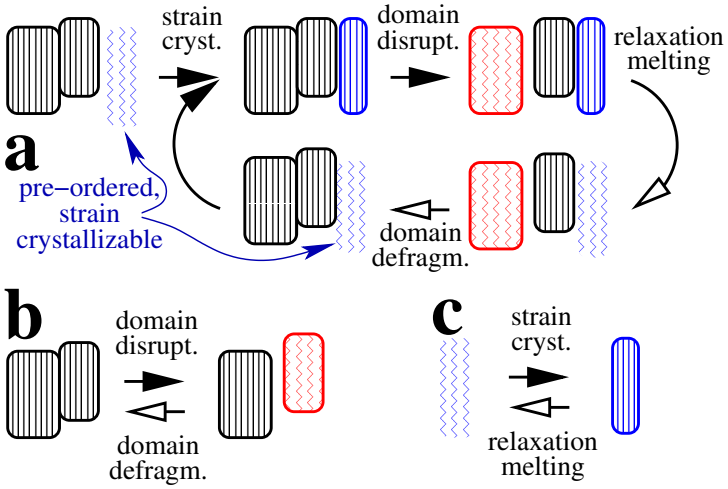

Figure 7.12: Schematic presentation of nanostructure evolution mechanisms during pre-straining and load-cycling. Only crystalline HDPE domains are depicted. Filled arrow-heads: Straining branches ($\dot{\varepsilon}(t) > 0$), open arrow-heads: relaxation branches ($\dot{\varepsilon}(t) < 0$). (**a**) Materials with PA6: The complex cycle includes epitaxial strain crystallization. (**b**) Materials with PA12: Simple cycle governed by domain disruption and domain defragmentation. (**c**) Speculative free strain crystallization for materials with PA12 from the evolution of the scattering power $Q(t)$

simpler scheme for PA12 can be explained by assuming that these materials do not contain enough pre-ordered amorphous PE chains around the crystalline PE domains to initiate significant domain growth by strain crystallization. Thus during the straining branches only continuous domain disruption and fragment dissolution is observed. During the relaxation branches the remnant pre-ordered amorphous regions from the fragments crystallize, and many of the original crystalline domains are reconstructed. Let us call this mechanism domain defragmentation. The PA6-materials, on the other hand, exhibit a more complex response to load-cycling that has also been found in a study [148] of pure polypropylene (Figure 7.12a). Here low stress suffices to extend and to crystallize pre-ordered PE chains that coat the crystalline domains. Higher stress disrupts crystalline domains and dissolves some of the fragments. Relaxation of some stress leads to melting of the strain-crystallized chains, and at very low stress fragments recombine.

The differences between low-pre-strain and high-pre-strain cycling is discussed by comparing the sub-figures a and b in Figure 7.5 – Figure 7.8, respectively. Ob-

viously, the samples that are exposed to high pre-strain suffer higher damage to the nanostructure. This damage is not recovered during the following load-cycling.

7.3.3 Response of the Scattering Power

The variation of $Q(t)$ is only moderate. Together with the complex structure information contained in Q this makes interpretation highly speculative. The common initial response scheme of the scattering power $Q(t)$ is similar to that of $\varepsilon_{n,l}(t)$. During the first straining branch of $\varepsilon(t)$, $Q(t)$ passes through a maximum. According to Eq. (2.22) the interpretation of $Q(t)$ requires assumptions. Most probably the contrast does not change considerably, and the void scattering in the equatorial streak appears to be constant (cf. Figure 7.4). Moreover, if we assume that the initial volume crystallinity v is lower than 0.5, an increase of Q indicates increasing crystallinity. This daring assumption would fit well to the results of $\varepsilon_{n,l}(t)$ for the samples containing PA6. On the other hand, the initial volume crystallinity v_0 of HDPE is normally higher than 0.5, and in this case an increasing value of $Q \propto v(1-v)$ would indicate decreasing crystallinity.

Only if we would be willing to assume a small-angle volume-crystallinity $v_0 < 0.5$, the initial evolution of $Q(t)$ were indicative for strain crystallization in all materials. This would mean that strain crystallization would occur even in the PA12-blends, but here it would mainly induce the formation of new HDPE crystalline domains ("free strain crystallization"), and epitaxial strain crystallization were negligible. At least after several cycles $Q(t)$ responds by an oscillation that is in phase with the signal $\varepsilon(t)$. Under the low-crystallinity assumption this finding would, again, indicate free strain crystallization during the straining branch followed by melting during the relaxation branch (cf. Figure 7.12c).

7.4 Plastic Flow in P6HY (20/80/0)

Figure 7.5b shows the data from the load-cycling experiment about high pre-strain of P6HY(20/80/0). In the low-cycling test this material has shown considerable retardation of the nanostructure relaxation response (cf. Figure 7.10a). In the high-cycling test after 40 min the ε returns negative values. This result is an artifact because the sample bends, whereas the distances between the fiducial marks are still measured along the fixed straight axis of the ROI. The bending is clearly

Table 7.2: Slow load cycling of MFC precursor materials. Extreme mechanical parameters and lifetime τ of stress fatigue. "Low" indicates cycling about $\varepsilon \approx 0.05$, "High" about $\varepsilon \approx 0.08$. σ_2/σ_{max} is the ratio of the 2nd to the 1st stress maximum

sample code	ε_{max}	σ_{max} [MPa]	σ_2/σ_{max}	τ [min]
P6HY(20/80/0) Low	0.058	62	0.96	24
P6HY(20/80/0) High	0.095	98	0.80	15
P6HY(20/70/10) Low	0.054	72	0.93	22
P6HY(20/70/10) High	0.081	137	0.91	15
P12HY(20/80/0) Low	0.054	64	0.95	26
P12HY(20/80/0) High	0.091	89	0.93	20
P12HY(20/70/10) Low	0.058	64	0.94	28
P12HY(20/70/10) High	0.094	100	0.93	19

observed in the video frames and demonstrates macroscopic plastic flow. Plastic flow is also indicated by the strong decrease of $\sigma(t)$. Moreover, this experiment is the only one that returns decreasing ε_n values. Thus the average distance between the crystallites from the nanofibrils (ordered stacks) is shrinking while the material is lengthened on the macroscopic scale. This combination of plastic flow and long period shrinkage can be explained by disentanglement of the HDPE chains outside the nanofibrils that leads to macroscopic plastic flow and eliminates frozen-in tension on the nanoscopic scale.

7.5 Material Fatigue

In common fatigue tests the macroscopic stress $\sigma(t)$ is controlled, and the strain $\varepsilon(t)$ is the macroscopic response. Because of the limited capabilities of our tensile tester we have controlled $\varepsilon(t)$. Thus $\sigma(t)$ is the macroscopic response, and macroscopic fatigue of the materials is indicated by the decay of the peak stresses from cycle to cycle. For a quantitative analysis the running average $\bar{\sigma}(t)$ has been computed over one period of the signal $\varepsilon(t)$. Figure 7.13 shows the variation of $\bar{\sigma}(t)$ in a semi-logarithmic plot together with lines that indicate an exponential regression using the equation $y = k\exp(-t/\tau)$. Here k and τ are the regression parameters with τ the lifetime of the decay. Lower lifetimes correspond to stronger fatigue.

Table 7.2 reports extreme values of the mechanical parameters and the life-

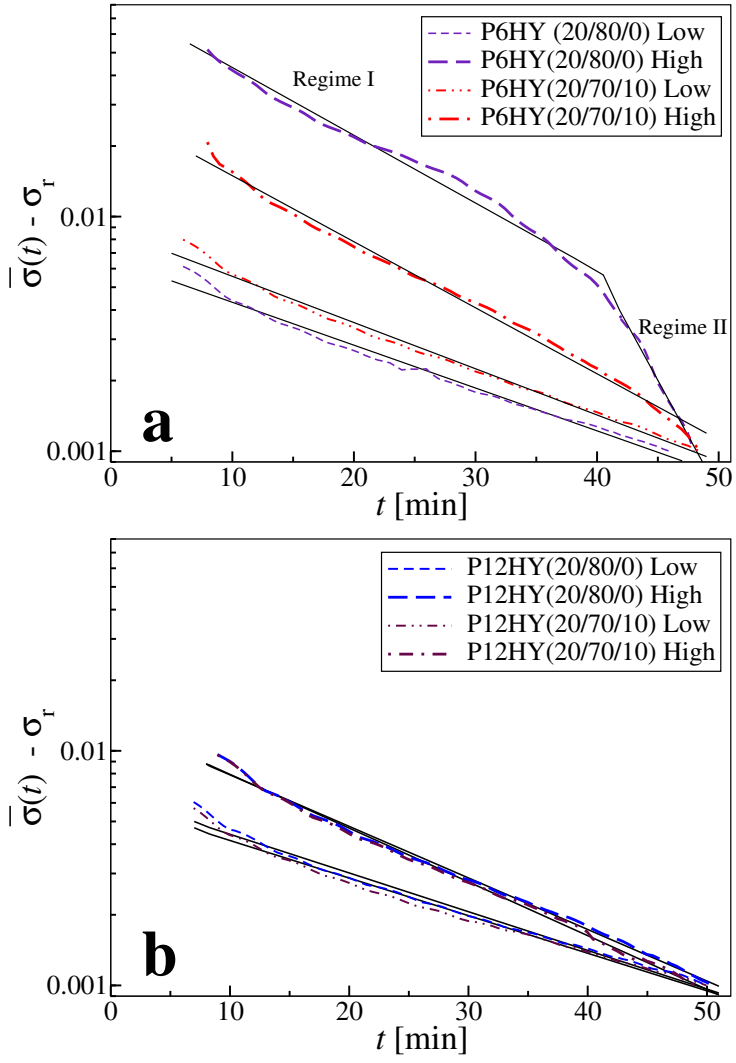

Figure 7.13: Assessment of fatigue by exponential regression of the macroscopic response $\bar{\sigma}(t)$. In order to linearize $\bar{\sigma}(t)$ a residual stress, σ_r, is subtracted. Here sufficient linearization has been obtained by setting $\sigma_r = \bar{\sigma}(t_{max})$. Solid straight lines illustrate the exponential fits to the data. (**a**) HDPE reinforced with PA6. (**b**) HDPE reinforced with PA12. The suffix **Low** indicates cycling about low pre-strain (ca. 5%) and **High** cycling about high pre-strain (ca. 8%). In high-cycling data of P6HY(20/80/0) two regimes are observed. Regime II is biased from sample bending after plastic flow

times τ determined from the load-cycling data. ε_{max} is the maximum strain, σ_{max} the maximum stress that is reached in the 1st maximum of load cycling, and σ_2/σ_{max} is the ratio of the 2nd to the 1st stress maximum. This value is included in the table because for $t < 10$ min the decay of $\bar{\sigma}(t) - \sigma_r$ is faster than the fitted exponential. Thus σ_2/σ_{max} is a better measure for the initial fast stress decay. Higher values of σ_2/σ_{max} mean less stress fatigue. The table shows that fatigue is higher when the sample is cycled about higher pre-strain. Fatigue is lower in the blends reinforced by PA12 than in the samples containing PA6. The low fatigue of PA12-materials may be explained by higher compatibility with HDPE due to the longer aliphatic chain segments of PA12. A practical explanation of the lower fatigue is the less-deteriorated semi-crystalline nanostructure of the HDPE in the PA12-materials (Figure 7.3). Apparently, addition of compatibilizer does not reduce the material fatigue significantly. This may be related to the finding that addition of the compatibilizer leads to strain heterogenization during load cycling (cf. Figure 7.10).

The results can be summarized as follows:

1. A side effect of a compatibilizer is heterogeneization of the polyethylene matrix. This is related to selective migration of unbound compatibilizer into those regions of the matrix where the semicrystalline nanostructure is predominantly made from imperfect crystals randomly distributed in the amorphous phase.

2. The observed heterogeneous strain distribution in the material may, ultimately, deteriorate the performance of the composite. This result indicates the complexity of composite design, because the desired effects of an additive or a processing step may be accompanied by side effects [171, 172, 190–192].

3. Concerning compatibilization, one should not only vary the compatibilizer fraction, but also the mixing procedure, the block lengths of the compatibilizer, and the temperature profile of the processing. At the optimum the mixing and the initial temperature profile should result in a constant average compatibilizer density in the interfacial layer, sufficient block lengths should restrict further compatibilizer

motion away from the interfacial layer during service, and sufficiently short blocks should keep the mobility of the compatibilizer high enough to guarantee its homogeneous distribution in the interface, until it is finally locked into this region either by chemical reaction or by quenching to a low service temperature.

Chapter VIII

Summary and Future Works

"*The end of study should be to direct the mind towards the enunciation of sound and correct judgments on all matters that come before it.*"
... René Descartes

In-situ SAXS measurements. In-situ small angle X-ray scattering measurements during mechanical testing is a strong tool for constructing structure-property-relationship of polymers. The evolution of nanostructure can be monitored with sufficient precision to correlate it with macroscopic response of the sample. Even without any precise pre-knowledge about the nanostructure the 2-dimensional scattering data can be transformed into the real space resulting in a chord distribution function (CDF). The peak analysis of the CDF reveals abundant information about the size, shape and correlation of the nanostructural entities. Thus deformation and rupture of the multi-phase morphology (e.g. semi-crystalline stacks), strain-induced crystallization/melting, crazing and other nanostructural transitions can be monitored. These information are vital when designing multi-phase materials with tailored properties is aimed at. In addition, the local nanoscopic strain can be estimated. Such quantitative experimental data combined with theory can improve our ability of simulating the mechanical behavior of multi-phase polymer materials [193–195].

Fatigue test at a synchrotron. Presently the minimum X-ray exposure required to record good anisotropic scattering patterns is still too long to monitor practical fatigue tests. With advanced technique and respective synchrotron beamlines this will become possible in the future. Nevertheless, as we have tried to demonstrate, even slow load-cycling experiments can shed some light on the mechanisms of structure response of polymeric composites under dynamic load.

General nanoscopic deformation mechanisms. Figure 8.1 summarizes and compares the deformation mechanisms in high-ordered and low-ordered (distorted) materials. Peak analysis of the CDF (SAXS) only probes the part of the matrix volume that is filled by a multi-phase domain structure (e.g. semi-crystalline stacks) with a minimum arrangement among their constituent domains (multilayer sandwiches marked by a broken rectangle in Figure 8.1). Random placement of irregular domains (gray domains in Figure 8.1) does not generate discrete SAXS peaks. Materials such as HDPE and PP form high-ordered semi-crystalline stacks in which several extended crystallites are piled up. This structure exhibits narrow layer-line peaks in the SAXS pattern, and accordingly several distinct peaks with in the CDF. During stretching, the peaks of CDF only move upward without becoming skewed. This indicates affine deformation of the semi-crystalline stacks. Thus variations of the L-peak's maximum measures the *average* deformation of the semi-crystalline morphology. This is different in materials with a heterogeneous or distorted nanostructure such as TPU or PP/MMT, respectively. The SAXS pattern of these materials exhibits an additional background. Their CDF peaks are diffuse and skewed. This indicates a broad distribution of long periods. Shape analysis of the asymmetric L-peak shows that the deformation is non-affine. In other words, the nanoscopic deformation of the stacks (layers) increases with their thickness. Therefore, the L-peak maximum does not measure the *average* deformation of the semi-crystalline morphology but only the deformation of the most frequent correlated stacks (most probable long period). Interestingly, in both kind of materials the nanoscopic strain computed from the variations of the L-peak maximum is always smaller than the macroscopic strain. This indicates that the most frequent well-correlated semi-crystalline stacks (domains) are stronger and deform less than the rest of the material. Thus the $\varepsilon_n/\varepsilon$ ratio can be considered as an index for nanoscopic strain-heterogeneity. This index is especially useful for following the failure mechanisms during a load-cycling test.

Material design. Concerning the material design the results of this work can be summarized as follows:

1. Strong TPU materials can be obtained if the melt processing is per-

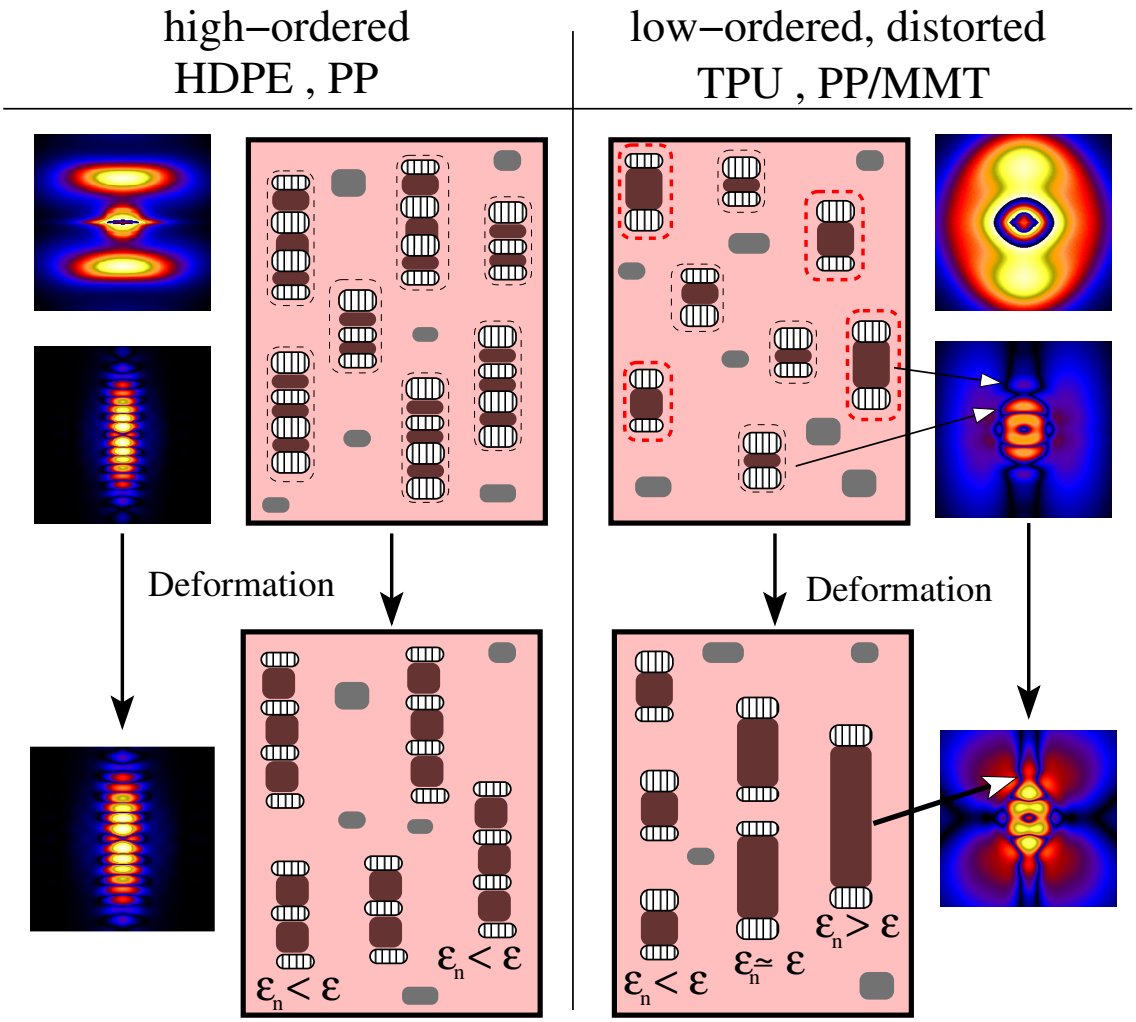

Figure 8.1: Schematic comparison of deformation mechanisms in high-ordered and low-ordered materials. SAXS monitors only the correlated domains marked with broken rectangles. The stacks marked by red rectangles contribute to the tail of the long period distribution. The disperse domains marked as gray regions do not contribute to the discrete SAXS peaks. High-ordered materials show several distinct peaks in their CDF whereas the low-ordered materials show diffuse peaks. The nanoscopic response of the material to the mechanical load is monitored by tracking the position and shape of *L*-peaks of CDFs.

formed below the phase-mixing temperature. Thus the phase-separated morphology is partially preserved. The domains will be oriented under shear flow and will grow upon cooling the melt. This results in an oriented material with mature hard domains.

2. In general, the influences of the additives in a composite on the expression of the semi-crystalline morphology of the matrix polymer are rarely taken into account. In situ monitoring by means of small-angle X-ray scattering has shown that additives may vary the nanostructure at least of polypropylene considerably. Thus re-optimization of commercial recipes might be required in order to tune the crystallization kinetics of the polymer in the presence of nanoparticles.

3. Low-molecular weight compatibilizers added to polymer composites may soften the matrix polymer. Matrix softening may enhance due to the migration of the compatibilizer during the course of load-cycling. Thus in addition to the chemical nature, the length and mobility of the compatibilizer must be taken into account. The problem of migration could possibly be solved by fixing the compatibilizer molecules at the interface by chemical bonds.

Suggestions for future work:

1. Combined heating-stretching cycles to study shape-memory behavior of TPU materials

2. Simultaneous SAXS-tomography during uniaxial deformation to investigate the effect of core-skin structures on the mechanical behavior

3. Simulation of the mechanical behavior of multi-phase polymer materials based on the experimental nanoscopic parameters extracted from CDFs

4. Investigation of nanoscopic strain-heterogeneity as a function of lamellae thickness

Bibliography

[1] Golfman, Y., *Hybrid Anisotropic Materials for Structural Aviation Parts*, CRC Press, Boca Raton, 2011, 1 edition.

[2] Kickelbick, G., *Hybrid Materials*, WILEY-VCH, Weinheim, 2007, 1 edition.

[3] Edwards, K. L., "Strategic Substitution of New Materials for Old: Applications in Automotive Product Development," *Mater. Des.* **2004**, 25, 529–533.

[4] Sperling, L. H., *Introduction to Physical Polymer Science*, John Wiley 'I&' Sons Ltd, New Jeresy, 2006, 4 edition.

[5] Gedde, U. W., *Polymer Physics*, Kluwer, Dordrecht, 1995.

[6] Eisenberg, A., "The Multi-Dimensional Glass Transition," *J. Phys. Chem.* **1963**, 67, 1333–1336.

[7] Strobl, G., *The Physics of Polymers*, Springer, Berlin, 2007.

[8] Granasy, L.; Pusztai, T.; Tegze, G.; Warren, J. A.; Douglas, J. F., "Growth and Form of Spherulites," *Phys. Rev. E* **2005**, 72, 011605.

[9] Weiner, J.; Berman, D. H., "Thermomechanical Behavior of Interacting Tie Molecules in Semicrystalline Polymers," *Macromolecules* **1984**, 17, 2015–2018.

[10] Huang, Y. L.; Brown, N., "Dependence of Slow Crack Growth in Polyethylene on Butyl Branch Density: Morphology and Theory," *J. Polym. Sci. Part B: Polym. Phys.* **1991**, 29, 129–137.

[11] Humbert, S.; Lame, O.; Chenal, J.-M.; Rochas, C.; Vigier, G., "Small Strain Behavior of Polyethylene: In situ SAXS Measurements," *J. Polym. Sci. Part B: Polym. Phys.* **2010**, 48, 1535–1542.

[12] Humbert, S.; Lame, O.; Chenal, J. M.; Rochas, C.; Vigier, G., "New Insight on Initiation of Cavitation in Semicrystalline Polymers: In-Situ SAXS Measurements," *Macromolecules* **2010**, 43, 7212–7221.

[13] Chen, B.; Evans, J. R. G., "Impact strength of polymer-clay nanocomposites," *Soft Matter,* **2009**, 5, 3572–3584.

[14] Oh, H.; Green, P. F., "Polymer Chain Dynamics and Glass Transition in Athermal Polymer/Nanoparticle Mixtures," *Nature Mater.* **2009**, 8, 139–143.

[15] Ginzburg, V. V.; Singh, C.; Balazs, A. C., "Theoretical Phase Diagrams of Polymer/Clay Composites:The Role of Grafted Organic Modifiers," *Macromolecules* **2000**, 33, 1089–1099.

[16] Janssen, R. P. M.; de Kanter, D.; Govaert, L. E.; Meijer, H. E. H., "Fatigue Life Predictions for Glassy Polymers: A Constitutive Approach," *Macromolecules* **2008**, 41, 2520–2530.

[17] Sauer, J. A.; Richardson, G. C., "Fatigue of Polymers," *Int. J. Fract.* **1980**, 16, 499–532.

[18] Pegoretti, A., "Creep and Fatigue Behavior of Polymer Nanocomposites," in "Nano- and Micro-Mechanics of Polymer Blends and Composites," , Karger-Kocsis, J.; Fakirov, S., eds., Hanser, Munich, 2009 pp. 301–339.

[19] Machado, G.; Kinast, E. J.; Scholten, J. D.; Thompson, A.; De Vargas, T.; Teixeira, S. R.; Samios, D., "Morphological and Crystalline Studies of Isotactic Polypropylene Plastically Deformed and Evaluated by Small-Angle X-ray Scattering, Scanning Electron Microscopy and X-ray Diffraction," *Eur. Polym. J.* **2009**, 45, 700–713.

[20] He, C.; Donald, A. M., "Morphology of a Deformed Rubber Toughened Poly(methyl methacrylate) Film Under Tensile Strain," *J. Mater. Sci.* **1997**, 32, 5661–5667.

[21] Ariyama, T., "Cyclic Deformation Behaviour and Morphology of Polypropylene," *J. Mater. Sci.* **1993**, 28, 3845–3850.

[22] Xu, B.; Leisen, J.; Beckham, H. W.; Abu-Zurayk, R.; Harkin-Jones, E.; McNally, T., "Evolution of Clay Morphology in Polypropylene/Montmorillonite Nanocomposites upon Equibiaxial Stretching: A Solid-State NMR and TEM Approach," *Macromolecules* **2009**, 42, 8959–8968.

[23] Castelein, G.; Coulon, G.; G'seil, C., "Polymers Under Mechanical Stress: Deformation of the Nanostructure of lsotactic Polypropylene Revealed by Scanning Force Microscopy," *Polym. Eng. Sci.* **1997**, 37, 1694–1701.

[24] Thomas, C.; Seguela, R.; Detrez, F.; Miri, V.; Vanmansart, C., "Plastic Deformation of Spherulitic Semi-Crystalline Polymers: An in-situ AFM Study of Polybutene Under Tensile Drawing," *Polymer* **2009**, 50, 3714–3723.

[25] Gilbert, D. G.; Donald, A. M., "Toughening Mechanisms in High Impact Polystyrene," *J. Mater. Sci.* **1986**, 21, 1819–1823.

[26] Danilatos, G. D., "Bibliography of Environmental Scanning Electron Microscopy," *Microsc. Res. Tech.* **1993**, 25, 529–534.

[27] Zankel, A.; Poelt, P.; Gahleitner, M.; Ingolic, E.; Grein, C., "Tensile Tests of Polymers at Low Temperatures in the Environmental Scanning Electron Microscope: An Improved Cooling Platform," *Scanning* **2007**, 29, 261–269.

[28] Nase, M.; Zankel, A.; Langer, B.; Baumann, H. J.; Grellmann, W.; Poelt, P., "Investigation of the Peel Behavior of Polyethylene/Polybutene-1 Peel

Films Using in-situ Peel Tests With Environmental Scanning Electron Microscopy," *Polymer* **2008**, 49, 5458–5466.

[29] Poelt, P.; Zankel, A.; Gahleitner, M.; Ingolic, E.; Grein, C., "Tensile Tests in the Environmental Scanning Electron Microscope (ESEM) Part I: Polypropylene Homopolymers," *Polymer* **2010**, 51, 3203–3212.

[30] Rask, J. H.; Flood, J. E.; Borchardt, J. K.; York, G. A., "The ESEM Used to Image Crystalline Structures of Polymers and to Image Ink on Paper," *Microsc. Res. Tech.* **1993**, 25, 384–392.

[31] Nozue, Y.; Shinohara, Y.; Ogawa, Y.; Sakurai, T.; Hori, H.; Kasahara; Tatsuya; Yamaguchi, N.; Yagi, N.; Amemiya, Y., "Deformation Behavior of Isotactic Polypropylene Spherulite during Hot Drawing Investigated by Simultaneous Microbeam SAXS-WAXS and POM Measurement," *Macromolecules* **2007**, 40, 2036–2045.

[32] Ube, T.; Aoki, H.; Ito, S.; Horinaka, J. I.; Takigawa, T., "Affine Deformation of Single Polymer Chain in Poly(methyl methacrylate) Films Under Uniaxial Extension Observed by Scanning Near-Field Optical Microscopy," *Polymer* **2009**, 50, 3016–3021.

[33] Litvinov, V. M.; Xu, J.; Melian, C.; Demco, D. E.; Möller, M.; Simmelink, J., "Morphology, Chain Dynamics, and Domain Sizes in Highly Drawn Gel-Spun Ultrahigh Molecular Weight Polyethylene Fibers at the Final Stages of Drawing by SAXS, WAXS, and 1H Solid-State NMR," *Macromolecules* **2011**, 44, 9254–9266.

[34] Huy, T. A.; Adhikari, R.; Lüpke, T.; Henning, S.; Michler, G. H., "Molecular Deformation Mechanisms of Isotactic Polypropylene in α- and β- Crystal Forms by FTIR Spectroscopy," *J. Polym. Sci. Part B: Polym. Phys.* **2004**, 42, 4478–4488.

[35] Song, Y.; Nitta, K. H.; Nemoto, N., "Molecular Orientations and True Stress-Strain Relationship in Isotactic Polypropylene Film," *Macromolecules* **2003**, 36, 8066–8073.

[36] Yoshida, S.; Ishii, K.; Kawamura, T.; Nitta, K. H., "Molecular Orientation Behavior of Mesomorphic Isotactic Polypropylene Under Uniaxial and Biaxial Deformation," *Polym. Eng. Sci.* **2011**, 51, 225–231.

[37] Farbos, B.; Mauran, D.; Pellerin, C., "Time-Resolved Polymer Deformation Using Polarized Planar Array Infrared Spectroscopy," *Vib. Spectrosc.* **2009**, 51, 34–38.

[38] Tarantili, P. A.; Andreopoulos, A. G.; Galiotis, C., "Real-Time Micro-Raman Measurements on Stressed Polyethylene Fibers. 1. Strain Rate Effects and Molecular Stress Redistribution," *Macromolecules* **1998**, 31, 6964–6976.

[39] Wang, S.; Wang, B.; Wang, B., "Investigation of Polymer Deformation by Positron Annihilation," *Journal de Physique IV 03* **1993**, C4, 275–278.

[40] Boué, "Transient Relaxation Mechanisms in Elongated Melts and Rubbers Investigated by Small Angle Neutron Scattering," *Adv Polym Sci* **1987**, 82, 47–101.

[41] Blaise, A.; Baravian, C.; André, S.; Dillet, J.; Michot, L. J.; Mokso, R., "Investigation of the Mesostructure of a Mechanically Deformed HDPE by Synchrotron Microtomography," *Macromolecules* **2010**, 43, 8143–8152.

[42] Stribeck, N., "X-ray Scattering for the Monitoring of Processes in Polymer Materials with Fiber Symmetry," *J. Macromol. Sci. Part C: Polymer Reviews* **2010**, 50, 40–58.

[43] Akpalu, Y. A., "Scattering from Polymers," *J. Macromol. Sci. Part C: Polymer Reviews* **2010**, 50, 1–13.

[44] Roe, R. J., *Methods of X-Ray and Neutron Scatteing in Polymer Science*, Oxford University Press, New York, 2000.

[45] Als-Nielsen, J.; McMorrow, D., *Elements of Modern X-ray Physics*, John Wiley & Sons, Ltd, Chichester, 2001, 1 edition.

[46] Stribeck, N., *X-Ray Scattering of Soft Matter*, Springer, Heidelberg, New York, 2007.

[47] Bragg, W. H.; Bragg, W. L., "The Reflection of X-rays by Crystals," *Proc. R. Soc. Lond. A* **1913**, 88, 428–438.

[48] Hiss, R.; Hobeika, S.; Lynn, C.; Strobl, G., "Network Stretching, Slip Processes, and Fragmentation of Crystallites during Uniaxial Drawing of Polyethylene and Related Copolymers. A Comparative Study," *Macromolecules* **1999**, 32, 4390–4403.

[49] Morosoff, N.; Petterlin, A., "Plastic Deformation of Polypropylene. IV. Wide-Angle X-Ray Scattering in the Neck Region," *J. Polym. Sci. Part A-2: Polym. Phys.* **1972**, 10, 1237–1254.

[50] Ran, S.; Zong, X.; Fang, D.; Hsiao, B. S.; Chu, B.; Phillips, R. A., "Structural and Morphological Studies of Isotactic Polypropylene Fibers During Heat/Draw Deformation by in-situ Synchrotron SAXS/WAXD," *Macromolecules* **2001**, 34, 2569–2578.

[51] Vaia, R. A.; Liu, W.; Koerner, H., "Analysis of Small-Angle Scattering of Suspensions of Organically Modified Montmorillonite: Implications to Phase Behavior of Polymer Nanocomposites," *J. Polym. Sci. Part B Polym. Phys.* **2003**, 41, 3214–3236.

[52] Baltá Calleja, F. J.; Petterlin, A.; Crist, B., "Plastic Deformation of Polypropylene VII. Long Period as Function of Temperature and Rate of Drawing," *J. Polym. Sci. Part A-2: Polym. Phys.* **1972**, 10, 1749–1756.

[53] Ren, C.; Jiang, Z.; Du, X.; Men, Y.; Tang, T., "Microstructure and Deformation Behavior of Polyethylene/Montmorillonite Nanocomposites with Strong Interfacial Interaction," *J. Phys. Chem. B* **2009**, 113, 14118–14127.

[54] Phillips, A.; Zhu, P. W.; Edward, G., "Simple Shear Deformation of Polypropylene via the Equal Channel Angular Extrusion Process," *Macromolecules* **2006**, 39, 5796–5803.

[55] Pawlak, A.; Galeski, A., "Cavitation during Tensile Deformation of Polypropylene," *Macromolecules* **2008**, 41, 2839–2851.

[56] Nitta, K. H.; Takayanagi, M., "Role of Tie Molecules in the Yielding Deformation of Isotactic Polypropylene," *J. Polym. Sci. Part B: Polym. Phys.* **1999**, 37, 357–368.

[57] Stribeck, N.; Almendarez Camarillo, A.; Nöchel, U.; Schroer, C.; Kuhlmann, M.; Roth, S. V.; Gehrke, R.; Bayer, R. K., "Volume-Resolved Nanostructure Survey of a Polymer Part by Means of SAXS Microtomography," *Macromol. Chem. Phys.* **2006**, 207, 1239–1249.

[58] Stribeck, N.; Nöchel, U.; Almendárez Camarillo, A., "Scanning Microbeam X-ray Scattering of Fibers Analyzed by one-Dimensional Tomography," *Macromol. Chem. Phys.* **2008**, 209, 1976–1982.

[59] Sakurai, S.; Yoshida, H.; Hashimoto, F.; Shibaya, M.; Ishihara, H.; Yoshihara, N.; Nishitsuji, S.; Takenaka, "Ultra Small-Angle X-ray Scattering Studies on Structural Changes in Micrometers Upon Uniaxial Stretching of Segmented Polyurethaneureas," *Polymer* **2009**, 50, 1566–1576.

[60] Stribeck, N., "Scattering of Soft Condensed Matter. From Fundaments to Application," in "Applications of Synchrotron Light to Scattering and Diffraction in Materials and Life Sciences," , Ezquerra, T. A.; Garciá Gutiérrez, M.; Nogales, A.; Gómez, M., eds., Springer, Berlin Heidelberg, 2009, volume 776 of *Lect. Notes Phys.* pp. 25–62.

[61] Debye, P.; Bueche, A. M., "Scattering by an Inhomogeneous Solid," *J. Appl. Phys.* **1949**, 20, 518–525.

[62] Porod, G., "The Small-Angle X-Ray Scattering from Densely Packed Colloidal Systems (Ger.)," *Colloid Polym. Sci.* **1951**, 124, 83–114.

[63] Stribeck, N., "Extraction of Domain Structure Information From Small-Angle X-Ray Patterns of Bulk Materials," *J. Appl. Cryst.* **2001**, 34, 496–503.

[64] Stribeck, N.; Fakirov, S., "Three-Dimensional chord Distribution Function SAXS Analysis of the Strained Domain Structure of a Poly(ether ester) Thermoplastic Elastomer," *Macromolecules* **2001**, 34, 7758–7761.

[65] Ruland, W., "The Evaluation of the Small-Angle Scattering of Lamellar Two-Phase Systems by Means of Interface Distribution Functions," *Colloid Polym. Sci.* **1977**, 255, 417–427.

[66] Ruland, W., "The Evaluation of the Small-Angle Scattering of Anisotropic Lamellar Two-Phase Systems by Means of Interface Distribution Functions," *Colloid Polym. Sci.* **1978**, 256, 932–936.

[67] Stribeck, N.; Ruland, W., "Determination of the Interface Distribution Function of Lamellar Two-Phase Systems," *J. Appl. Cryst.* **1978**, 11, 535–539.

[68] Méring, J.; Tchoubar-Vallat, D., "X-Rays. Small-Angle X-Ray Scattering in Diluted Suspensions. Computations of Chord Distributions (fr.)," *C. R. Acad. Sc. Paris* **1965**, 261, 3096–3099.

[69] Méring, J.; Tchoubar-Vallat, D., "Solid State Physics. Diffuse Small-Angle X-Ray Scattering from Concentrated Systems (fr.)," *C. R. Acad. Sc. Paris* **1966**, 262, 1703–1706.

[70] Méring, J.; Tchoubar, D., "Interpretation of the SAXS from Porous Systems. Part I. (french)," *J. Appl. Cryst.* **1968**, 1, 153–165.

[71] Tchoubar, D.; Méring, J., "Interpretation of the SAXS from Porous Systems. Part II. (french)," *J. Appl. Cryst.* **1969**, 2, 128–138.

[72] Ruland, W., "Small-Angle Scattering of Two-Phase Systems: Determination and Significance of Systematic Deviations from Porod's Law," *J. Appl. Cryst.* **1971**, 4, 70–73.

[73] Koberstein, J. T.; Morra, B.; Stein, R. S., "The Determination of Diffuse-Boundary Thicknesses of Polymers by Small-Angle X-ray Scattering," *J. Appl. Cryst.* **1980**, 13, 34–45.

[74] Stribeck, N., "Nanostructure Evolution Studies of Bulk Polymer Materials with Synchrotron Radiation. Progress in Method Development," *Anal. Bioanal. Chem.* **2003**, 376, 608–617.

[75] Stribeck, N.; Nöchel, U.; Funari, S. S.; Schubert, T., "Tensile Tests of Polypropylene Monitored by SAXS. Comparing the Stretch-Hold Technique to the Dynamic Technique," *J. Polym. Sci. Polym. Phys.* **2008**, 46, 721–726.

[76] Denchev, Z.; Dencheva, N.; Funari, S. S.; Motovilin, M.; Schubert, T.; Stribeck, N., "Nanostructure and Mechanical Properties Studied During Dynamical Straining of Microfibrillar Reinforced HDPE/PA Blends," *J. Polym. Sci. Part B: Polym. Phys.* **2010**, 48, 237–250.

[77] Jankova, K.; Chen, X.; Kops, J.; Batsberg, W., "Synthesis of Amphiphilic PS-b-PEG-b-PS by Atom Transfer Radical Polymerization," *Macromolecules* **1998**, 31, 538–541.

[78] Jankova, K.; Kops, J.; Chen, X.; Batsberg, W., "Synthesis by ATRP of Poly(ethylene-co-butylene)-blockpolystyrene, Poly(ethylene-co-butylene)-block-poly(4-acetoxystyrene) and its Hydrolysis Product Poly(ethylene-cobutylene)-block-poly(hydroxystyrene)," *Macromol. Rapid Commun.* **1999**, 20, 219–223.

[79] Denchev, Z. Z.; Dencheva, N. V., "Transforming Polymer Blends into Composites: a Pathway Towards Nanostructured Materials," *Polym. Inter.* **2008**, 57, 11–22.

[80] Dencheva, N.; Oliveira, M. J.; Carneiro, O. S.; Pouzada, A. S.; Denchev, Z., "Preparation and Structure Development in Microfibrilar Composite Materials Based on Polyethylene-Polyamide 6 Oriented Blends," *J. Appl. Polym. Sci.* **2010**, 115, 2918–2932.

[81] VNI, "PV-WAVE manuals," V 7.5, Houston, TX, USA **2007**.

[82] Stribeck, N.; Nöchel, U., "A Method for Merging of USAXS and Smeared SAXS Patterns of Fibers," *J. Appl. Cryst.* **2008**, 41, 715–722.

[83] Hugel, T.; Strobl, G.; Thomann, R., "Building Lamellae from Blocks: The Pathway Followed in the Formation of Crystallites of Syndiotactic Polypropylene," *Acta Polym.* **1999**, 50, 214–217.

[84] Strobl, G., "Crystallization and melting of bulk polymers: New observations, conclusions and a thermodynamic scheme," *Progr. Polym. Sci.* **2006**, 31, 398–442.

[85] Hall, E. L., *Computer Image Processing and Recognition*, Academic Press, London, 1980.

[86] Jánosi, A., "Small-Angle X-ray Scattering from Multiphase Systems. Interpretation of the Electron Density Fluctuation (Ger.)," *Monatsh. f. Chemie* **1983**, 114, 377–383.

[87] Glatter, O.; Kratky, O., eds., *Small Angle X-ray Scattering*, Academic Press, London, 1982.

[88] Baltá Calleja, F. J.; Vonk, C. G., *X-Ray Scattering of Synthetic Polymers*, Elsevier, Amsterdam, 1989.

[89] Bonart, R., "Segmentierte Polyurethane," *Angew. Makromol. Chem.* **1977**, 58, 259–297.

[90] Ryan, A. J.; Elwell, M. J.; Bras, W., "Using Synchrotron Radiation to Study Polymer Processing," *Nuclear Instr. Meth. Phys. Res.* **1995**, B97, 216–223.

[91] Pompe, G.; Pohlers, A.; Pötschke, P.; Pionteck, J., "Influence of Processing Conditions on the Multiphase Structure of Segmented Polyurethane," *Polymer* **1998**, 39, 5147–5153.

[92] Frick, A.; Rochman, A., "Characterization of TPU-Elastomers by Thermal Analysis (DSC)," *Polymer Testing* **2004**, 23, 413–417.

[93] Frick, A.; Mikoszek, M., "Study on the Influence of Melt Processing on Segmented Polyurethanes Morphology," *Macromol.Symp.* **2010**, 294, 102–108.

[94] Sonnenschein, M. F.; Lysenko, Z.; Brune, D. A.; Wendt, B. L.; Schrock, A. K., "Enhancing Polyurethane Properties via Soft Segment Crystallization," *Polymer* **2005**, 46, 10158–10166.

[95] Saiani, A.; Daunch, W. A.; Verbeke, H.; Leenslag, J. W.; Higgins, J. S., "Origin of Multiple Melting Endotherms in a High Hard Block Content Polyurethane. 1. Thermodynamic Investigation," *Macromolecules* **2001**, 34, 9059–9068.

[96] Pötschke, P.; Häußler, L.; Pegel, S.; Steinberger, R.; Scholz, G., "Thermoplastic Polyurethane Filled with Carbon Nanotubes for Electrical Dissipative and Conductive Applications," *Kautschuk Gummi Kunststoffe* **2007**, 60, 432–437.

[97] Eisenbach, C. D.; Nefzger, H.; Hayen, H.; Enkelmann, V., "Structure of the Hard Segments in non Hydrogen Bond Forming Polyurethane Elastomers as Derived from Oligomeric Model Compounds," *Macromol. Chem. Phys.* **1994**, 195, 3325–3342.

[98] Peterlin, A., "Molecular Model of Drawing Polyethylene and Polypropylene," *J. Mater. Sci.* **1971**, 6, 490–508.

[99] Peterlin, A., "Morphology and Properties of Crystalline Polymers with Fiber Structure," *Text. Res. J.* **1972**, 42, 20–30.

[100] Porod, G., "Application and Results of Small-Angle X-Ray Scattering from Solid Polymers (Ger.)," *Fortschr. Hochpolym.-Forsch.* **1961**, 2, 363–400.

[101] Bonart, R., "X-ray Investigations Concerning the Physical Structure of Cross-linking in Segmented Urethane Elastomers," *J. Macromol. Sci. Part B* **1968**, 2, 115–138.

[102] Hoffmann, K.; Bonart, R., "Orientierungsverhalten von segmentierten Polyetherurethanen in Abhängigkeit von der Dehnung und den verwendeten Lösungsmitteln," *Makromol. Chem.* **1983**, 184, 1529–1546.

[103] Varga, J., "Crystallization, Melting and Supermolecular Structure of Isotactic Polypropylene," in "Polypropylene: Structure, Blends and Composites," , Karger-Kocsis, J., ed., Chapman & Hall, London, 1995 pp. 51–106.

[104] Kurokawa, Y.; Yasuda, H.; Oya, A., "Preparation of a Nanocomposite of Polypropylene and Smectite," *J. Mater. Sci. Lett.* **1996**, 15, 1481–1483.

[105] Giannelis, E. P., "Polymer Layered Silicate Nanocomposites," *Adv. Mater.* **1996**, 8, 29–35.

[106] Manias, E.; Touny, A.; Wu, L.; Strawhecker, K. E.; Lu, B.; Chung, T. C., "Polypropylene/Montmorillonite Nanocomposites. Review of the Synthetic Routes and Materials Properties," *Chem. Mater.* **2001**, 13, 3516–3523.

[107] Ray, S. S.; Okamoto, M., "Polymer/Layered Silicate Nanocomposites: A Review from Preparation to Processing," *Prog. Polym. Sci.* **2003**, 28, 1539–1641.

[108] Solomon, M. J.; Somwangthanaroj, A., "Intercalated Polypropylene Nanocomposites," in "Dekker Encyclopedia of Nanoscience and Nanotechnology," , Schwarz, J. A.; Contescu, C. I.; Putyera, K., eds., Marcel Dekker, Inc., New York, 2004 pp. 1483–1490.

[109] Ke, Y. C.; Stroeve, P., *Polymer-Layered Silicates and Silica Nanocomposites*, Elsevier, Amsterdam, 2005, 1 edition.

[110] Ma, J.; Qi, Z.; Hu, Y., "Synthesis and Characterization of Polypropylene/Clay Nanocomposites," *J. Appl. Polym. Sci.* **2001**, 82, 3611–3617.

[111] Kawasumi, M.; Hasegawa, N.; Kato, M.; Usuki, A.; Okada, A., "Preparation and Mechanical Properties of Polypropylene-Clay Hybrids," *Macromolecules* **1997**, 30, 6333–6338.

[112] Hambir, S.; Bulakh, N.; Kodgire, P.; Kalgaonkar, R.; Jog, J. P., "PP/Clay Nanocomposites: A Study of Crystallization and Dynamic Mechanical Behavior," *J. Polym. Sci. Part B: Polym. Phys.* **2001**, 39, 446–450.

[113] Vu, Y. T.; Rajan, G. S.; Mark, J. E., "Reinforcement of Elastomeric Polypropylene by Nanoclay Fillers," *Polym. Int.* **2004**, 53, 1071–1077.

[114] Chen, L.; Wong, S. C.; Liu, T.; Lu, X.; He, C., "Deformation Mechanisms of Nanoclay-Reinforced Maleic Anhydride-Modified Polypropylene," *J. Polym. Sci. Part B: Polym. Phys.* **2000**, 49, 1561–1564.

[115] Zhang, Q.; Fu, Q.; Jiang, L.; Lei, Y., "Preparation and Properties of Polypropylene/Montmorillonite Layered Nanocomposites," *Polym. Int.* **2000**, 49, 1561–1564.

[116] Zhu, S.; Chen, J.; Zuo, Y.; Li, H.; Cao, Y., "Montmorillonite/Polypropylene Nanocomposites: Mechanical Properties, Crystallization and Rheological Behaviors," *Appl. Clay Sci.* **2011**, 52, 171–178.

[117] Prachum, Y.; Strauss, R. H. A.; Zuo, Y.; Kiatkamjornwong, S., "The Physical and Mechanical Properties of Beta-Nucleated Polypropylene/Montmorillonite Nanocomposites," *J. Appl. Polym. Sci.* **2011**, 122, 1066–1076.

[118] Pavlidou, S.; Papaspyrides, C. D., "A Review on Polymer-Layered Silicate Nanocomposites," *Prog. Polym. Sci.* **2008**, 33, 1119–1198.

[119] LeBaron, P. C.; Wang, Z.; Pinnavaia, T. J., "Polymer-layered silicate nanocomposites: an overview," *Appl. Clay Sci.* **1999**, 15, 11–19.

[120] Chrissopoulou, K.; Anastasiadis, S. H., "Polyolefin/Layered Silicate Nanocomposites with Functional Compatibilizers," *Eur. Polym. J.* **2011**, 47, 600–613.

[121] Reichert, P.; Nitz, H.; Klinke, S.; Brandsch, R.; Thomann, R.; Mülhaupt, R., "Poly(propylene)/Organoclay Nanocomposite Formation:Influence of

Compatibilizer Functionality and Organoclay Modification," *Macromol. Mater. Eng.* **2000**, 275, 8–17.

[122] Spencer, M. W.; Hunter, D. L.; Knesek, B. W.; Paul, D. R., "Morphology and Properties of Polypropylene Nanocomposites Based on a Silanized Organoclay," *Polymer* **2011**, 52, 5369–5377.

[123] Rohlmann, C. O.; Horst, M. F.; Quinzani, L. M.; Failla, M. D., "Comparative Analysis of Nanocomposites Based on Polypropylene and different Montmorillonites," *Eur. Polym. J.* **2008**, 44, 2749–2760.

[124] Lertwimolnun, W.; Vergnes, B., "Influence of Compatibilizer and Processing Conditions on the Dispersion of Nanoclay in a Polypropylene Matrix," *Polymer* **2005**, 46, 3462–3471.

[125] Ratnayake, U. N.; Haworth, B., "Polypropylene/Clay Nanocomposites: Influence of Low Molecular Weight Polar Additives on Intercalation and Exfoliation Behavior," *Polym. Eng. Sci.* **2006**, 46, 1008–1015.

[126] Lee, E. C.; Mielewski, D. F.; Baird, R. J., "Exfoliation and dispersion Enhancement in Polypropylene Nanocomposites by in-situ Melt Phase Ultrasonication," *Polym. Eng. Sci.* **2004**, 44, 1773–1782.

[127] Chen, Y. H.; Zhong, G. J.; Wang, Y.; Li, Z. M.; Li, L., "Unusual Tuning of Mechanical Properties of Isotactic Polypropylene Using Counteraction of Shear Flow and β-Nucleating Agent on β-Form Nucleation," *Macromolecules* **2009**, 42, 4343–4348.

[128] Zhao, L.; Li, J.; Guo, S.; Du, Q., "Ultrasonic Oscillations Induced Morphology and Property Development of Polypropylene/Montmorillonite Nanocomposites," *Polymer* **2006**, 47, 2460–2469.

[129] Morgan, A. B.; Gilman, J. W., "Characterization of Polymer-Layered Silicate (Clay) Nanocomposites by Transmission Electron Microscopy and X-Ray Diffraction: A Comparative Study," *J. Appl. Polym. Sci.* **2003**, 87, 1329–1338.

[130] Vermogen, A.; Masenelli-Varlot, K.; Séguéla, R.; Duchet-Rumeau, J.; Boucard, S.; Prele, P., "Evaluation of the Structure and Dispersion in Polymer-Layered Silicate Nanocomposites," *Macromolecules* **2005**, 38, 9661–9669.

[131] Martín, Z.; Jiménez, I.; Ángeles Gómez, M.; Ade, H.; Kilcoyne, D. A.; Hernádez-Cruz, D., "Spectromicroscopy Study of Intercalation and Exfoliation in Polypropylene/Montmorillonite Nanocomposites," *J. Phys. Chem. B* **2009**, 113, 11160–11165.

[132] Ma, J.; Zhang, S.; Qi, Z.; Li, G.; Hu, Y., "Crystallization Behaviors of Polypropylene/Montmorillonite Nanocomposites," *J. Appl. Polym. Sci.* **2001**, 83, 1978–1985.

[133] Xu, W.; Ge, M.; He, P., "Nonisothermal Crystallization Kinetics of Polypropylene/Montmorillonite Nanocomposites," *J. Polym. Sci. Part B: Polym. Phys.* **2002**, 40, 408–414.

[134] Pozsgay, A.; Fráter, T.; Papp, L.; Sajó, I.; Pukánszky, B., "Nucleating Effect of Montmorillonite Nanoparticles in Polypropylene," *J. Macromol. Sci., Part B: Physics* **2002**, 41, 1249–1265.

[135] Li, J.; Zhou, C.; Gang; Wang, "Study on Nonisothermal Crystallization of Maleic Anhydride Grafted Polypropylene/Montmorillonite Nanocomposite," *Polymer Testing* **2003**, 22, 217–223.

[136] Xu, W.; Liang; Guodong; Zhai, H.; Tang, S.; Hang, G.; Pan, W.-P., "Preparation and Crystallization Behaviour of PP/PP-g-MAH/Org-MMT Nanocomposite," *Eur. Polym. J.* **2003**, 39, 1467–1474.

[137] Kim, B.; Lee, S. H.; Lee, D.; Ha, B.; Park, J.; Char, K., "Crystallization Kinetics of Maleated Polypropylene/Clay Hybrids," *Ind. Eng. Chem. Res.* **2004**, 43, 6082–6089.

[138] Nowacki, R.; Monasse, B.; Piorkowska, E.; Galeski, A.; M., H. J., "Spherulite Nucleation in Isotactic Polypropylene Based Nanocomposites with Montmorillonite under Shear," *Polymer* **2004**, 45, 4877–4892.

[139] Ding, C.; Jia, D.; He, H.; Guo, B.; Hong, H., "How Organo-Montmorillonite truly Affects the Structure and Properties of Polypropylene," *Polymer Testing* **2005**, 24, 94–100.

[140] Rozanski, A.; Monasse, B.; Szkudlarek, E.; Pawlak, A.; Piorkowska, E.; Galeski, A.; Haudin, J. M., "Shear-Induced Crystallization of Isotactic Polypropylene Based Nanocomposites with Montmorillonite," *Eur. Polym. J.* **2009**, 45, 88–101.

[141] Brown, H. R.; Kramer, E. J., "Craze Microstructure from Small-Angle X-Ray Scattering (SAXS)," *J. Macromol. Sci. Part B: Physics* **1981**, 19, 487–522.

[142] Brown, H. R.; Kramer, E. J.; Bubeck, R. A., "Effect of Deformation Ratio on Fibril Deformation in Fatigue of Polystyrene," *J. Mater. Sci.* **1988**, 23, 248–252.

[143] Karl, A.; Cunis, S.; Gehrke, R.; Krosigk, G. v.; Lode, U.; Luzinov, I.; Minko, S.; Pomper, T.; Senkovsky, V.; Voronov, A.; Wilke, W., "Investigation of failure mechanisms in polymer composites by simultaneous measurement of ultra-small-angle scattering and acoustic emission during the deformation. I. Method," *J. Macromol. Sci. Part B: Physics* **1999**, 38, 901–912.

[144] Pomper, T.; Lode, U.; Karl, A.; Krosigk, G. V.; Minko, S.; Luzinov, I.; Senkovsky, V.; Voronov, A.; Wilke, W., "Investigation of Craze Development Using Small-Angle X-Ray Scattering of Synchrotron Radiation," *J. Macromol. Sci., Phys.* **1999**, B38, 869–883.

[145] Kobayashi, H.; Shioya, M.; Tanaka, T.; Irisawa, T., "Synchrotron Radiation Small-Angle X-Ray Scattering Study on Fracture Process of Carbon Nanotube/Poly(ethylene terephthalate) Composite Films," *Compos. Sci. Technol.* **2007**, 67, 3209–3218.

[146] Fischer, S.; Diesner, T.; Rieger, B.; Marti, O., "Simulating and Evaluating Small-Angle X-Ray Scattering of Micro-Voids in Polypropylene during Mechanical Deformation," *J. Appl. Cryst.* **2010**, 43, 603–610.

[147] Statton, W. O., "Microvoids in Fibers as Studied by Small-Angle Scattering of X-rays," *J. Polym. Sci.* **1962**, 58, 205–220.

[148] Stribeck, N.; Nöchel, U.; Funari, S. S.; Schubert, T.; Timmann, A., "Nanostructure Evolution in Polypropylene During Mechanical Testing," *Macromol. Chem. Phys.* **2008**, 209, 1992–2002.

[149] Stribeck, N.; Androsch, R.; Funari, S. S., "Nanostructure Evolution of Homogeneous Poly(ethylene-co-1-octene) as a Function of Strain," *Macromol. Chem. Phys.* **2003**, 204, 1202–1216.

[150] Fronk, W.; Wilke, W., "SAXS of Partially Oriented Polymers: Model Calculations with Monoclinic Macrolattice," *Colloid Polym. Sci.* **1985**, 263, 97–108.

[151] Fakirov, S.; Samokovlijsky, O.; Stribeck, N.; Apostolov, A. A.; Denchev, Z.; Sapoundjieva, D.; Evstatiev, M.; Meyer, A.; Stamm, M., "Nanostructure Deformation Behavior in Poly(ethylene terephthalate)/ Polyethylene Drawn blend as Revealed by Small-Angle Scattering of Synchrotron X Radiation," *Macromolecules* **2001**, 34, 3314–3317.

[152] Androsch, R.; Stribeck, N.; Lüpke, T.; Funari, S., "Investigation of the Deformation of Homogeneous Poly(ethylene-co-1-octene) by Wide- and Small-angle X-ray Scattering using Synchrotron Radiation," *J. Polym. Sci. Part B: Polym. Phys.* **2002**, 40, 1919–1930.

[153] Moonen, J. A.; Roovers, W. A.; Meier, R. J.; Kip, B. J., "Crystal and Molecular Deformation in Strained High-Performance Polyethylene Fibers Studied by Wide-Angle X-ray Scattering and Raman Spectroscopy," *J. Polym. Sci. Part B: Polym. Phys.* **1992**, 30, 361–372.

[154] Wilkes, G. L.; Zhou, H., "Orientation-Dependent Mechanical Properties and Deformation Morphologies for Uniaxially Melt-Extruded High-Density Polyethylene Films having an Initial Stacked Lamellar Texture," *J. Mater. Sci.* **1998**, 33, 287–303.

[155] Butler, M. F.; Donald, A. M., "A Real-Time Simultaneous Small- and Wide-angle X-Ray Scattering Study of in situ Polyethylene Deformation at Elevated Temperatures," *Macromolecules* **1998**, 31, 6234–6249.

[156] Wu, J.; Schultz, J. M.; Yeh, F.; Hsiao, B. S.; Chu, B., "In-Situ Simultaneous Synchrotron Small- and Wide-Angle X-ray Scattering Measurement of Poly(vinylidene fluoride) Fibers under Deformation," *Macromolecules* **2000**, 33, 1765–1777.

[157] Barbi, V.; Funari, S. S.; Gehrke, R.; Scharnagl, N.; Stribeck, N., "SAXS and the Gas Transport in Polyether-block-Polyamide Copolymer Membranes," *Macromolecules* **2003**, 38, 749–758.

[158] Kawakami, D.; Ran, S.; Burger, C.; Avila Orta, C.; Sics, I.; Chu, B.; Hsiao, B. S.; Kikutani, T., "Superstructure Evolution in Poly(ethylene terephthalate) during Uniaxial Deformation above Glass Transition Temperature," *Macromolecules* **2006**, 39, 2909–2920.

[159] Miyazaki, T.; Hoshiko, A.; Akasaka, M.; Shintani, T.; Sakurai, S., "SAXS Studies on Structural Changes in a Poly(vinyl alcohol) Film during Uniaxial Stretching in Water," *Macromolecules* **2006**, 39, 2921–2929.

[160] Ibanes, C.; David, L.; de Boissieu, M.; Séguéla, R.; Epicier, T.; Robert, G., "Structure and Mechanical Behavior of Nylon-6 Fibers Filled with Organic and Mineral Nanoparticles. I. Microstructure of Spun and Drawn Fibers," *J. Polym. Sci. Part B: Polym. Phys.* **2004**, 42, 3876–3892.

[161] Šmit, I.; Musil, V.; Švab, I., "Effects of EPDM and Wollastonite on Structure of Isotactic Polypropylene Blends and Composites," *J. Appl. Polym. Sci.* **2004**, 91, 4072–4081.

[162] Todorov, L. V.; Viana, J. C., “Characterization of PET Nanocomposites Produced by Different Melt-Based Production Methods,” *J. Appl. Polym. Sci.* **2007**, 106, 1659–1669.

[163] Deshmane, C.; Yuan, Q.; Perkins, R. S.; Misra, R. D. K., “On striking Variation in Impact Toughness of Polyethylene-Clay and Polypropylene-Clay Nanocomposite Systems: The Effect of Clay-Polymer Interaction,” *Mater. Sci. Eng. A* **2007**, 458, 150–157.

[164] Drozdov, A. D.; Christiansen, J. d., “Cyclic Viscoplasticity of High-Density Polyethylene/Montmorillonite Clay Nanocomposite,” *Eur. Polym. J.* **2007**, 43, 10–25.

[165] Blomenhofer, M.; Ganzleben, S.; Hanft, D.; Schmidt, H.-W.; Kristiansen, M.; Smith, P.; Stoll, K.; Mäder, D.; Hoffmann, K., “"Designer" Nucleating Agents for Polypropylene,” *Macromolecules* **2005**, 38, 3688–3695.

[166] Kristiansen, P. M.; Gress, A.; Hanft, D.; Schmidt, H.-W., “Phase Behavior, Nucleation and Optical Properties of the Binary System Isotactic Polypropylene / N,N’,N"-tris-isopentyl-1,3,5-benzene-tricarboxamide,” *Polymer* **2006**, 47, 249–253.

[167] Libster, D.; Aserin, A.; Garti, N., “Advanced Nucleating Agents for Polypropylene,” *Polym. Adv. Technol.* **2007**, 18, 685–695.

[168] Lipp, J.; Shuster, M.; Terry, A. E.; Cohen, Y., “Fibril Formation of 1,3:2,4-Di(3,4-dimethylbenzylidene) Sorbitol in Polymer Melts,” *Polym. Eng. Sci.* **2008**, 48, 705–710.

[169] Ahmed, S.; Jones, F. R., “A Review of Particulate Reinforcement Theories for Polymer Composites,” *J. Mater. Sci.* **1990**, 25, 4933–4942.

[170] Sumita, M.; Tsukumo, Y.; Miyasaka, K.; Ishikawa, K., “Tensile Yield Stress of Polypropylene Composites Filled with Ultrafine Particles,” *J. Mater. Sci.* **1983**, 18, 1758–1764.

[171] Fröhlich, R.; Thomann, R.; Mülhaupt, R., "Toughened Epoxy Hybrid Nanocomposites Containing Both an Organophilic Layered Silicate Filler and a Compatibilized Liquid Rubber," *Macromolecules* **2003**, 36, 7205–7211.

[172] Díez-Pascual, A. M.; Naffakh, M.; González-Domínguez, J.; Ansón, A.; Martinéz-Rubi, Y.; Martinéz, M. T.; Simard, B.; Gómez, M. A., "High Performance PEEK/Carbon Nanotube Composites Compatibilized with Polysulfones-II. Mechanical and Electrical Properties," *Carbon* **2010**, 48, 3500–3511.

[173] Marchant, D.; Jayaraman, K., "Strategies for Optimizing Polypropylene-Clay Nanocomposite Structure," *Ind. Eng. Chem. Res.* **2002**, 41, 6402–6408.

[174] Santos, K. S.; Liberman, S. A.; Oviedo, M. A. S.; Mauler, R. S., "Optimization of the Mechanical Properties of Polypropylene-based Nanocomposite via the Addition of a Combination of Organoclays," *Composites Part A* **2009**, 40, 1199–1209.

[175] McGenity, P. M.; Hooper, J. J.; Paynter, C. D.; Riley, A. M.; Nutbeem, C.; Elton, N. J.; Adams, J. M., "Nucleation and Crystallization of Polypropylene by Mineral Fillers: Relationship to Impact Strength," *Polymer* **1992**, 33, 5215–5224.

[176] Evstatiev, M.; Fakirov, S., "Microfibrillar Reinforcement of Polymer Blends," *Polymer* **1992**, 33, 877–880.

[177] Fakirov, S.; Evstatiev, M., "Microfibrillar Reinforced Composites - New Materials from Polymer Blends," *Adv. Mater.* **1994**, 6, 395–398.

[178] Fakirov, S.; Evstatiev, M.; Friedrich, K., "Microfibrillar Reinforced Composites - Another Approach to Polymer Blend Processing," in "Polymer Blends," , Paul, D. R.; Bucknall, C. D., eds., J. Wiley & Sons, New York, 2000, volume 2 p. 455.

[179] Alcock, A.; Cabrera, N. O.; Barkoula, N. M.; Reynolds, C. T.; Govaert, L. E.; Peijs, T., "The effect of Temperature and Strain Rate on the Mechanical Properties of Highly Oriented Polypropylene Tapes and all-Polypropylene Composites," *Compos. Sci. Technol.* **2007**, 67, 2061–2070.

[180] Roy, C.; Chaala, A., "Vacuum Pyrolysis of Automobile Shredder Residues," *Resources, Conservation and Recycling* **2001**, 32, 1–27.

[181] Day, M.; Shen, Z.; Cooney, J. D., "Pyrolysis of Auto Shredder Residue: Experiments with a Laboratory Screw Kiln Reactor," *J. Anal. Appl. Pyrolysis* **1999**, 51, 181–200.

[182] Mark, F. E.; Fisher, M., M.; Smith, K. A., "Energy Recovery from Automotive Shredder Residue Through co-Combustion with Municipal Solid Waste," in "Energy Recovery from Automotive Shredder Residue," , Mark, F. E.; Fisher, M. M.; Smith, K. A., eds., Assoc. Plastics Manufacturers in Europe (APME), Brussels, 1998 pp. 158–175.

[183] Thorby, D., *Structural Dynamics and Vibration in Practice*, Butterworth-Heinemann, Amsterdam, 2008, 1st edition.

[184] Peterlin, A., "Mechanical Properties of Polymeric Solids," *Ann. Rev. Mater. Sci.* **1972**, 2, 349–380.

[185] Takemori, M. T., "Polymer Fatigue," *Ann. Rev. Mater. Sci.* **1984**, 14, 171–204.

[186] Crist, B., "The Ultimate Strength and Stiffness of Polymers," *Ann. Rev. Mater. Sci.* **1995**, 25, 295–323.

[187] Dencheva, N.; Denchev, Z. Z.; Oliveira, M. J.; Funari, S. S., "Microstructure Studies of In-Situ Composites Based on Polyethylene/Polyamide 12 Blends," *Macromolecules* **2010**, 43, 4715–4726.

[188] Dencheva, N.; Oliveira, M. J.; Pouzada, A. S.; Kearns, M. P.; Denchev, Z. Z., "Mechanical Properties of Polyamide 6 Reinforced Microfibrilar Composites," *Polymer Composites* **2011**, 32, 407–417.

[189] Kumar, S.; Warner, S.; Grubb, D. T.; Adams, W. W., "On the Small-Angle X-Ray Scattering of Rigid-Rod Polymer Fibers," *Polymer* **1994**, 35, 5408–5412.

[190] Földes, E., "Study of the Effects Influencing Additive Migration in Polymers," *Angew. Makromol. Chem.* **1998**, 261-265, 65–76.

[191] Burch, H. E.; Scott, C. E., "Effect of Viscosity Ratio on Structure Evolution in Miscible Polymer Blends," *Polymer* **2001**, 42, 7313–7325.

[192] Thirtha, V.; Lehman, R.; Nosker, T., "Effect of Additives on the Composition Dependent Glass Transition Variation in PS/PP Blends," *J. Appl. Polym. Sci.* **2008**, 107, 3987–3992.

[193] Allegra, G.; Raos, G.; Vacatello, M., "Theories and Simulations of Polymer-based Nanocomposites: From Chain statistics to Reinforcement," *Prog. Polym. Sci.* **2008**, 33, 683–731.

[194] Dong, S. K., Y. Bhattacharya, "Mapping the Real Micro/Nanostructures for the Prediction of Elastic Moduli of Polypropylene/Clay Nanocomposites," *Polymer* **2010**, 51, 816–824.

[195] Jancar, J.; Douglas, J. F.; Starr, F. W.; Kumar, S. K.; Cassagnau, P.; Lesser, A. J.; Sternstein, S. S.; Buehler, M. J., "Current issues in Research on Structure-Property Relationships in Polymer Nanocomposites," *Polymer* **2010**, 51, 3321–3343.

Zusammenfassung

Der Bedarf an leichten Materialien mit maßgeschneiderten physikalischen und mechanischen Eigenschaften nimmt stetig zu. Polymer-Multiphasen-Materialien (wie Copolymere, Mischungen und Verbundwerkstoffe) versprechen ein ausgezeichnetes Potential mehrere Funktionen zusammenzubringen. Die Entwicklung neuer Materialien mit den gewünschten Eigenschaften erfordert fundierte Kenntnisse der Struktur-Eigenschafts-Beziehungen von Polymeren. Für die Erfassung von Struktur-Eigenschafts-Beziehungen ist die Kombination von Struktur-Charakterisierungsmethoden mit mechanischen Tests nötig. In-situ-Röntgenstreuung während der Verformung ist eine der vielseitigsten Verfahren dieser Art der Untersuchungen. In dieser Arbeit wurde die Kleinwinkel-Röntgenstreuung (SAXS) während dem uniaxialen Strecken von orientierten Polymer-Materialien verwendet. Direkte Auswertung der aufgezeichneten SAXS-Muster ermöglicht nur eine grobe Schätzung der strukturellen Übergänge. Weitere Informationen über die Nanostruktur erhält man durch die Berechnung der Segmentverteilungsfunktion (CDF). Die einzige erforderliche Annahme ist eine Multiphasen-Struktur. Die CDF zeigt die strukturelle Informationen im realen Raum. Die Peak-Analyse der CDFs gibt Aufschluss über die Langperiode, die Langperioden-Distribution, die Domänen-Anordnung und das laterale Ausmaß der Domänen. Darüber hinaus können die lokale nanoskopische Elongation und die nanoskopische Elongationsheterogenität geschätzt werden. Die nanostrukturellen Parameter werden mit dem mechanischen Verhalten der untersuchten Materialien in Beziehung gesetzt. Um die Eignung der Methode zu demonstrieren, wurden drei Klassen von Polymeren untersucht, nämlich i. ein thermoplastisches Polyurethan-Elastomer (TPU), ii. Polypropylen (PP) und dessen Nanokomposite mit Montmorillonit (MMT), und iii. auf Polyethylen hoher Dichte (HDPE) und Polyamiden (PA6 und PA12) basierende mikrofibrille Verbundwerkstoffe (MFC). Die Ergebnisse legen nahe, dass niedriggeordnete Materialien wie TPU eine nicht-affine Verformung auf der nanoskopischen Skala zeigen. Anders gesagt hängt die nanoskopische Elongation einer Domäne von ihrer Dicke ab. Hochgeordnete Materialien wie HDPE und PP zeigen eine affine Deformation auf der nanoskopischen Skala. Dies bedeutet, dass alle Lamellen-Stapeln fast die gleiche Verformung erleben. Allerdings ist die nanoskopische Elongation – berechnet aus dem Maximum des Langperiode-

Peaks – kleiner als der makroskopischen Elongation in allen untersuchten Materialien. Dies zeigt, dass die gut korrelierte Stapeln (Domänen) weniger verformen als der Rest des Materials. Weitere Ergebnisse betreffen Mikrorissbildung, spannungsinduzierte Kristallisation und die Entwicklung der nanoskopischen Parameter während der kontinuierlichen Dehnung und Lastwechseltests.

Erklärung über frühere Promotionsversuche

Hiermit erkläre ich, Ahmad Zeinolebadi, dass vorher keine weiteren Promotionsversuche unternommen worden sind, oder an einer anderen Stelle vorgelegt wurden.

Hamburg den 20.07.2012
Ahmad Zeinolebadi

Eidesstattliche Versicherung

Hiermit erkläre ich an Eides Statt, dass die vorliegende Dissertationsschrift selbstständig und allein von mir unter den angegebenen Hilfsmitteln angefertigt wurde.

Hamburg den 20.07.2012
Ahmad Zeinolebadi

Erklärung über Chemikalien

In dieser Arbeit wurden keine Gefahrstoffe verwendet.

Die Ergebnisse dieser Arbeit wurden zum Teil in den folgenden drei Papers veröffentlicht.

Hamburg den 20.07.2012
Ahmad Zeinolebadi

Publikationen

1. Zeinolebadi, A.; Stribeck, N.; Ganjaee-Sari, M.; Dencheva, N.; Denchev, Z.; Botta, S., "*Nanostructure Evolution Mechanisms During Slow Load-Cycling of Oriented HDPE/PA Microfibrillar Blends as a Function of Composition*," *Macromol. Mater. Eng.*, **In Press**.

2. Stribeck, N.; Zeinolebadi, A.; Ganjaee-Sari, M.; Botta, S.; Jankova, K.; Hvilsted, S.; Drozdov, A.; Klitkou, R.; Potarniche, C.; Chirstiansen, J.; Ermini, V., *"Properties and Semicrystalline Structure Evolution of Polypropylene/Montmorillonite Nanocomposites under Mechanical Load*," *Macromolecules*, **2012**, 45, 962-973.

3. Stribeck, N.; Zeinolebadi, A.; Ganjaee-Sari, M.; Frick, A.; Mikoszek, M.; Botta, S., "*Structure and Mechanical Properties of an Injection-Molded Thermoplastic Polyurethane as a Function of Melt Temperature*," *Macromol. Chem. Phys.*, **2011**, 20, 2234-2248.

Index